Solar RRL
www.solar-rrl.com

Low-Temperature Processing Methods for Tin Oxide as Electron Transporting Layer in Scalable Perovskite Solar Cells

Maryam Haghighi, Nahid Ghazyani, Saba Mahmoodpour, Razieh Keshtmand, Aliakbar Ghaffari, Huiming Luo, Raheleh Mohammadpour, Nima Taghavinia, and Mojtaba Abdi-Jalebi**

Perovskite solar cell (PSC) technology experiences a remarkably rapid growth toward commercialization with certified efficiency of over 25%, along with the outstanding breakthrough in the development of SnO_2. Owing to the wide bandgap, high electron mobility, chemical stability, and low photocatalytic activity, SnO_2 has been the rising star to serve as electron transporting layer (ETL). More importantly, the low-temperature fabrication process (<200 °C) enables SnO_2 a promising candidate for the industry, making it compatible with the plastic substrates and large-scale production, which is crucial for the flexible and scalable devices fabrication. In this review, the processing methods (solution-based, vacuum-based, and vapor-based deposition) of low-temperature SnO_2 (LT-SnO_2) and the pros and cons of them with a focus on their scalability are discussed. Additionally, the morphologies of obtained LT-SnO_2 are investigated to guide the design and performance improvement of devices. The modification strategies to reduce undesired nonradiative recombination and passivate the defects in the bulk or at the interface of LT-SnO_2, influencing the quality of perovskite films, together with the efficiency and stability of cells are summarized. This review is a comprehensive overview of the studies on low-temperature SnO_2 ETL and provides detailed instructions for scalable PSCs.

1. Introduction

The perovskite solar cell stands out from the state-of-the-art family of solar cells and is rapidly becoming one of the most promising photovoltaic technologies. As of yet, the highest efficiency of this technology has been reported at 25.7%, since the introduction of perovskite photovoltaic absorbing materials based on $CH_3NH_3PbI_3$ (or $MAPbI_3$) by Miyasaka et al in 2009.[1,2] The advantageous properties of perovskite utilization as PV absorber are low recombination loss, low material cost, and the possibility of incorporating different cations and anions in its composition. Moreover, they possess a straight and tunable bandgap as well as a large absorption coefficient and high diffusion length of electrons and holes. Conversely, the major challenges of these cells include lack of control over the morphology of the layer, high moisture and oxygen vulnerability, device instability and degradation, and the presence of toxic substances like Pb in its composition.[3,4]

M. Haghighi
Department of Physics and Energy Engineering
Amirkabir University of Technology
Tehran 15875-4413, Iran

M. Haghighi, N. Ghazyani, N. Taghavinia
Physics Department
Sharif University of Technology
Tehran 14588-89694, Iran
E-mail: taghavinia@sharif.edu

S. Mahmoodpour
Department of Chemistry
Amirkabir University of Technology
Tehran 15875-4413, Iran

The ORCID identification number(s) for the author(s) of this article can be found under https://doi.org/10.1002/solr.202201080.

DOI: 10.1002/solr.202201080

R. Keshtmand
Department of Physics
Iran University of Science and Technology
Tehran 13114-16846, Iran

A. Ghaffari
School of Chemistry
College of Science
University of Tehran
Tehran 14155-6619, Iran

H. Luo, M. Abdi-Jalebi
Institute for Materials Discovery
University College London
London WC1E 7JE, UK
E-mail: m.jalebi@ucl.ac.uk

R. Mohammadpour, N. Taghavinia
Institute for Nanoscience and Nanotechnology
Sharif University of Technology
Tehran 14588-89694, Iran

Typically, the most common configuration of PSCs consists of layers deposited on top of each other as follows: electrode/electron transport layer (ETL)/absorbent/hole transport layer (HTL)/counter electrode. The electrons and holes generated in the absorbent layer are extracted through the ETL and HTL layers, respectively, and transported onto the relevant electrodes. As regards, electron transport materials (ETMs) and hole transport materials (HTMs) are applied and deposited either prior or posterior to the absorbing layer (i.e., perovskite) to make for ETL and HTL layers, respectively. The two commonly used device architectures for PSCs include mesoscopic and planar structures where mesoporous PSCs comprise of a scaffold such as TiO_2, ZnO, Al_2O_3, or ZrO_2 while planar PSCs contain of a perovskite layer that is sandwiched between ETL and HTL without any scaffold. Based on the arrangement of HTL and ETL in relation to the light illumination in PSCs, both planar and mesoporous device architecture could be fabricated in n–i–p configuration (conventional) and in inverted structure where the irradiated light first passes through HTL (p–i–n), as shown in **Figure 1**.[5,6]

In this regard, the exploitation and development of methods for manufacturing and scaling up PSCs has increased over time.[7–18] Although transparent conductive oxide (TCO) is normally utilized as substrates in the preparation of laboratory-scale cells, its utility in the fabrication of large-area modules for commercial applications is curtailed due to their rigidity and high weight. This has triggered the researchers to be in search for flexible polymer substrates such as PET and PEN.[19–22] Nevertheless, these conductive flexible materials are of limited heat tolerance and thus are incompatible with the high annealing temperatures required in the conventional ETL (e.g., TiO_2) treatment. Consequently, the deposition process of subsequent layers on these substrates needs to be accomplished at a temperature <150 °C.[23] However, there are some reports about the use of higher temperatures (180[24–26] and 185 °C[27] on PET substrate) and (180, and 200 °C[28,29] on PEN substrate). Considering that all deposited thin films in the conventional structure of PSCs, excluding ETL, could be prepared at low temperatures (less than 150 °C), fabrication of ETL below 150 °C is the main challenge in this field.

The ETL is of the most essential constituent of high-efficiency PSCs profoundly transporting electrons from the absorber layer to the electrode as well as performing as a hole-blocking layer to avoid charge recombination. Hence, ETL electron mobility is an important factor in determining the photovoltaic performance of the device. Therefore, comparatively high electron mobility is desirable for ETL since electrons could be more effectively transported and collected.

The most commonly employed ETL in the PSCs structures is TiO_2 in which albeit the rate of electron injection from the perovskite absorbent into the ETL is expedited, the electron recombination rate is also high due to its low electron mobility and transport properties. Besides, based on the high density of defects and trap sites on its surface stemming from oxygen vacancies, the recombination probability and undesirable transport increases.[30] Notably, the density of surface/bulk energy traps in TiO_2 and SnO_2 nanostructures depends on its morphology and crystal phase and can be in the range of 10^{16} to 10^{19} cm^{-3}.[31–33] In contrast, SnO_2 is also a pioneering candidate as ETL in PSCs, which represents higher electron mobility than that of TiO_2 along with superior optical properties, wide bandgap, high transparency, and higher stability.[34] In practice, PSCs based on low-temperature TiO_2 (LT-TiO_2) ETL demonstrate incompetent efficiencies due to poor crystallinity, low electrical conductivity, and high trap sites densities. On the contrary, low-temperature SnO_2 (LT-SnO_2) (<200 °C) has been widely circulated as ETL in planar PSCs representing highly favored efficiency,[35] which indicates the promise of this material as LT-ETL since the increasing number of research reports in recent years involving LT-SnO_2 (**Figure 2**a). What is more, Figure 2b exhibits the PCE trend of LT-SnO_2-based PSCs by year concerning the perovskite type of absorbent layer. In this view, various synthesis and coating methods for the LT-SnO_2 layer employed in the fabrication of PSCs, reported to be solution-based, vacuum-based, and vapor-based/assisted, are briefly reviewed and elaborated in the next section.

Energy band alignment is another crucial parameter that should be considered when designing a photovoltaic device. The energy band alignment of ETLs so as to better conform to that of the absorbent layer will facilitate electron extraction and transport further increasing J_{SC} and *FF*. In addition, V_{OC} is typically determined through the energy difference between the ETL and HTL Fermi levels. Therefore, energy-level tuning/adjusting has been extensively applied as s method to increase the V_{OC} of a device. Extraction, transport, and recombination of charges at the interface significantly contribute to determining the performance of the device. Moreover, trap sites in ETL have impact on its charge transport. Therefore, interface engineering has been utilized as an effectual method to enhance charge transporting and further optimize the device performance. Also, various ETL morphologies are designed to improve its contact with the

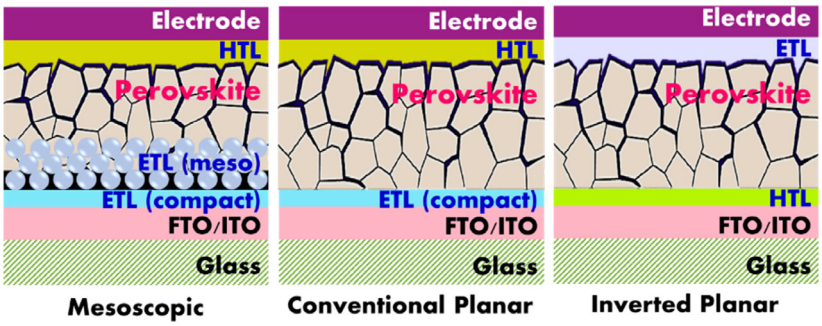

Figure 1. Principal structures of PSCs: Mesoporous PSCs, conventional planar PSCs, and inverted planar PSCs.

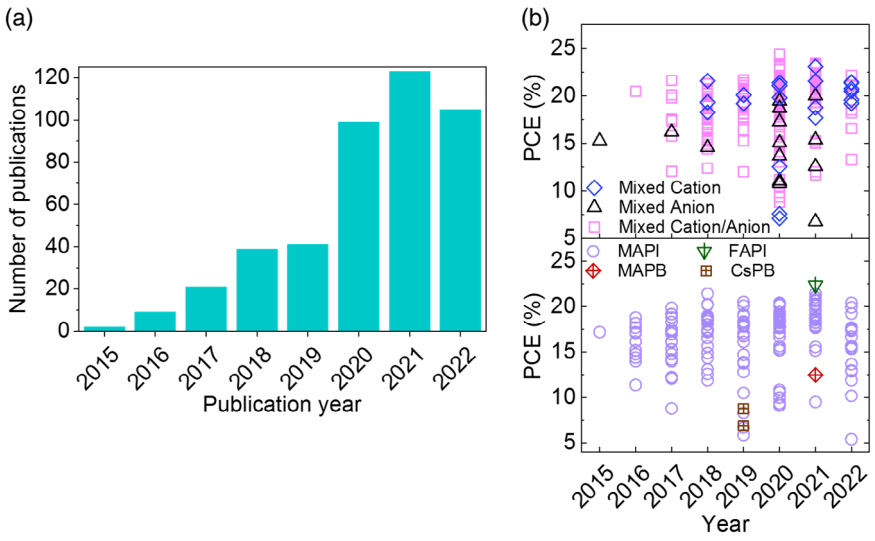

Figure 2. a) Frequency chart of the number of articles involving PSCs based on LT-SnO_2 by year. b) PCE trend of PSCs based on LT-SnO_2 by year, regarding the perovskite type of absorbing layer. (MAPI: $MAPbI_3$, MAPB: $MAPbBr_3$, FAPI: $FAPbI_3$, CsPB: $CsPbBr_3$, Mixed Cation: $FA_{0.95}Cs_{0.05}PbI_3$, $FA_xMA_{1-x}PbI_3$, $MA_{0.7}FA_{0.3}PbI_3$, $Cs_{0.04}FA_{0.92}MA_{0.04}PbI_3$, $FA_{0.5}MA_{0.5}PbI_3$, Mixed Anion: $CsPbI_2Br$, $CsPbIBr_2$, $MAPbI_{3-x}(SCN)_x$, $MAPbI_{3-x}Cl_x$, Mixed Cation/Anion: $(FAPbI_3)_x(MAPbBr_3)_{1-x}$, $(FAPbI_3)_{0.85}(MAPbBr_3)_{0.15}$, $Cs_{0.05}(MA_{0.17}FA_{0.83})_{0.95}Pb(I_{0.83}Br_{0.17})_3$, $FA_{0.83}MA_{0.17}Pb(I_{0.87}Br_{0.17})_3$, $FA_{0.75}MA_{0.25}PbI_{2.5}Br_{0.5}$, $K_{0.03}Cs_{0.05}(FA_{0.85}MA_{0.15})_{0.92}Pb(I_{0.85}Br_{0.15})_3$, $FA_{0.976}MA_{0.024}Pb(I_{0.976}Br_{0.024})_3$, $(FAPbI_3)_{0.3}(MAPbI_3)_{0.7}$, $(FA_{0.83}MA_{0.17})_{0.95}Cs_{0.05}PbI_{2.5}Br_{0.5}$, $FA_{0.75}MA_{0.15}Cs_{0.1}PbI_{2.65}Br_{0.35}$, $K_{0.035}Cs_{0.05}(FA_{0.85}MA_{0.15})_{0.95}Pb(I_{0.85}Br_{0.15})_3$, $FA_xMA_{1-x}Pb(I_yCl_z, Br_{1-y-z})_3$, $Cs_{0.06}MA_{0.27}FA_{0.67}PbI_{2.7}Br_{0.3}$, $(FAPbI_3)_{0.95}(MAPbBr_3)_{0.05}$).

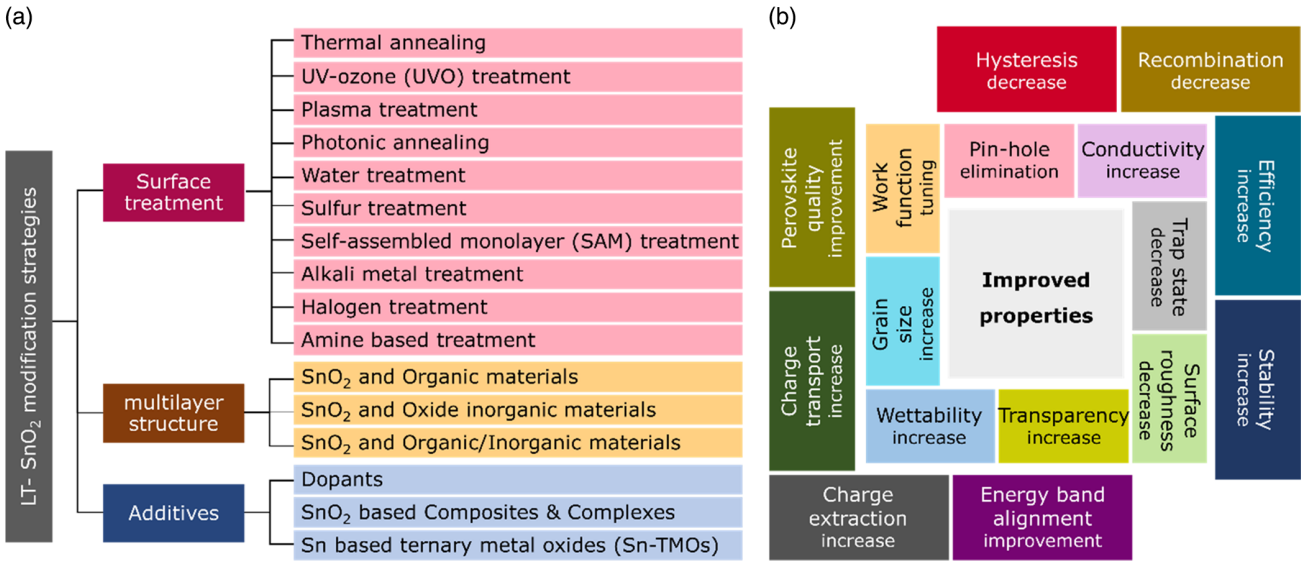

Figure 3. a) Classification of strategies utilized to LT-SnO_2 treatment and modification. b) Schematic of improved characteristics of PSCs based on modified LT-SnO_2 using various modification methods.

absorbent layer in order to achieve higher device performance. As mentioned above, all parameters influence upon each other and simultaneously determine the characteristics of a device.

Although SnO_2 layers have demonstrated high potentials in the fabrication of efficient planar PSC devices, the practically extreme residual behavior and low stability of LT-SnO_2-based PSCs is a major challenge that has made researchers applying a variety of strategies to tackle this issue. Accordingly, the strategies utilized for LT-SnO_2 treatment and modification fall into several broad categories, including surface treatment, multilayer, and additive (**Figure 3**a), which are extensively discussed in this review. According to literature, these procedures improve the structural, electrical, and optical properties of LT-SnO_2 through reducing the pinholes, enhancement of the crystallinity via the grain size enlargement as well as diminishing the grain boundaries, tuning the energy level of the work function, and optimizing the electrical conductivity and transparency. Most of which improve the wettability of the ETL so that the perovskite

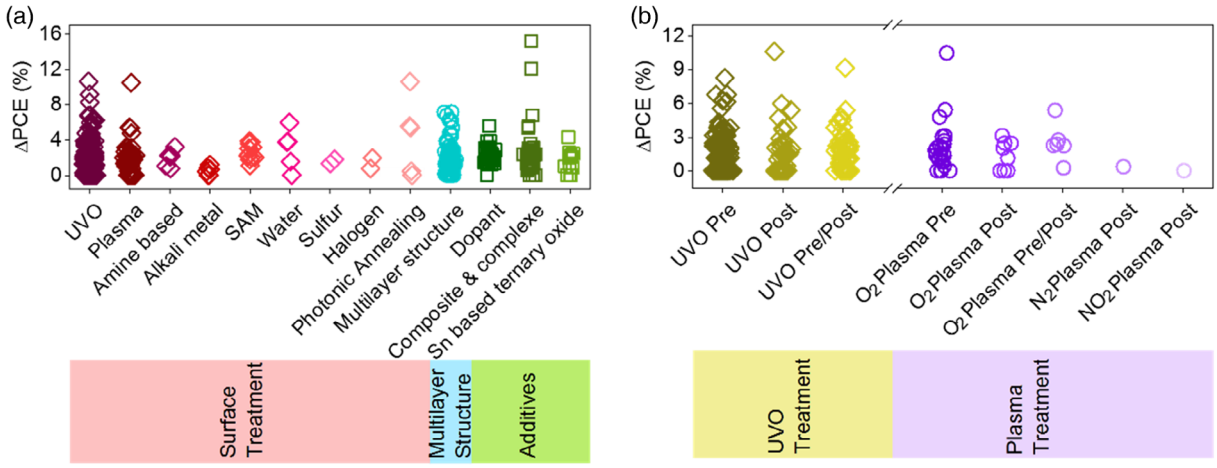

Figure 4. a) The PCE increment with respect to modification methods. b) The PCE increment with respect to UVO and plasma pre-, post-, and pre/post-treatments.

absorbing layer be more perfectly deposited. Utilizing the mentioned methods, the performance of PSCs based on modified LT-SnO_2 based is remarkably improved by means of tuning the bandgap alignment between the ETL/(perovskite) absorbing layer, enhancing the charge extraction and transport, alleviating recombination and hysteresis, as well as increasing the device stability (Figure 3b). The efficiency enhancement of the PSC using each method is represented in **Figure 4**. The reported results show that UVO treatment has been used more than other methods to modify LT-SnO_2 ETL both alone and in combination with other methods. In addition, the PCE of PSCs based on LT-SnO_2 according to the active area and the type of TCO used as substrate is shown in **Figure 5**. As illustrated, in the highest active area (35.00 cm^2), the PCE of the corresponded device is 15.08% using the flexible PEN/ITO substrate,[36] and the highest PCE, i.e., 24.40%, is reported in the active area of 0.59 cm^2 using the rigid glass/ITO substrate.[37] Moreover, the largest rigid module with an active area of 22.80 cm^2 using glass/FTO substrate has been reported to demonstrate a PCE of 12.03%.[38]

Herein, low-temperature fabrication processes of SnO_2 ETL for high efficiency and stable PSC are of great significance, in terms of the tolerance for flexible substrates and upscaling technologies. In this review, the common used LT-SnO_2 preparation methods are discussed systematically in the following section. Different morphological studies of LT-SnO_2 are reviewed so as to have a much more comprehensive understanding on the overall PSCs. Last but not least, key issues and challenges of LT-SnO_2 still demand prompt solutions, where modifications like interface engineering and addictive engineering are concluded.

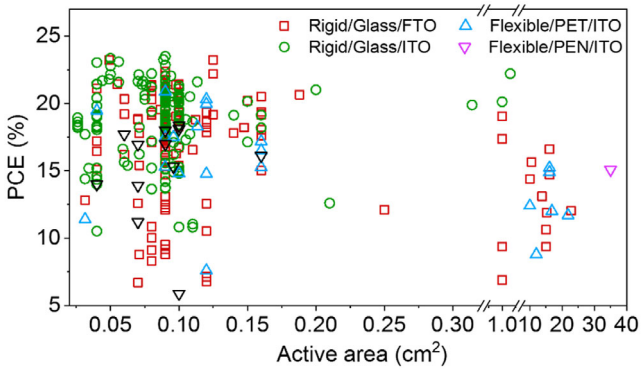

Figure 5. PCE of PSCs based on LT-SnO_2 with regard to active area and TCO type as substrate.

2. LT-SnO_2 Preparation Methods

Reports of ETL validation of SnO_2 in the fabrication of high-efficiency PSCs have increased in recent times. Among the various utilized methods, low temperature ones operable in flexible substrates, e.g., PET showing 260 °C melting temperature and PEN having that of 270 °C, are of paramount importance. A diagram of the LT-SnO_2 preparation methods is depicted in **Figure 6**. Besides, the performance and device characteristics of PSCs based on LT-SnO_2 ETL prepared through various methods are briefly presented in **Table 1**.

2.1. Solution-Based Deposition Methods

Among the various methods for SnO_2 synthesis, solution-based methods take precedence owing to the feasibility of performing the production process at low temperatures, lower materials consumption, as well as the facile manufacturing process. In order to prepare LT-SnO_2 layer, either $SnCl_4$, $SnCl_2$, and their hydrates $SnCl_2.2H_2O$, $SnCl_4.5H_2O$ tin precursors, or spin-coating of the as-received commercial SnO_2 colloidal solution often the Alfa Aesar product (Alfa-SnO_2) is employed.[39–43] As shown in Figure 6, the commercial Alfa-SnO_2 is the most frequently employed in the preparation of LT-SnO_2, and in specie, the most utilized solvent for the synthesis is ethanol.

2.1.1. Spin-Coating of SnO_2 Inks

The spin-coating technique serves as one of the most conventional methods of SnO_2 growth holding out the advantages of

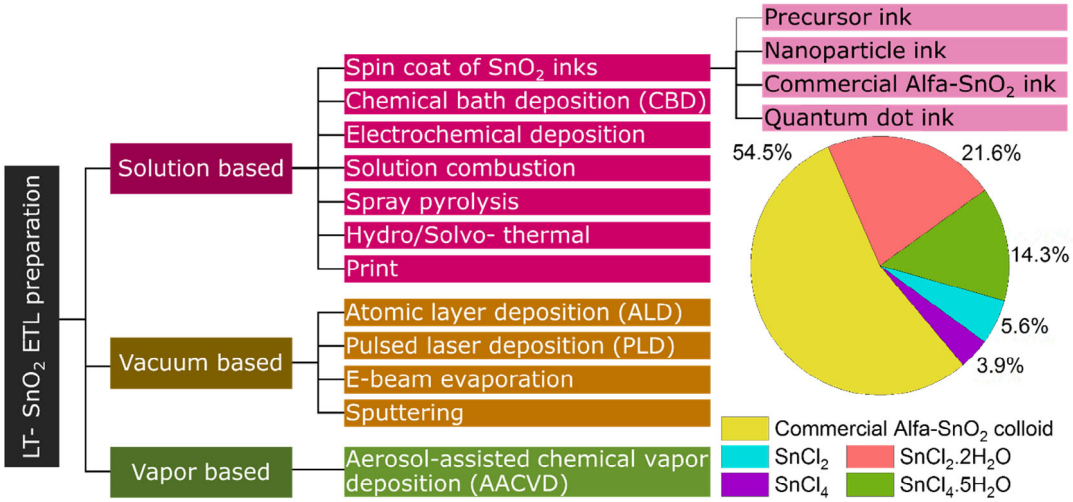

Figure 6. Diagram of LT-SnO_2 ETL preparation methods along with pie plot showing application percentage of different tin precursors in solution-based methods.

controlling the thickness of deposition and allowing the combination of different chemicals.[44,45] Classified among the inks utilized in this method is a precursor ink, e.g., the ink obtained from the sol–gel method, which contains tin chloride salt along with a sulfur source in solvents including ethanol, water, and isopropanol (IPA). In this procedure, ever since the ink is prepared, the desired layer is deposited on the substrate through the spin-coating method. However, as regards the deficient crystallization and the presence of organic and chloride residues in the prepared layer of the precursor ink, posttreatment methods such as thermal annealing or UV-ozone (UVO) are required. Yan et al. first used $SnCl_2.2H_2O$ as tin source to prepare ETL at 180 °C and reached a PCE of 17.2%, thus promoting the rapid development of LT-SnO_2. Calabrò et al.[46] could achieve 17.3% PCE making use of SnO_2 ETL prepared through spin-coating of $SnCl_2.2H_2O$ precursor ink in ethanol. Besides, Murugadoss[47] investigated the effect of ethanol and water solvents in SnO_2 precursors and recognized the superiority of ethanol solvent compared to that of water. In this regard, the utilization of water solvent provokes nonuniform coating of SnO_2 layer due to the formation of $Sn(OH)_2$ nanoparticles. Moreover, some reports[40,48–50] refer to the aging of the precursor ink prior to the deposition, which often appears to improve the quality of the SnO_2 layer. Dong et al.[48] could manage to realize 20.5% PCE utilizing SnO_2 ETL prepared through spin-coating of $SnCl_2.2H_2O$ precursor ink in ethanol aged for 24 h at room temperature.

Researchers resolved the issue of enhancing the crystalline quality and removing the organic and chloride residues into the application of nanoparticle inks. In this method, SnO_2 nanoparticles are primarily synthesized through solution-based processes including hydro/solvothermal,[51] microwave,[52] and grinding.[53] After subsequent rinsing, the resulting nanoparticles are dispersed in solvents such as ethanol, isopropanol, or water and then deposited through spin-coating on the substrate. Miyasaka et al. first used SnO_2 nanoparticles, which is purchased from chemical company, to prepare ETL and achieved a PCE of 13.0%. In the same manner, Zhu et al.[51] first synthesized SnO_2 nanoparticles using hydrothermal method and then spin-coated nanoparticles dispersed in IPA on C_{60} as a bilayer ETL in an inverted structure and achieved the PCE of 18.8%. Abulikemu and coworkers[52] utilized the microwave method to synthesize SnO_2 nanoparticles (with an average particle size of 3 nm). In the microwave method, the synthesis of SnO_2 nanoparticles is progressed more rapidly than that of the hydro/solvothermal method due to the high temperatures by microwave radiation, and besides, it enables the precise monitoring of the reaction parameters, i.e., temperature, time, and pressure. Furthermore, the grinding technique is based on physical ball milling which the latter has been broadly utilized in mechanical alloying processes. In this technique, the ball is employed not only as a mill but also as a means to form a cold welding between the powder particles so as to fabricate the desired alloy. In this light, Singh et al.[53] similarly utilized this novel procedure to produce SnO_2 nanoparticles. They prepared nanoparticles dispersed in IPA solvent and deposited on the FTO substrate through spin-coating method and could obtain the devices of 16.46% PCE. Moreover, this group could manage to further increase the PCE to 21.09% through the addition of a compact layer of SnO_2 prepared via the precursor ink spin-coating method beneath the grinding SnO_2 layer.

In recent years, researchers have been using a commercially available colloidal solution of SnO_2 nanoparticles, often from Alfa Aesar, to prepare LT-SnO_2 ETL. As indicated in Figure 6, more than half (54.5%) of the LT-SnO_2 research articles reported since 2015 have employed this solution. In the commercial Alfa-SnO_2, a small amount of KOH has been added to the solution for colloidal stability. The presence of this substance triggers the passivation of perovskite/ETL interface, which results in remarkable performance and significant reduction of PSCs hysteresis built upon Alfa-SnO_2 ETL.[26] The desired layer prepared using the Alfa-SnO_2 is uniform and pinhole free through which Jiang et al.[54] could fabricate PSCs of 20.54% PCE based on SnO_2 ETL making use of them. In addition, in 2017, they reported

Table 1. Performance and detailed parameters of PSCs based upon LT-SnO_2 ETL prepared via different methods.

SnO_2 deposition method					Cell configuration	J_{SC} [mA cm^{-2}]	V_{OC} [V]	FF [%]	Eff [%]	Ref.
Solution based	Spin coat	Precursor ink	–	Planar	FTO/SnO_2/$MAPbI_3$/Spiro-MeOTAD/Au	22.19	1.04	75.40	17.30	[46]
			Aged	Planar	FTO/SnO_2/$Cs_{0.05}(MA_{0.15}FA_{0.85})_{0.95}Pb(I_{0.85}Br_{0.15})_3$/Spiro-MeOTAD/Au	22.40	1.16	78.00	20.50	[48]
		Nanoparticle ink	Hydro/ solvothermal	Inverted	ITO/NiO/$MAPbI_3$/C_{60}/SnO_2/Ag	21.80	1.12	77.00	18.80	[51]
			Microwave	Planar	FTO/SnO_2/$MAPbI_3$/Spiro-MeOTAD/Au	21.24	1.01	65.90	14.20	[52]
			Grinding	Mesoporous	FTO/SnO_2/SnO_2/$Cs_{0.05}(FA_xMA_{1-x})_{0.95}Pb(I_yBr_zCl_{1-y-z})_3$/Spiro-MeOTAD/Au	21.46	1.22	80.09	21.09	[53]
			Alfa Aesar colloidal SnO_2	Planar	ITO/SnO_2/$(FAPbI_3)_{1-x}(MAPbBr_3)_x$/ Spiro-MeOTAD/Au	23.86	1.12	80.60	21.64	[35]
		Quantum dot ink	–	Planar	FTO/SnO_2/$MAPbI_3$/spiro-MeOTAD/Au	22.95	1.14	74.50	19.41	[29]
			–	Planar	FTO/SnO_2/$Cs_{0.05}(MA_{0.17}FA_{0.83})_{0.95}Pb(I_{0.83}Br_{0.17})_3$:$Pb(SCN)_2$/ spiro-MeOTAD/Au	23.05	1.13	79.80	20.79	[29]
	CBD		–	Planar	ITO/SnO_2/$PC_{70}BM$/$MAPbI_3$/ Spiro-MeOTAD/Au	21.30	1.05	66.30	14.80	[58]
			with Spin coat	Planar	FTO/SnO_2/$Cs_{0.05}(MA_{0.17}FA_{0.83})_{0.95}Pb(I_{0.83}Br_{0.17})_3$/spiro-MeOTAD/Au	22.59	1.17	75.00	20.73	[59]
	Electrodeposited		–	Planar	ITO/SnO_2/$MAPbI_3$/Spiro-MeOTAD/Ag	19.75	1.08	65.00	13.88	[62]
			–	Planar	PEN/ITO/SnO_2/$MAPbI_3$/ Spiro-MeOTAD/Au	20.53	1.06	66.00	14.30	[61]
	Dual-fuel combustion		–	Planar	ITO/SnO_2/$MAPbI_3$/Spiro-MeOTAD/Ag	19.01	1.08	66.00	12.93	[63]
	Spray	Ethanolic precursor ink		Planar	FTO/SnO_2/$MAPbI_3$/Spiro-MeOTAD/Au	21.80	1.01	73.70	15.40	[65]
		Aqueous nanoparticle ink		Planar	FTO/SnO_2/$MAPbI_3$/Spiro-MeOTAD/Au	21.20	1.01	78.60	16.70	[65]
				Planar	ITO/SnO_2/$Cs_{0.05}FA_{0.85}MA_{0.15}PbI_{2.9}Br_{0.15}$/ Spiro-MeOTAD/Ag	23.85	1.15	69.60	18.20	[64]
	Hydro/ Solvothermal			Planar	FTO/SnO_2/$MAPbI_3$/Spiro-MeOTAD/Au	22.76	1.05	68.00	16.17	[66]
	Print	Slot-die method	Solvent→ Water: IPA = 1:1	Planar	FTO/SnO_2/$Cs_{0.05}FA_{0.85}MA_{0.15}Pb(I_{0.85}Br_{0.15})_3$/Spiro-MeOTAD/Au	3.28	6.73	69.00	15.22	[26]
		R2R gravure	Solvent→ Water: IPA = 1:1	Planar	PEN/ITO/SnO_2/$Cs_{0.05}FA_{0.85}MA_{0.15}Pb(I_{0.85}Br_{0.15})_3$/Spiro-MeOTAD/Ag	20.31	1.05	71.78	16.95	[67]
			Solvent→ Water	Planar	PEN/ITO/SnO_2/$Cs_{0.05}FA_{0.85}MA_{0.15}Pb(I_{0.85}Br_{0.15})_3$/Spiro-MeOTAD/Ag	18.90	0.99	63.83	11.20	[67]
Vacuum based	Atomic layer deposition (ALD)	Thermal-ALD (T-ALD)		Planar	FTO/SnO_2/$(FAPbI_3)_{0.85}(MAPbBr_3)_{0.15}$/ PTAA/Au	22.74	1.11	76.00	18.37	[69]
				Planar	FTO/TiO_2/SnO_2/$(FAPbI_3)_{0.85}(MAPbBr_3)_{0.15}$/ PTAA/Au	22.98	1.14	79.00	20.03	[69]
		Plasma assisted-ALD (PA-ALD)		Planar	FTO/SnO_2/C_{60}/$MAPbI_3$:$Pb(SCN)_2$/ Spiro-MeOTAD/Au	21.50	1.13	78.96	18.80	[70]
	Pulsed laser deposition (PLD)			Planar	FTO/SnO_2/PCBM/$MAPbI_3$:$Pb(SCN)_2$/ Spiro-MeOTAD/Au	21.51	1.11	73.00	17.29	[75]
	E-beam evaporation		–	Planar	FTO/SnO_2/$Cs_{0.05}(MA_{0.17}FA_{0.83})_{0.95}Pb(I_{0.83}Br_{0.17})_3$/Spiro-MeOTAD/Au	22.75	1.10	73.00	18.20	[77]
	sputtering			Planar	FTO/SnO_2/$Cs_{0.06}MA_{0.27}FA_{0.67}PbI_{2.7}Br_{0.3}$/ Spiro-MeOTAD/Au	23.70	1.08	79.00	20.20	[38]
Vapor based	Aerosol-assisted Chemical Vapor Deposition (AACVD)		–	Planar	FTO/SnO_2/PCBM/$MAPbI_3$/Ag	14.70	1.03	67.51	10.20	[79]

PSCs of an active area of 0.07 and 1 cm^2 rendering PCEs of 21.6% and 20.1%, respectively.[35] Xu et al.[55] used DMF and ethanol as Alfa-SnO_2 aqueous diluents to improve the morphology of the ETL layer. The presence of ethanol as the diluent (Water: Ethanol:1: 1) has not only increased the stability dispersion of the solution but also increased its wettability on the substrate, whereas DMF was the opposite and reduced the wettability of the ETL layer and the crystalline quality of the perovskite layer. They compared three different solvents of pure water, water–ethanol, and water–DMF and found that when ethanol was the solvent, SnO_2 films were formed with uniform grain sizes without agglomeration, yielding 18.84 % reached a yield of 16.35% under the same conditions and with water as a diluent solvent.

The reproducibility of the SnO_2 layer process is a requirement for the commercialization and large-scale production of PSCs. Wang and colleagues[56] used Alfa-SnO_2 aqueous solution to improve ETL quality by adding oxygenated water (H_2O_2). They showed that the addition of H_2O_2 reduced the density of oxygen traps and defects and increased electron extraction, as reported by a yield of 22.15% with a 94% stability improvement after 1000 h.

Nevertheless, part of the challenges of solution-based methods for tin oxide films is the low quality of the crystallinity of the layer, which causes a relative decrease in electron mobility. The utilization of small colloidal nanoparticles of quantum dot (QD) effectively has been successfully addressed this barrier. In 2018, Yang et al.[29] could synthesize SnO_2 QDs forming energy levels that well-aligned to that of the perovskite layer and demonstrated long-term stability of up to several months. The Xu group[57] also synthesized SnO_2 QDs using radiowaves in a fast reaction (3 minutes) without additives and reported a PCE of 20.24%.

2.1.2. Chemical Bath Deposition

CBD is a solution-based method consisting of two stages of nucleation and particle growth and is based on the formation of a solid phase of the solution. In the CBD method, the substrate is immersed in a solution containing precursors. This method is influenced by parameters including bath temperature, pH and concentration of the solution, and time which does not cause physical impairs to the substrate. Furthermore, the CBD method demonstrates strong points over other techniques such as lower cost and temperature as well as higher quality and production volume. Barbe et al.[58] employed a single-stage CBD method with $SnCl_4$ precursor at 55 °C without requiring annealing in order to prepare the amorphous LT-SnO_2 layer and achieved a PCE of 14.8%. Also, Anaraki et al.[59] innovated the combined method of spin-coating and CBD technique to produce SnO_2 bilayer ETL in which the spin-coated film played the role of seed in the CBD process. By means of this combined method, they could manage to achieve devices of superior photovoltaic parameters, longer stability, and lower hysteresis exhibiting a PCE of 20.73%. One of the reasons for using CBD method in LT-SnO_2 synthesis is to reduce the agglomeration of SnO_2 precursor, but the use of CBD is limited due to the time-consuming synthesis process. Ko et al.[60] attributed the cause of agglomeration to the concentration and effect of common ions. They investigated SnO_2 provinces by rapid CBD method at low temperature and control of the precursor concentration. They deposited the SnO_2 film at 70 °C by CBD and reported a PCE of 20.12%. Surprisingly, Seo et al. conducted a two-step CBD method to tune the electronic, physical, and morphological properties of the obtained SnO_2 film by adjusting the pH and time of reaction, thus leading to a breakthrough certified PCE of 25.2% (0.0937 cm^2) and 23.0% (0.984 cm^2). However, due to large consumption of solution during the preparation, whether this method is suitable for large-scale production remain a challenging problem.

2.1.3. Electrochemical Deposition

Regardless of the trends of the methods mentioned earlier, they are not suitable for large-scale production. Consequently, the short-reaction electrodeposit technique has been regarded in the industry for converting electrical energy into chemical potential. Apart from the low-temperature production capability, this method initiates excellent adhesion between the deposited layer and the substrate and is an economical way to produce a vacuum-free uniform surface coating. Besides, morphology and layer thickness might be controlled through modifying the deposition conditions. The electrochemical deposition method takes place in a three-electrode cell containing a tin chloride precursor solution, e.g., $SnCl_2$, which includes a platinum counter electrode, an Ag/AgCl reference electrode, and a working electrode as a substrate on which the deposition is directly applied. Therein, the deposition temperature and duration (time) are of paramount importance for layer properties where the best reported temperature was 50 °C not requiring post-deposition annealing.[61,62] Chen et al.[62] could achieve the PCE of 13.88% using this method. Likewise, Lam et al.[61] recognized the 14.3% PCE under similar conditions through the addition of a PCBM layer between SnO_2 ETL and perovskite.

2.1.4. Solution Combustion

The solution combustion method is based on the exothermic disposition of self-reactions, and the heat is generated through the exothermic redox chemical reaction, although this method is mostly employed for the NiO_x synthesis. In this manner, Liu et al.[63] utilized different ratios of urea and acetone acetyl (ACAC) as dual-fuel and compared it with the ACAC single-fuel case, in which the urea behaved as an oxidizer. They could produce SnO_2 nanoplates in the single-fuel case and SnO_2 spherical nanoparticles in that of the dual-fuel case and achieve 12.93% PCE using dual-fuel combustion method.

2.1.5. Spray Coating

The utilization of spray pyrolysis has been quite widespread in the preparation of thin films. In this method, the solution droplets (aerosols) are expelled from the spray gun into the hot surface at high velocity and deposited on the surface with desired uniformity and surface coverage rendering thicknesses of even to 10 nm. In comparison to that of spin-coating method, spray pyrolysis provides the controlling and manipulation of the

deposited layer and produces a continuous, uniform coating of higher optical properties. Wang et al.[64] indicated that the use of chloride precursors in the SnO_2 layer deposition by spraying results in undesirable optical properties. To overcome this issue, they employed aqueous SnO_2 nanoparticle ink for ETL deposition and could acquire a PCE of 18.2%. Besides, Taheri et al.[65] could realize PCSs of 15.4% and 16.7% PCE, respectively, applying a comparison between those of ethanol and aqueous SnO_2 nanoparticle ink precursors as the solution utilized in the spray pyrolysis method.

2.1.6. Hydro/Solvothermal Method

In addition to the other solution-based techniques, the hydro/solvothermal method has been introduced as a deposition applied directly to the substrate. This method might be considered as a set of chemical reactions in a closed chamber in the presence of aqueous or nonaqueous solvent at temperatures beyond the boiling point of the solvent. Moreover, this process also takes place at high pressures and the selected temperature depends on the reaction required to obtain the targeted material. Thermodynamic parameters such as temperature, pressure, and time might enhance the solubility and assist the growth process. The advantageous features of this method include high efficiency, desired controllability, user-and-environmental-friendliness, manufacture of uniform-size-distributed products, and less energy consumption. With the aim of tackling one of the remarkable challenges of PSCs, i.e., low stability, Liu et al.[66] utilized hydrothermal growth method could obtain nanohierarchical SnO_2 ETLs as compact and mesoporous ETLs, which could prevent moisture penetration and improved the stability of devices.

2.1.7. Print

Printing is a versatile technique that pushes the envelope of laboratory-scale deposition works much further toward large-scale and enables the commercial production of PSCs and modules involving deposition on flexible substrates such as PET and PEN. The foremost printing methods include: Roll-to-Roll Gravure (R2R Gravure), slot-die coating, and inkjet printing. What is more, the noncontact feature of this technique offers privilege of substrate delegation including rigid (glass, FTO, ITO, etc.) and flexible (plastic/metal foil, etc.). Among them, the R2R Gravure method is the most far reaching in the industry. In ETL printing method, the concentration of precursor and the solvent type are of fundamental importance in forming a uniform and pinhole-free layer. Bu et al.[26] could achieve the PCE of 15.22% through slot-die coating of Alfa-SnO_2 solution in water/IPA solvent (1:1 ratio) on large-area flexible PET/ITO substrate with 16.07 cm^2 (active) area. In a similar vein, Gong and coworkers[67] made use of Alfa-SnO_2 solution in water and water/IPA solvent (1:1 ratio) through *R2R* Gravure printing method on flexible PET/ITO substrate at 0.07 cm^2 scale and could achieve 11.2% and 16.95% PCE, respectively.

2.2. Vacuum-Based Deposition Methods

2.2.1. Atomic Layer Deposition

ALD is a vapor-phase vacuum-based pulse technique that could be employed to produce high-quality metal oxide thin mineral films. Principally, ALD is performed in two procedures: thermal-ALD (T-ALD) at relatively low temperatures (<200 °C) and plasma-assisted-ALD (PA-ALD) in the presence of plasma. In the first half of the pulse, both of which are based on the self-limiting reactions between the surfaces edged –OH and the Sn precursor, whereas in the second half, the main reactant in the T-ALD is water (H_2O) and in the PA-ALD is oxygen (O_2).[68] Moreover, the manufacturing of thin and controllable films of up to monolayer order could be realized through ALD method. Due to the presence of plasma in the PA-ALD method, the heating temperature of the substrate during the process is lower and the plasma employed in which is the reaction outputs of O_2, N_2 and H_2 gases or their combination. Lee et al.[69] could fabricate uniform and pinhole-free SnO_2 layers at 120 °C using T-ALD method and exhibit a PCE of 18.37%, which could be further elevated to 20.03% through adding a compact TiO_2 layer under that of the SnO_2 layer. Likewise, Wang and coworkers[70] could realize the PCE of 18.8% and 16.8% utilizing PA-ALD method for SnO_2 deposition layer at 100 °C on rigid and flexible substrates, respectively. In turn, Kuang and coworkers[68] employed RF with oxygen plasma (i.e., RF inductively coupled O_2 plasma) as a reactant to fabricate the SnO_2 layer through ALD. As a versatile and robust deposition technique, ALD is capable of producing high-quality inorganic metal oxide thin films. In the first half of the cycle, self-limiting reactions take place between the surface leading to -OH groups and the Sn precursor. Subsequently, in the second half of the cycle, the main reactant in T-ALD and PA-ALD is water (H_2O) and O_2, respectively. The utility of an O_2 plasma reactant renders the deposition of SnO_2 thin films at low temperatures possible. Therein, the research group utilized tetrakis(dimethylamino)tin (TDMASn) as a Sn precursor as well as O_2 plasma to cleanse the substrate surface (ITO) prior to the deposition. Besides, after the ETL deposition and right before the perovskite layer deposition, the SnO_2 layer was exposed to O_2 plasma. In conclusion, champion PSCs showing a PCE of 17.5% using SnO_2 deposited by O_2 plasma-assisted ALD at 50 °C and 17.8% at 200 °C were obtained.

2.2.2. Pulsed Laser Deposition

In pulsed laser deposition (PLD), once the laser pulses hit the solid target material, the surface of which becomes so hot that leads to local evaporation of the material from the target as a plasma plume, the so-called ablation. In consequence of the collision of the plume with the substrate surface, a thin layer is formed on the substrate surface.[71,72] In the light of PLD application, the scattering of the ablated material from the target is avoided that provides favorable conditions for a vacuum-based unspotted deposition. If the laser ablation takes place in the air, the plasma would instantly collide with the air molecules and cease moving further. Moreover, the ablated atoms and ions react easily with oxygen, water, and other molecules in the air in a

way that they chemically transform.[72] What is more, it is possible to grow a broad range of materials extending from dielectrics, semiconductors, and metals, to superconductors via the PLD method. These materials might consist of a single element or a combination of several elements such as oxides, nitrides, carbides, and sulfides. The most prominent cause behind this versatility lies in the nature of the laser pulse, which allows the stoichiometric transfer of the target material composition onto the formed layer far from the thermal equilibrium and underoptimized conditions.[73,74] Besides, the PLD is a physical deposition technique for the preparation of thin films at low temperatures, which avoids the requisite of further thermal posttreatment. Theretofore, this method holds the potential to be applied for SnO_2 deposition on flexible substrates. Chen et al.[75] utilized the PLD and could achieve devices of rigid and flexible substrates demonstrating PCEs of 17.29% and 14%, respectively.

2.2.3. E-Beam Evaporation

E-beam evaporation is a vacuum-based method performed by means of an electron beam. The energy required for evaporation is provided through the transport of energy from the electron beams to the target material. The presence of air molecules in the route of metal vapor transport from the target material to the substrate might decrease the deposition rate and prevent the formation of compact coating, indicating the essentiality of a high vacuum. The E-beam evaporation method has been proven to enable the large-scale and cost-cutting production of LT-SnO_2 with uniform coverage. Thereupon, SnO_2 films prepared through this method demonstrate high electron mobility, desired antireflection, and directional crystallization that takes a leading role in high-efficiency PSCs.[76] Ma et al.[77] utilizing LT-SnO_2 prepared through E-beam evaporation method as ETL in PSC could obtain the PCE of 18.2% on a large active area of 1 cm^2. Since it works at vacuum condition, time and energy cost should be considered for the industrial production.

2.2.4. Sputtering

The sputtering process involves the ablation of target atoms/molecules through the plasma of an inert gas accelerating under the field and deposited on the substrate. In the same manner to that of other vacuum-based physical deposition methods, the sputtering method comprises three steps: ablation of the target material, transporting of atoms/molecules from the target to the substrate, and formation of a thin film on the substrate. In this method, the physical interaction of particles colliding with the target material serves for the ablation of the target material.[38,78] Qiu et al.[38] employed different ratios of reactive O_2 and inert Ar gas and altered the power and time of the deposition for SnO_2 ETL, which ultimately could manage to achieve 20.2% PCE on a small scale of 0.09 cm^2 and that of 12.03% on a large scale of 22.8 cm^2.

2.3. Vapor-Based Deposition Methods

2.3.1. Aerosol-Assisted Chemical Vapor Deposition

In the AACVD method adapted from CVD, a thin film of solid material is formed on the substrate as a consequence of a chemical reaction in the vapor phase. In this manner, CVD involves of a stream of gas or gaseous compounds containing a precursor chemical composition in a chamber including one or more hot surfaces (substrates). Conventionally, the CVD method exhibits a high reaction temperature in which AACVD is employed as a modification to reduce the deposition temperature. In the AACVD method, the precursor is generated through ultrasonic using a liquid/gas aerosol and subsequently introduced to the substrate surface. Noh et al.[79,80] implied that the application of AACVD at low temperatures to produce SnO_2 leads to oxygen vacancies thereof. Notwithstanding, the report demonstrated that the presence of oxygen vacancies improved charge transport in the SnO_2 layer through elevating the density of free carriers. Consequently, they could successfully obtain the 10.2% PCE on a small scale of 0.07 cm^2 (utilizing PCBM as an interlayer between perovskite and SnO_2 ETL)[79] and that of 1.4% on a large scale of 1 cm^2.[80]

3. LT-SnO_2 Modification Methods

Although various methods have been developed to deposit high-quality LT-SnO_2, the physical and electrical properties of SnO_2 films and the photovoltaic performances of devices widely vary. Thus, a great variety of strategies have been applied to modify the SnO_2 films, including surface treatment, multilayer, and addictive engineering. With these optimizations, the defects in the bulk or at the grain boundaries of LT-SnO_2 will be passivated, along with the increasing crystallinity and fewer pinholes. Moreover, the charge accumulation and recombination at ETL/perovskite interface will be hindered by the well-aligned energy level. LT-SnO_2 modification also benefit for the nucleation and growth of perovskite films, tailoring the growth direction and grain sizes.

3.1. Surface Treatment

The interface between perovskite layer and charge transport layer, particularly ETL, has played a crucial task in reducing nonradiative recombination losses through efficiently transporting photogenerated charges. The application of an engineered interface between ETL and perovskite is of the most efficient ways to eliminate these parasitic charge carrier compounds. Such an engineered interface could also pave the way for a high-performance electron conductor of a reduced band-offset. Moreover, it could also assist the formation of a compact perovskite layer so as to improve the efficiency and stability of the prepared PSCs.[81] In this regard, extensive research works have been devoted to these issues that will be reviewed in the following subsections. Besides, the PCE and performance parameters of PSCs based on LT-SnO_2 ETL modified through the surface treatment method are summarized in **Table 2**.

3.1.1. Thermal Treatment (Annealing)

Due to the widespread utilization of solution-based methods to fabricate the SnO_2 layer, thermal decomposition of Sn precursors and the conversion to SnO_2 require thermal annealing.[40,82–85]

Table 2. Surface treatment: performance and precise photovoltaic characteristics of PSCs built on LT-SnO_2 ETL modified through surface treatment.

SnO_2 modification				Cell configuration	J_{SC} [mA cm^{-2}]	V_{OC} [V]	FF [%]	Eff [%]	Ref.
Surface treatment	Thermal annealing	Air ambient	Planar	ITO/SnO_2/$(FAPbI_3)_{1-x}(MAPbBr_3)_x$/Spiro-MeOTAD/Au	23.86	1.12	80.60	21.64	[35]
		O_2	Planar	ITO/SnO_2/$(FAPbI_3)_{0.85}(MAPbBr_3)_{0.15}$/Spiro-MeOTAD/Ag	24.40	1.14	73.40	20.40	[89]
		Ethanol vapor	Planar	ITO/SnO_2/$MAPbI_3$/Spiro-MeOTAD/Au	21.85	1.08	74.28	17.66	[90]
		Air/N_2 two steps	Planar	FTO/MDCN-SnO_2/$MAPbI_3$/Spiro-MeOTAD/Au	24.16	1.07	74.05	19.14	[91]
		Air/Alkali-gas two steps	Planar	ITO/SnO_2/$FA_{0.15}MA_{0.85}PbI_3$/Spiro-MeOTAD/Au	24.71	1.10	77.91	21.10	[92]
		Hot air flow (HAF)	Planar	ITO/SnO_2/$Cs_{0.05}FA_{0.79}MA_{0.16}PbI_{2.45}Br_{0.55}$/Spiro-MeOTAD/Au	22.16	1.14	72.19	18.93	[93]
	UV-Ozone (UVO) treatment	UVO pretreatment	Planar	FTO/SnO_2/$MAPbI_3$/Spiro-MeOTAD/Au	23.27	1.11	67.00	17.21	[97]
		UVO/humidity pretreatment	Planar	FTO/SnO_2/Cs(FAMA)$Pb(I,Br)_3$/Spiro-MeOTAD/Au	22.40	1.16	78.00	20.50	[48]
		UVO posttreatment	Planar	ITO/SnO_2 QDs/$MA_{0.7}FA_{0.3}PbI_3$/Spiro-MeOTAD/Au	22.99	1.11	77.00	20.11	[94]
			Planar	ITO/SnO_2/$MAPbI_3$/Spiro-MeOTAD/Au	20.11	1.11	64.30	14.36	[96]
			Planar	FTO/SnO_2/$MAPbI_{3-x}Cl_x$/Spiro-MeOTAD/Ag	21.95	1.07	69.00	16.21	[95]
	Plasma treatment	O_2 plasma	Planar	ITO/SnO_2/$FA_xMA_{1-x}Pb(I_y,Cl_z,Br_{1-y-z})_3$/Spiro-MeOTAD/Au	24.06	1.12	80.20	21.68	[123]
			Planar	PET/ITO/SnO_2/$(FA_{0.83}MA_{0.17})_{0.95}Cs_{0.05}$ $PbI_{2.5}Br_{0.5}$/Spiro-MeOTAD/Au	12.81	5.68	42.00	3.09	[25]
		RF inductively coupled O_2 plasma	Planar	ITO/SnO_2/$Cs_{0.05}(MA_{0.17}FA_{0.83})_{0.95}Pb(I_{0.9}Br_{0.1})_3$/Spiro-MeOTAD/Au	22.10	1.08	75.00	17.80	[68]
		Ar/O_2 plasma	Planar	FTO/SnO_x/$MAPbI_3$/Spiro-MeOTAD/Au	21.36	1.13	76.90	18.64	[124]
		Ar plasma	Mesoscopic	ITO/SnO_2/*m*-TiO_2/$MAPbI_3$/Spiro-MeOTAD/Au	24.91	0.98	62.04	15.17	[290]
		N_2 plasma	Planar	PET/ITO/SnO_2/$(FA_{0.83}MA_{0.17})_{0.95}Cs_{0.05}$ $PbI_{2.5}Br_{0.5}$/Spiro-MeOTAD/Au	21.82	1.12	83.00	20.30	[25]
		N_2O plasma	Planar	PET/ITO/SnO_2/$(FA_{0.83}MA_{0.17})_{0.95}Cs_{0.05}$ $PbI_{2.5}Br_{0.5}$/Spiro-MeOTAD/Au	21.90	1.10	83.00	19.96	[25]
	Photonic Annealing	IPL Annealing	Planar	FTO/SnO_2/$MAPbI_3$/PTAA/Au	21.40	1.06	67.00	15.30	[39]
			Planar	FTO/SnO_2/$Cs_{0.05}(MA_{0.85}FA_{0.15})_{0.95}PbI_3$/PTAA/Au	15.78	1.02	78.30	12.56	[110]
			Planar	FTO/SnO_2/$MAPbI_3$/Spiro-MeOTAD/Au	20.68	1.10	77.87	17.68	[130]
	Water treatment	Hydrothermal treatment	Planar	ITO/SnO_2/$Cs_{0.05}FA_{0.81}MA_{0.14}PbI_{2.55}Br_{0.45}$/Spiro-MeOTAD/Au	22.60	1.14	79.10	20.30	[131]
		Water-bath treatment	Planar	FTO/SnO_2/$Cs_{0.05}(MA_{0.15}FA_{0.85})_{0.95}Pb(I_{0.85}Br_{0.15})_3$/Spiro-MeOTAD/Au	22.76	1.09	77.30	19.17	[121]
		Water-spin coat treatment	Planar	ITO/SnO_2/$Cs_{0.10}FA_{0.75}MA_{0.15}Pb(Br_{0.15}I_{0.85})_3$/SpiroMeotad/Au	22.58	1.14	76.33	19.68	[99]
	Sulfur treatment	Potassium *O*-hexyl xanthate	Planar	ITO/SnO_2/Potassium *O*-hexyl xanthate/$MAPbI_3$/Spiro-MeOTAD/Au	22.61	1.06	76.85	18.41	[102]
		$(NH_4)_2S$	Planar	ITO/SnO_2/$(NH_4)_2S$/FAMA$Pb(I,Br)_3$/Spiro-MeOTAD/Ag	22.95	1.15	75.95	20.03	[137]
	SAM treatment	Si-based (APTES)	Planar	FTO/SnO_2/APTES SAM/$MAPbI_3$/Spiro-MeOTAD/Au	21.93	1.16	72.00	18.32	[141]
		C_{60}	Planar	ITO/SnO_2/C_{60} SAM/$MAPbI_3$/Spiro-MeOTAD/Ag	21.53	1.07	65.00	15.18	[63]
		Zwitterion	Planar	FTO/SnO_2/NDSB-201/$Cs_{0.05}(MA_{0.15}FA_{0.85})_{0.95}$ $Pb(I_{0.85}Br_{0.15})_3$/Spiro-MeOTAD/Au	23.60	1.16	78.40	21.43	[148]
			Planar	ITO/SnO_2/DETAPMP/$(FAPbI_3)_{0.95}(MAPbBr_3)_{0.05}$/Spiro-MeOTAD/Ag	23.14	1.14	81.90	21.65	[149]

Table 2. Continued.

SnO_2 modification				Cell configuration	J_{SC} [mA cm^{-2}]	V_{OC} [V]	FF [%]	Eff [%]	Ref.
		Choline chloride	Planar	FTO/SnO_2/Choline Chloride/$MAPbI_3$/Spiro-MeOTAD/Au	22.80	1.15	72.41	18.90	[150]
		Thiol Silane	Planar	ITO/SnO_2/MPTMS/$FAMAPb(I,Br,Cl)_3$/Spiro-MeOTAD/Au	23.60	1.11	76.32	20.03	[143]
		Carboxylic acid	Planar	ITO/SnO_2/3-thiophenepropanoic acid/$MAPbI_3$/Spiro-MeOTAD/MoO_3/Ag	22.49	1.08	76.79	18.67	[151]
			Planar	ITO/SnO_2/3-thenoic acid/$MAPbI_3$/Spiro-MeOTAD/MoO_3/Ag	22.68	1.11	77.89	19.59	
			Planar	ITO/SnO_2/thiophene-3-acetic acid/$MAPbI_3$/Spiro-MeOTAD/MoO_3/Ag	23.03	1.12	80.12	20.61	
			Planar	ITO/SnO_2/PDI-P/$MAPbI_3$/Spiro-MeOTAD/Au	20.43	1.05	72.53	15.57	[152]
			Planar	ITO/SnO_2/PDI-LP/$MAPbI_3$/Spiro-MeOTAD/Au	22.57	1.08	72.81	17.83	
			Planar	ITO/SnO_2/PDI-LAS/$MAPbI_3$/Spiro-MeOTAD/Au	22.88	1.11	73.98	18.77	
	Alkali metal treatment	KCl treatment	Planar	ITO/SnO_2/KCl/$MAPbI_{3-x}Cl_x$/Spiro-MeOTAD/Au	21.82	1.12	79.30	19.44	[156]
		KOH treatment	Planar	FTO/SnO_2/KOH/$Cs_{0.05}(FA_{0.85}MA_{0.15})_{0.95}Pb(I_{0.85}Br_{0.15})_3$/Spiro-MeOTAD/Au	22.60	1.15	79.00	20.50	[26]
		KCl treatment	Planar	ITO/SnO_2/KCl/$MAPbI_3$/Spiro-MeOTAD/Au	22.50	1.06	76.86	18.29	[105]
		LiCl treatment	Planar	ITO/SnO_2/LiCl/$MAPbI_3$/Spiro-MeOTAD/Au	22.12	1.06	78.97	18.53	[105]
		NaCl treatment	Planar	ITO/SnO_2/NaCl/$MAPbI_3$/Spiro-MeOTAD/Au	22.73	1.06	77.59	18.67	[105]
	Halogen treatment	Chlorine treatment	Planar	FTO/SnO_2/1,2-dichlorobenzene/$Cs_{0.10}FA_{0.75}MA_{0.15}Pb(Br_{0.15}I_{0.85})_3$/Spiro-MeOTAD/Au	20.68	1.14	75.30	17.81	[120]
		Bromine treatment	Planar	FTO/SnO_2/1-Butyl-3-methylimidazolium bromide/$MAPbI_3$/Spiro-MeOTAD/Au	21.74	1.12	77.50	18.80	[157]
	Amine-based treatment	Guanidinium treatment	Planar	ITO/SnO_2/Guanidinium chloride/$MAPbI_{3-x}Cl_x$/Spiro-MeOTAD/Ag	19.87	1.17	80.47	18.72	[162]
		NH_4F treatment	Planar	FTO/SnO_2/NH_4F/$(FAPbI_3)_{0.95}(MAPbBr_3)_{0.05}$/Spiro-MeOTAD/Au	24.60	1.16	81.40	23.20	[104]
		Glycine treatment	Planar	ITO/SnO_2/Glycine/$Cs_{0.05}MA_yFA_{0.95-y}PbI_{3-x}Cl_x$/Spiro-MeOTAD/Ag	24.15	1.10	78.00	20.68	[34]
		2-Methylbenzimidazole (MBIm) treatment	Planar	FTO/SnO_2/MBIm/$Cs_{0.05}(MA_{0.15}FA_{0.85})_{0.95}Pb(I_{0.85}Br_{0.15})_3$/Spiro-MeOTAD/Au	23.41	1.20	77.40	21.57	[81]
p-Amino benzenesulfonic acid (ABSA) treatment	Planar	ITO/SnO_2/ABSA/$MAPbI_3$/Spiro-MeOTAD/MoO_3/Ag	22.93	1.13	78.75	20.32	[168]		

Thermal annealing under air decreases charge transport imbalance in the ETL/perovskite and HTL/perovskite interface, leading to a reduction in *J–V* hysteresis.[86] It should be mentioned that the temperature and environment, i.e., atmosphere pressure and humidity, of thermal annealing is of considerable importance. Annealing temperature should be below 200 °C. Although high-temperature annealing (>400 °C) might enhance the film crystallinity, it could result in more oxygen vacancies as well as pinholes and cracks in the film and generating gaps between the ETL and the substrate due to thermal stress and overcrystallization.[87] This in turn would increase the recombination and reduces the device performance.[88] In 2017, Jiang et al.[35] successfully ascertained 21.52% PCE of the devices using low temperature (150 °C) annealing of spin-coated SnO_2 film from a commercial colloidal suspension of SnO_2 nanoparticles as ETL in the planar PSC cell structure. Far from it, the realization of flexible PSCs requires flexible films such as PET or PEN as substrates incompatible with such high-temperature treatment and thus the deposition of the layers on these substrates must be processed at temperatures below 150 °C.[23] However, some reported performing at higher temperatures (180 °C[24–26] and 185°[27] for PET) and (180 and 200 °C[28,29] for PEN). The presence of moisture is a prerequisite for the thermal decomposition process; therefore, the annealing process in practice is carried out under medium-humidity air.[88] Nevertheless, it has been reported that this thermal process is performed under a special atmosphere such as oxygen, nitrogen, alkali gas, and ethanol vapor.

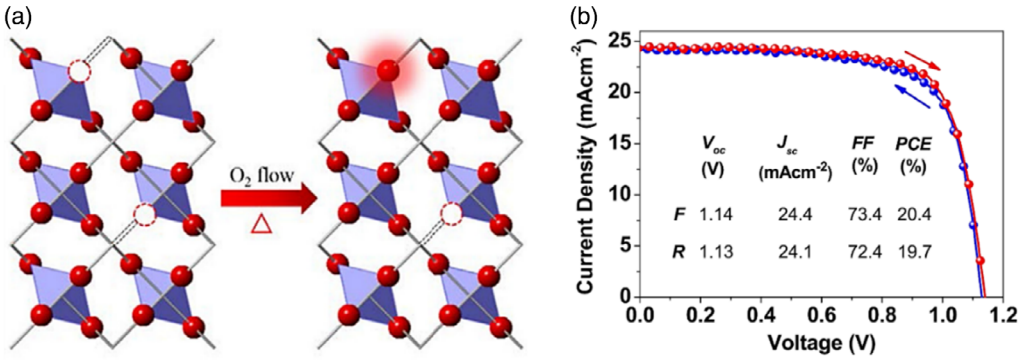

Figure 7. a) Schematic representation of the filling of oxygen vacancies along with the O_2 gas flow. b) *J–V* curves and PV characteristics of the champion PSC with SnO_2 ETL annealed under oxygen. Reproduced with permission.[89] Copyright 2019, Elsevier.

Thermal Annealing Under O_2 Gas: According to the literatures, annealing SnO_2 films under O_2 makes the oxygen in SnO_x films dramatically increase and the oxygen vacancies to reduce leading to more perfect and larger SnO_x rutile crystals. Besides, annealed SnO_x films under O_2 gas have been reported to have lower surface roughness and higher compactness that favors the perovskite growth. The reduction in surface roughness could be attributed to the reduction of the defect density in SnO_x thin films and the migration of Sn and O atoms to the defects during the annealing process.[89] Jiang et al.,[89] after which the SnO_2 films were dried at 100 °C under air, evaluated the thermal annealing effect (e.g., 180 °C) under N_2/O_2 gas flow with different O_2 percentages on the performance of the SnO_2 layer in PSC. They could successfully adjust the oxygen content, electron mobility, and trap state density in SnO_x films (**Figure 7**). To investigate the effect of self-passivation, they analyzed the charge transport dynamics (i.e., transport and carrier recombination processes) of SnO_x-based PSCs. The results demonstrated that the SnO_x films annealed under 100% O_2 gas flow presented the best carrier collection performance in PSCs.[89]

Thermal Annealing Under Ethanol Vapor: Wang et al.[90] utilized ethanol vapor during the annealing process in order to improve the performance of the LT-SnO_2 ETL. They placed the spin-coated SnO_2 film at 200 °C for 1 h on a hot plate sealed by a large glass chamber. Also, a vessel containing ethanol to produce ethanol vapor was included inside the chamber. Compared to the traditional annealing method (i.e., under air), this method has significantly augmented the electrical properties of SnO_2 film. Moreover, annealing under ethanol gas resulted in higher light absorption and lower trap state density in the perovskite layer. Therefore, PSCs were fabricated using ethanol-annealed SnO_2 film as ETL and demonstrated a facilitated electron injection and transport as well as a reduced charge recombination.

Two-Step Thermal Annealing: Huang et al.[91] combined the TiO_2 QDs in the anatase phase along with MXene in solution-based with SnO_2 nanoparticle colloid and deposited through spin-coating method. The prepared ETL was then annealed in a two-step process at 150 °C under air (5 min) and N_2 gas (25 min). According to the results, in the two-step annealing, SnO_2 nanocrystals and quantum dots of TiO_2 were formed and grew due to oxidation in the first step of air annealing. In the second step of annealing under N_2 gas, the crystals resumed growing; however, the source of the oxygen element was supplied by –OH functional groups and preformed TiO_2 crystals due to oxygen deficiency in the annealing atmosphere. This, in turn, has led to the formation of defective TiO_2 crystals that inclined to assemble with vicinal SnO_2 crystals and eventually formed a more stable phase of TiO_2/SnO_2 heterojunctions. Conclusively, utilizing a two-step thermal annealing process with the formation of TiO_2/SnO_2 nanoscale heterojunction and the enhancement of ETL conductivity due to the presence of MXene as conductive bonded bridges as a multidimensional conductive network (MDCN).

Huang and coworkers[92] also employed a versatile two-step annealing process to improve SnO_2 ETL. In the first step, annealing was performed at 150 °C and then the samples were kept in a reaction chamber containing a certain amount of ammonia solution in which the samples were separated from the solution. Consequently, the chamber was sealed and heated for 2 h at a temperature of 120 °C, during which time the layer was exposed to the alkaline gas produced (**Figure 8**a). Regarding the corrosion caused by alkaline gas during the second step of annealing, the surface of SnO_2 film was polished, and also $-NH_2$ group was chemically adsorbed onto the surface of the SnO_2 layer. The surface polishing resulted in the ETL surface smoother. According to the results, the crystallinity quality of the perovskite film has significantly excelled after applying SnO_2 annealing under alkaline gas. The justification behind these effects was presented in two pathways. As shown in Figure 8b, the $-NH_2$ groups adsorbed onto the SnO_2 surface would firmly interact with the perovskite halide anions through hydrogen bonding providing germination sites for further nucleation of perovskite crystals by accelerating atoms in the preheating of perovskite film. As viewed by the classical nucleation theory, during the nucleation process, the reduction in volumetric free energy caused by a temperature decrease could merely recompense 2/3 of the surface energy of the nucleus and the rest has to be supplied through the conditions stemmed from local energy fluctuations of the perovskite films preheating. The presence of hydrogen bonds formed between perovskite halide anions and the $-NH_2$ group could efficiently increase local energy fluctuations and accelerate crystal nucleation. Furthermore, $-NH_2$ groups are of smaller molecular dimensions than that of the perovskite organic molecule which comes to their aid to incorporate into the inorganic

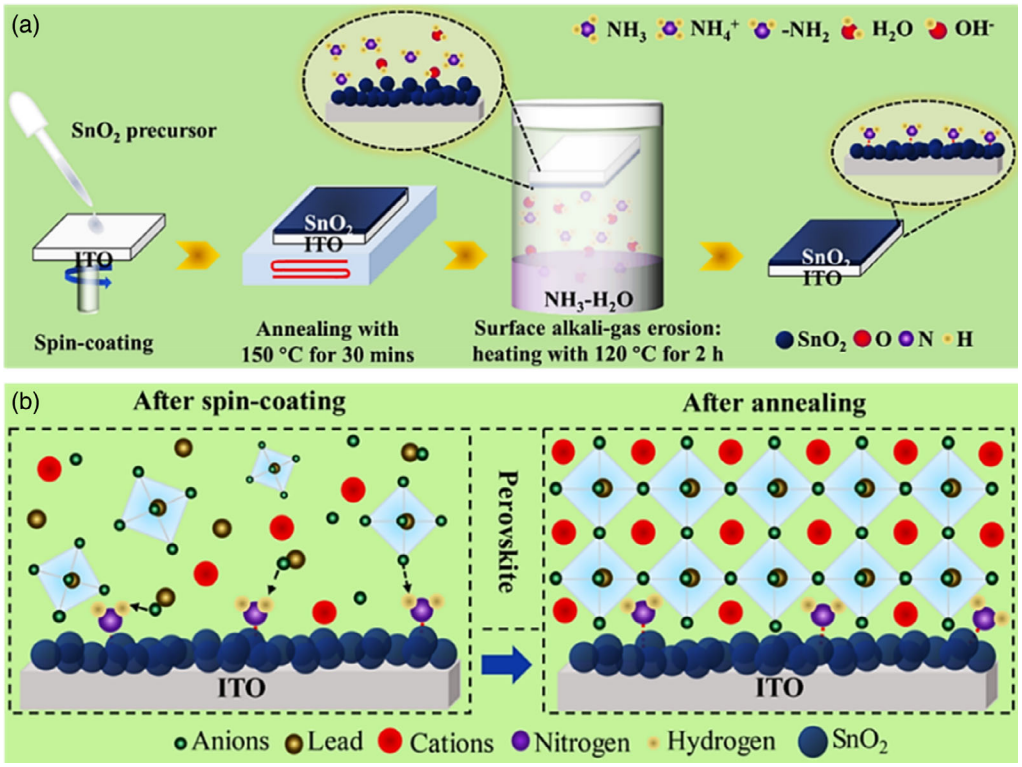

Figure 8. a) Schematic of the two-step thermal annealing process under air/alkali gas and surface polishing arising from the presence of alkaline gas. b) Schematic of the structure and nucleation process in the perovskite/ETL interface. Reproduced with permission.[92] Copyright 2020, American Chemical Society.

perovskite framework and substitute the perovskite organic molecule at the bottom of the film as the annealing process resumes. As a consequence, the rate of perovskite crystals nucleation would be enhanced and a bridge link between SnO_2 and perovskite is constructed. By and large, utilizing a two-step thermal annealing process with polishing and adsorption of $-NH_2$ group, they could manage to improve mobility, charge transport in the perovskite/ETL interface, and crystallinity of the perovskite layer with the achievement of a 21.1% PCE.

Thermal Annealing Under Hot Air Flow: Smith et al.[93] made use of a fast roll-to-roll (R2R) compatible process for SnO_2 ETL annealing. In this method, to rapidly anneal SnO_2 ETL at 120 °C in 1 minute, a heat gun of control capability is employed for rendering a hot HAF. They found that elevating the duration of the HAF thermal annealing process up to 5 minutes made the roughness of the ETL surface enhance due to the increment in grain radius that was favored for the perovskite deposition.

3.1.2. UV-Ozone Treatment

Since the conventional methods of the preparation of SnO_2 films demand the application of precursor ink (i.e., tin chloride) that requires high temperature, they are not suitable for upscaling. To tackle this issue, UVO posttreatment has been presented as a suitable method that will further overcome the technical rigors of the manufacturing process and production costs and facilitate the large-scale fabrication of SnO_2 films. Generally, UVO treatment is always considered to remove the surface contaminants, improve the wettability, and change the states of surface oxygen. The major wavelengths of the ultraviolet rays radiated from a well-known low-pressure mercury vapor lamp are 184.9 and 253.7 nm. During the process of formation or decomposition of O_3, atomic oxygen (O) having a strong oxidizing ability is generated. Organic compounds can be decomposed by irradiating them with energy stronger than the bond energy. These excited contaminants, or the free radicals of the contaminants formed by photolysis, react with atomic oxygen to form simple molecules such as CO_2, H_2O, N, and O_2, which are removed from the surface.[94–96] Generally, UVO treatment is applied as pretreatment and posttreatment, before and after the ETL deposition, respectively.

UV-Ozone Pretreatment: In the majority of research works utilizing low-temperature SnO_2 films as ETL in PSC, the UVO pretreatment time was reported to be between 5[26,97] and 30[98–100] minutes, among the 15 minutes to be dominant.[39,64,90,93,96,101–105] The principal purpose of performing this treatment was to clean-up the surface of the substrates from volatile organic compounds as well as the enhancement of wettability.

(UV-Ozone/Humidity) Pretreatment: Dong et al.[48] produced moisture molecules adsorbed onto the surface through the utility of UVO pretreatment under humidity on substrates prior to the SnO_2 layer deposition (**Figure 9**a). They managed to harness the water adsorbed onto the substrate surface through ambient humidity and UVO pretreatment duration monitoring.

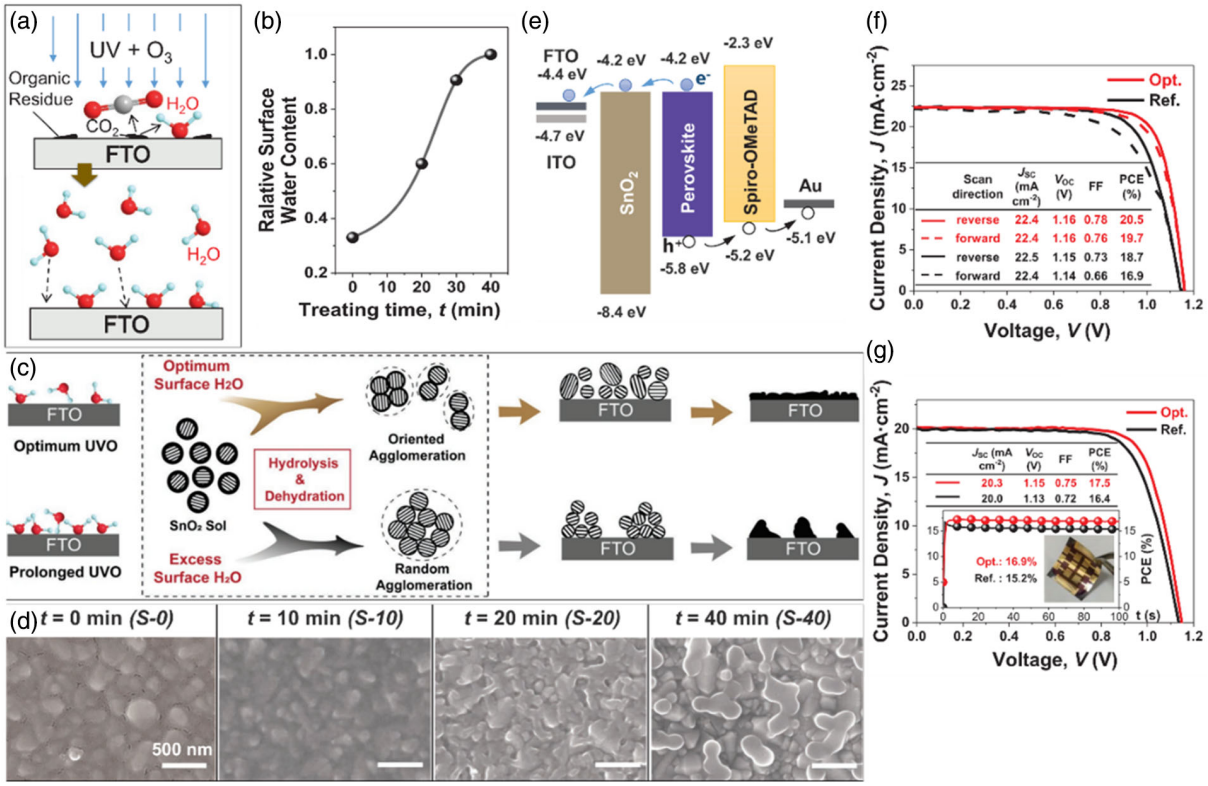

Figure 9. a) Schematic illustration of UVO pretreatment and water absorption on the FTO substrate. b) Relative surface water content (estimated using the FTIR spectrum) as a function of UVO pretreatment time. c) Schematic representation of the proposed mechanisms for the structural evolution of SnO_2 thin films on FTO substrates with water adsorbed in optimized and prolonged duration (higher than optimized times). d) SEM images of the surface of SnO_2 films on the FTO substrate throughout different UVO pretreatment times. e) Energy-level diagrams for PSC with n–i–p structure. *J–V* curves and PV parameters of PSCs with the f) rigid glass/FTO and g) PEN/ITO flexible substrates employing reference (Ref.) and optimized (Opt.) ETLs. Reproduced with permission. [48] Copyright 2019, John Wiley and Sons.

The results of the systematic studies demonstrated that the optimal amount of surface adsorbed water molecules throughout the deposition of SnO_2 nanocrystals using the sol–gel method at room temperature on UVO pretreated substrates facilitates optimal hydrolysis-condensation reactions for SnO_2 regrowth (Figure 9b). Furthermore, UVO pretreatment of the substrate makes for a perfect coverage of SnO_2 of desired morphology and crystallization along with superior optical and electrical properties as well as optimized roughness that provokes a more perfect bonding of the interface with the perovskite layer. The sight of pinholes and cracks will be vanished in UVO pretreated samples, resulting in a thin and compact film of ideal coverage and low roughness. Nevertheless, UVO pretreating of longer than optimized time drives the SnO_2 grains to agglomerate and further surface roughness increment and a defective coating in the films is obtained (Figure 9c,d). Employing the UVO pretreatment, Dong et al.[48] could manage to simultaneously optimize crystallinity, trap state density, and surface roughness in the SnO_2 ETL employed in PSCs fabricated at room temperature. The structural advantages of the treated SnO_2 film made for further improvements in charge transport dynamics and minimized energy loss in the PSCs that significantly enhanced their PCE (Figure 9f,g).

UV-Ozone Posttreatment: As viewed by the literature, the duration of UVO posttreatment has been reported to vary between 5[27] and 60[95,96,106] minutes, with that of 15 minutes to be more frequent.[40,65,92,93,104,107–110] UVO posttreatment, through wiping out the organic residues on the surface of SnO_2 film, would lead up to the increased hydrophilicity and wettability of the SnO_2 layer and improved surface adhesion between the SnO_2 layer and perovskite. All but most of the SnO_2-based PSCs reported heretofore are freshly employed with that of a few minute treatments under UVO, which appears as an essential step before the perovskite deposition.[111] Furthermore, posttreatments of the ETL using UVO have an impact on perovskite growth.[30] In particular, as regards the decrease in the concentration of oxygen vacancies making a downward change in the Fermi levels, the work function of metal oxides might be elevated upon UVO posttreatment. Surface UVO posttreatment improves the interface properties between the ETL and the perovskite that promotes the interaction between the ETL and the perovskite layer, thereby facilitating expeditious electron injection from the perovskite layer to the ETL.[87]

In UVO treatment, ultraviolet light is simultaneously generated at two wavelengths of 253.7 and 184.9 nm possessing high energy and the corresponding photon energy of which is

472 and 647 kJ mole^{-1}, respectively. Both photon energies are higher than those of Sn–Cl and O–H bonds having bond energies on the order of 350 and 459 kJ/mole, respectively. Also to be found, they are higher than those of C–C, C–H, and C–O bond energies thereabouts 346, 411, and 358 kJ mole^{-1}, respectively. Therefore, UV light is capable of readily breaking down these chemical bonds so that the reaction perpetuates. Meanwhile, UV light of 184.9 nm wavelength could convert O_2 oxygen molecules to active O_3 ozone molecules, which facilitates the formation of SnO_2, decomposition as well as the oxidation of organic compounds, and the final by-products are released as Carbon monoxide (CO_2) and water (H_2O).[94] So too did, Liu et al.[94] studied the deposition of SnO_2 quantum dot colloidal solution to construct the QD SnO_2 layer as ETL. High-temperature sintering is customarily applied to remove contaminants albeit in might lead to some defects in the SnO_2 QD film. Nevertheless, to curb this issue, the research group utilized UVO posttreatment at room temperature to detach ethyl groups from SnO_2 QD film and managed to obtain a PCE of 20.1%.

Furthermore, it has been reported that the surface temperature of the layers throughout UVO upraises to about 60 to 70 °C due to the effect of UV light.[95,96] Case in point, Li et al.[96] spin-coated a commercial Alfa-SnO_2 ink followed by annealing at 50 °C for 5 minutes. Thereby, the layers were treated with UVO for 60 minutes. The results of temperature measurement using an infrared thermometer demonstrated that the temperature of the layers increased by about 60 °C during UVO due to its light radiation. According to them, UVO posttreated SnO_2 layers displayed superior compactness, purity, and transparency.

Moreover, Huang et al.[95] compared the performance of UV-sintered SnO_2 films with that of 180 °C annealed films in the PSC architecture. Thereby, UV-sintered SnO_2-based PSCs possessed 16.21% PCE, whereas annealed SnO_2-PSCs displayed 11.49% at 180 °C. Likewise, it was reported therein that the UVO treatment process imposes a thermal process in the meantime and that the temperature in the entire UVO process is normally below 100 °C. From the findings of the experiment, in the short periods, the layers were of pinholes which could undermine the hole blocking performance of SnO_2. Besides, it was demonstrated that the –OH bond density increased and then further decreased upon increasing UVO treatment duration. These findings implied that after which the UVO treatment was applied the hydroxyl groups were formed on the SnO_2 surface, and the more –OH groups on the SnO_2 surface the lower the recombination rate. These results are schematically summarized in **Figure 10**.

3.1.3. Plasma Treatment

One of the utilities of plasma treatment involves surface activation, which offers numerous benefits including higher efficiency, cost-effectiveness, and environmentally friendliness over traditional methods of wet physical and chemical activation. When the plasma comes in contact with the surface, the induced energy transferred by the plasma engenders subsequent reactions on the surface of the material.[112] In consequence, the wettability of the

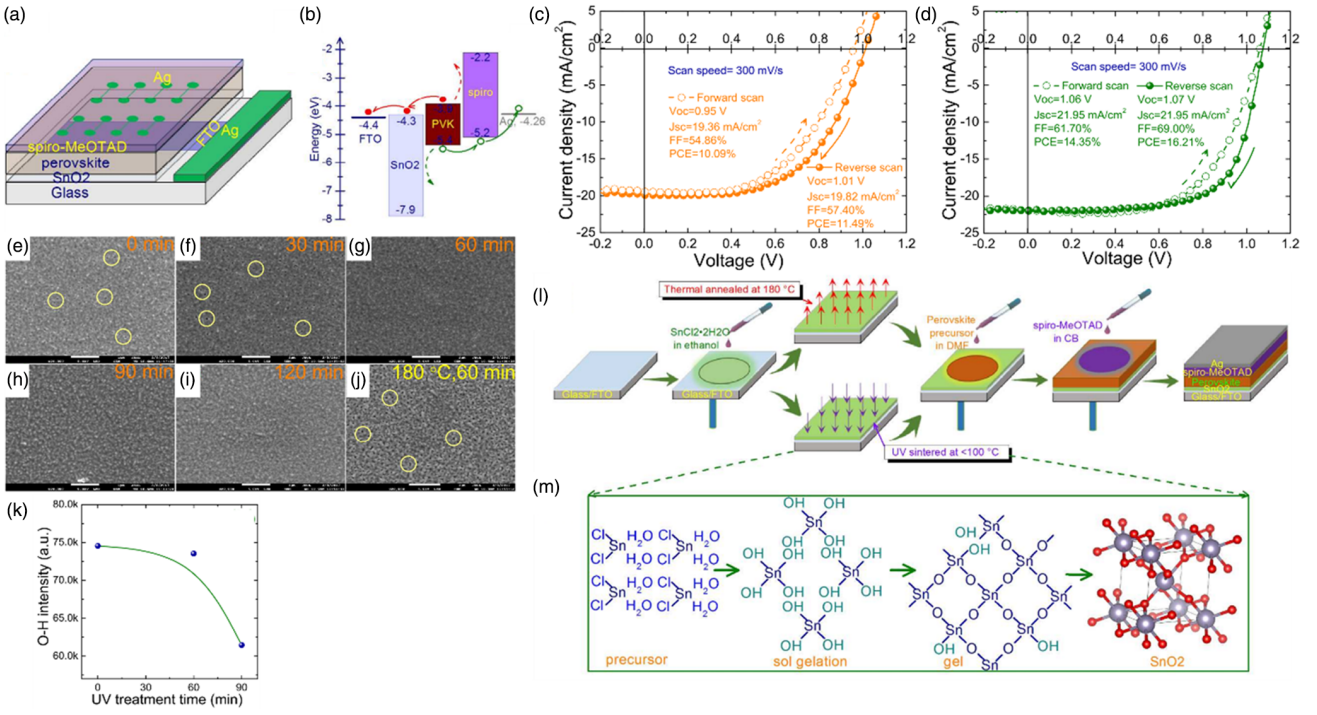

Figure 10. a) Schematic representation of the PSC architecture. b) Energy-level diagrams of PSC with n–i–pstructure. The *J*–*V* curves of the PSC based on c) annealed SnO_2 at 180 °C and d) UVO posttreated SnO_2. SEM images from the surface of SnO_2 films e-i) UVO posttreated at different times (0–120 minutes) and j) annealed at 180 °C for 60 minutes (the white scale bar in the figure represents 1 μm). k) –OH groups density of SnO_2 films with different time periods of UVO treatment. Schematic diagram of l) PSC fabrication process and m) proposed reaction mechanism. Reproduced with permission.[95] Copyright 2017, American Chemical Society.

surface increases and the water contact angle decreases owing to plasma treatment, and thus the surface is rendered more hydrophilic. Besides, it curtails the concentration of C–C or C–H bonds.[112–114] Each gas type possesses variant characteristics that affect the surface properties of an object within different respects. As regards, neutral or inert argon (Ar) plasma has reportedly displayed no chemical effects on the surface.[115] The major difference between Ar and O_2 plasma lies in the mechanism of the surface activation, i.e., physical etching and chemical reaction, respectively.[116] Moreover, the chemical interaction of oxygen-based plasma systems can form strong carbon–oxygen (C–O) covalent bonds of higher polarity than those of carbon–hydrogen (C–H) bonds.[112,114,117]

In recent times, plasma utilization has been acknowledged to be an efficient posttreatment procedure. In particular, the impacts of plasma treatment on metal oxide-based semiconductors to control carrier concentrations associated with oxygen vacancies have enormously attracted research interests.[118,119] The reports have demonstrated that the O_2 and N_2 plasma treatment reduced the carrier concentration which was also accompanied by some oxygen vacancies. By comparison, the oxygen vacancies population is significantly higher in Ar plasma treatment. In the case of O_2 plasma, bulk traps are treated through filling the oxygen vacancies even though the surface is damaged by ion bombardment.[119] O_2 plasma treatment has been more frequently utilized compared to the other gases in both pre- and posttreatment methods, i.e., before and after SnO_2 ETL deposition. In the cases of O_2 plasma utilization as pretreatment, the duration of pretreatment was reported to extend between 3[68] and 20[110,120] minutes in which the 5-minute time was more frequent.[24,121,122] Besides, in the case of O_2 plasma utility as posttreatment and an alternative of thermal annealing, the posttreatment duration was reported to vary between 2.5 and 15 min and likewise, the 5-min time was dominant.[25,68,123–126] In these

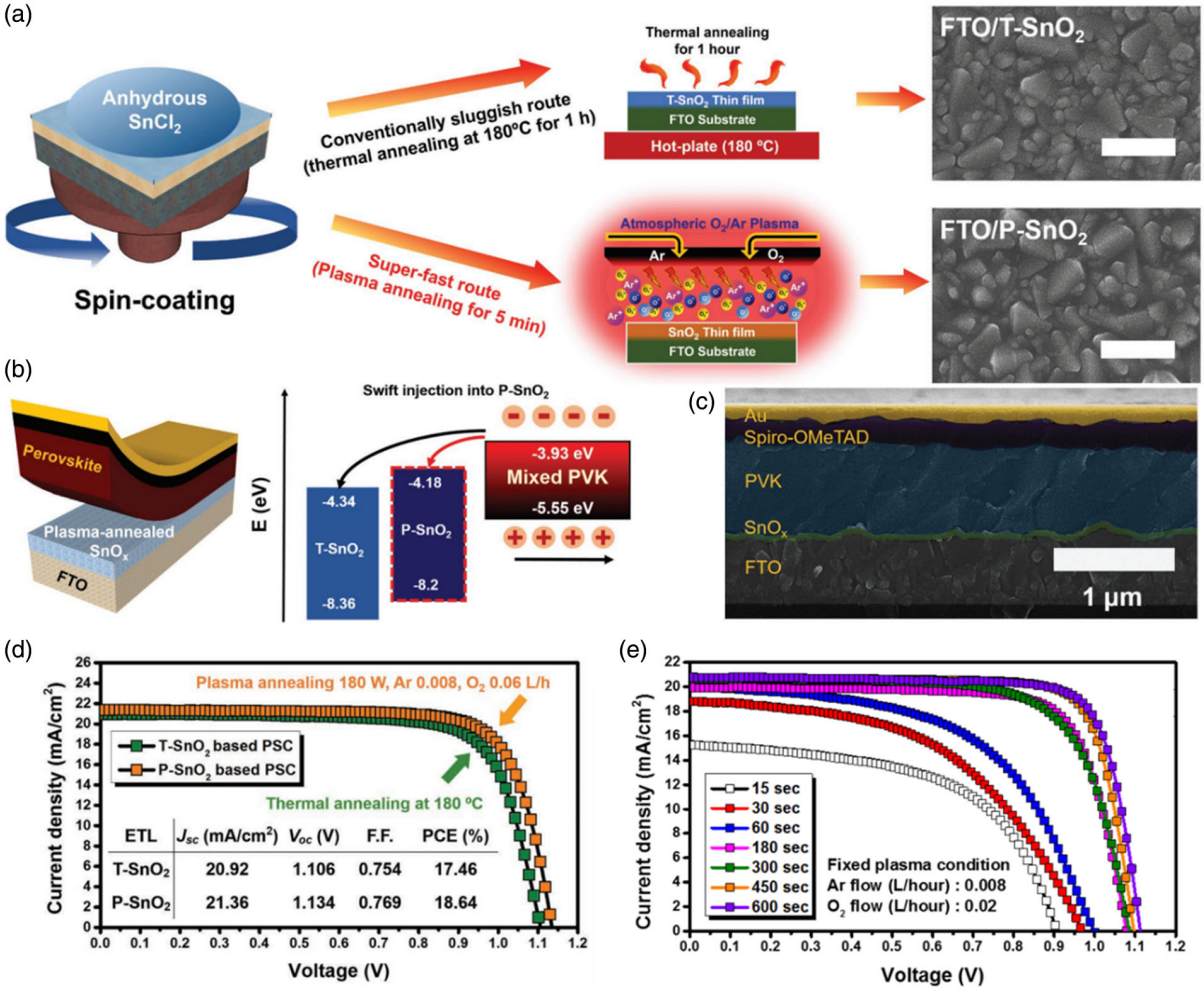

Figure 11. a) Schematic pathway of SnO_2 thin film prepared through thermal energy or O_2/Ar and FESEM images obtained from two types of films. The T-SnO_2 thin film was annealed at 180 °C for 60 min and the *P*-SnO_2 thin film was prepared through plasma energy at a gas flow rate of 0.008 Lh^{-1} (Ar) and 0.06 Lh^{-1} (O_2) for 5 min. b) A schematic representation of PSC structure employing SnO_2 thin film as ETL and the energy band diagram showing the behavior of photo-excited electrons at the interface between the perovskite and both SnO_2 thin-film types. c) Cross-section FESEM image of PSC with *P*-SnO_2 thin film. d) *J–V* curves of PSCs with *P*-SnO_2 and T-SnO_2. e) *J–V* characteristics for PSC dependent on some degree on plasma oxidation time of 15 to 600 seconds in a constant gas flow. After 450 seconds, the PV performance was saturated at a certain point. Reproduced with permission.[124] Copyright 2018, John Wiley and Sons.

reports, the main purpose of functioning the posttreatment was to modify the roughness, activate the surface, tune the energy level of the conduction band (E_{CB}), and enhance the work function of SnO_2 ETL. Luan et al.[123] applied O_2 plasma to posttreat the surface of trifluoroethanol-incorporated SnO_2 (T-SnO_2). They investigated the effect of O_2 plasma power on PSC performance in which a champion efficiency of 21.68% was achieved at 60 watts. Yu et al.[124] were of the pioneers that reported the utilization of the Ar/O_2 plasma atmosphere as the major energy source to activate the sol–gel film to form a compact SnO_2 thin film of $SnCl_2$ precursor at a record rate of $\leq$5 min. The amorphous SnO_2 thin films employed as ETL in PSC were prepared through anhydrous $SnCl_2$ spin-coating solution followed by thermal annealing (T-SnO_2) or plasma (P-SnO_2) (**Figure 11**a). In turn, the T-SnO_2 thin film was prepared slowly under thermal stress of 180 °C temperature for 1 h, whereas the *P*-SnO_2 thin film was fabricated very rapidly in 5 min under Ar/O_2 plasma atmosphere along with undesired heat (i.e., ≈50 °C) as well as plasma ion bombardment (Figure 11a). Even though the undesired thermal energy is involved to some extent, its effect is negated owing to the degree of oxidation caused by the oxygen flow rate and the duration of the radiation. Therein, the duration of plasma irradiation in the range of 15 to 600 s was examined (Figure 11e). In the semi-oxidized state of the SnO_2 thin film (i.e., <450 s), the remaining Sn^{+2} and Cl^- ions might incorporate into the perovskite lattice and undermine the PSC performance since Sn^{+2} ions are prone to facile oxidization under ambient air.

Also been demonstrated, the formation of metal–oxygen–metal (M–O–M) and hydroxyl metal (M–OH) bonds in P-SnO_2 thin film was higher and lower, respectively, than that of T-SnO_2 in which M–OHs plays the role of shallow trap sites. The widespread presence of M–OH indicated the deficient oxidation of the oxidative network, which reduces the mobility of the SnO_2 thin film, decreases the electron life, and hinders desired electron transport. Furthermore, thermal annealing is given to make for more grain boundaries due to the activation of necking between SnO_2 particles wherein a high density of shallow trap sites is generated owing to network mismatch. Moreover, due to the passivation of the surface stemming from the treatment of inherent defects and the substitution of carbon impurities with oxygen during plasma annealing, the conduction band minimum can be moved upward (Figure 11b).[124] Therefore, with the use of plasma annealing, the research group was capable of fabricating a denser oxide network compared to that of thin layers oxidized under thermal annealing resulting in supreme electrical conductivity along with lower trap densities. As concluded by these findings, plasma annealing is a cost-effective and efficient fabrication procedure of high-quality thin films for various metal oxides that can be prepared using the sol–gel route.[124] Also, Shekargoftar et al.[127] used argon plasma (atmospheric pressure and power density 2.5 W cm^{-2}, 5 min, <60 °C) for the treatment of SnO_2 films and its performance by thermal annealing (30 min, 180 °C) compared. The O_{1S} peak of the XPS spectrum of their samples was fitted by three compounds with binding energies of 530.5, 531.6, and 532.9 eV, which correspond to the oxygen contained in SnO_2/SnO, Sn–OH hydroxides, and water adsorbed on the surface, respectively. Thermal annealing was more effective in removing water due to higher temperatures. But the plasma-treated sample showed more Sn–OH hydroxides, which the group attributed to the formation of surface defects by high-energy plasma argon species bombardment. Subbia et al.[25] reported that compared to PSCs with heat-annealed SnO_2, PSCs with SnO_2 treated with N_2 plasma had higher efficiencies of 20.3% on rigid substrates and 18.1% on flexible PET/ITO substrates. These flexible PSCs were extremely stable since they could maintain 90% of their initial PCE after 1000 cycles. The result demonstrated that deep UV (DUV) radiation employing N_2 and N_2O plasma emissions plays a prominent role in achieving high attribute metal oxide thin films at lower temperatures. In this line, this group[25] reported a novel strategy for the production of SnO_2 metal oxide semiconductors at near-RT temperatures including low-power inductively coupled radio frequency (RF) plasma. In this method, sol–gel-coated SnO_2 thin films are activated using nitrogen plasma to break down the alkoxy and hydroxy groups allowing the formation of a M–O–M network (**Figure 12**a). Besides, the performance comparison among the as-deposited/annealed SnO_2 thin films and that of deposited through RF coupled with O_2, N_2, and N_2O plasmas (i.e., AD-SnO_2, OPT-SnO_2, NPT-SnO_2, and NOPT-SnO_2, respectively) and also that of thermally annealed SnO_2 (TA-SnO_2) in PSCs was conducted (Figure 12c). According to the results, the chlorine-containing residues in the thermally annealed samples and treated-under-nitrogen-plasma samples were less than that of the treated-under-oxygen-plasma sample. It is remarkable that the formation of SnO_2 film from Sn metal-halide precursor merely takes place in the presence of N_2 plasma, whereas reactive species of O_2 plasma fared poorly. Studies in this group have represented that the formation mechanism in the presence of ultraviolet (UV) rays involves breaking down the metal alkoxy-hydroxyl bonds to form the M–O–M structure followed by film thickening and compactness. In the described mechanism, the plasma emissions containing DUV photons provide the energy required to initiate the breakage of alkoxy-metal bonds although the RF power is relatively low. In the case of O_2 plasma, the emission spectrum at an operating pressure close to 1 torr does not contain the UV component required to initiate the bond cleaving process, therefore, the produced film retains the original composition of the deposited layer to a greater extent. The favorable outcome of NOPT-SnO_2-based PSCs verifies that DUV emission from N_2 plasma is indispensable for the initial cleavage of metal alkoxy and metal hydroxyl bonds and the resulting formation of SnO_2 thin films.[25]

3.1.4. Photonic Annealing

The long processing time is a bottleneck for fast and large-scale production, which is a major motivator and financial incentive for the widespread deployment of PSCs. In this regard, intense pulsed light (IPL) annealing holds the convincing potential to significantly enhance the performance and compatibility of the manufacturing process. In this method, broadband light pulses in a short scale of milliseconds and of high intensity, normally xenon flash lamp, are employed for swift and selective annealing of light-absorbing materials. The short duration of this process causes the temperature in the absorbent material to ascent locally devoid of damaging the temperature-sensitive substrates such as

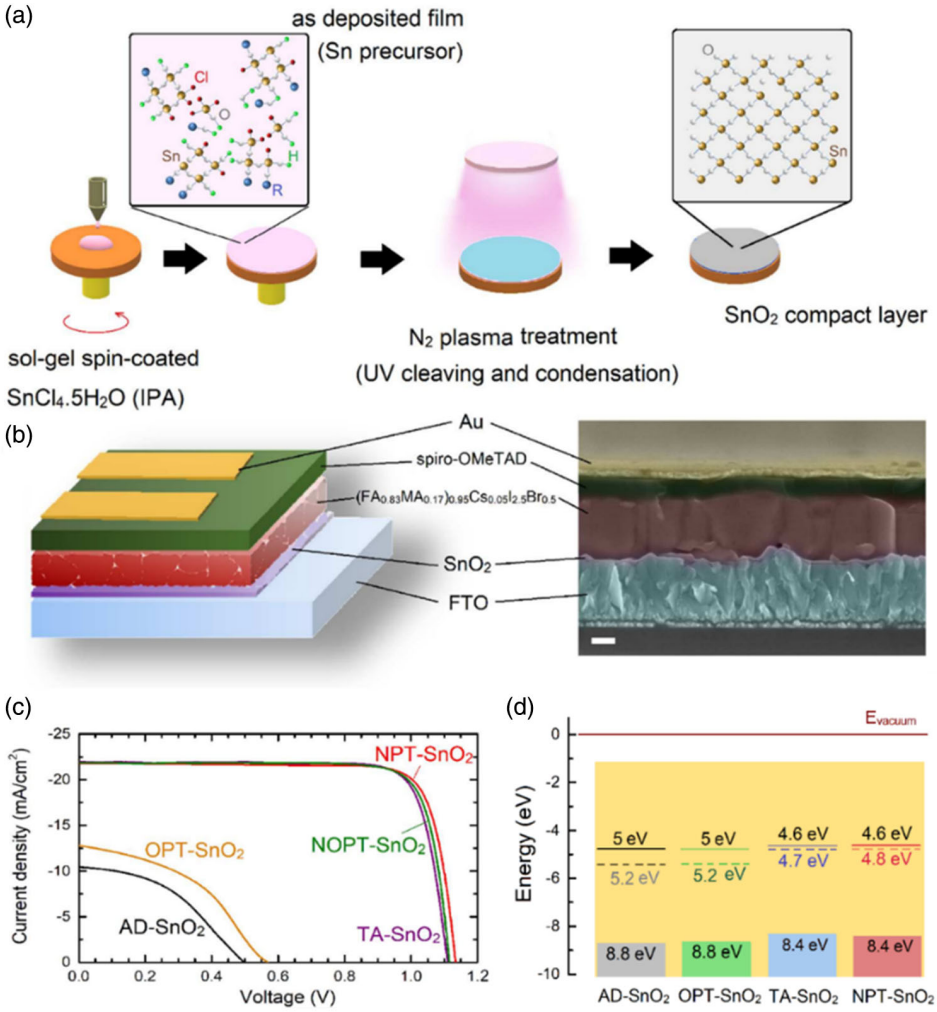

Figure 12. a) Schematic representation of the SnO_2 thin film fabrication method using the modified sol–gel technique with the exposure to low-power RF N_2 plasma for 60 minutes at an approximate 1 torr pressure. b) Schematic of the cell structure as well as the cross-section FESEM image of the PSC with SnO_2 thin film as ETL (scale bar: 200 nm). c) *J–V* curves of PSCs based on various SnO_2 thin films as ETL. d) Schematic of the suggested energy band for different SnO_2 thin films according to bandgap and UPS calculations. Reproduced with permission.[25] Copyright 2018, American Chemical Society.

flexible plastics. Moreover, the intrinsic feasibility of utilizing this method for large-area production, along with the short processing time as well as its simpatico with the substrates, makes it favorable for roll-to-roll (R2R) manufacturing platforms. Besides, light-based fast annealing strategies in PSCs, in addition to ETL, have been utilized for annealing the absorbent layer.[39] In a related study, near IR light was employed to anneal the Al_2O_3-$MAPbI_3$ absorbing layer for 2.5 s and resulted in a PCE of 10.0% in comparison with that of PSC using 45-min thermal annealing yielding 10.9% PCE.[128] Furthermore, photonic annealing for TiO_2 has been utilized and a 15% PCE was obtained[129] Likewise, Zhu et al.[39] utilized this method for annealing SnO_2 ETL films prepared through a solution-based low-temperature process on the FTO substrate. As stated by their findings, IPL annealing triggered the formation of SnO_2 films through the following reaction: ($SnCl_4 + 2\ H_2O \rightarrow SnO_2 + 4$ HCl). According to their results, IPL annealing has reduced the surface roughness and increased layer compactness. In addition to the hydroxyl groups (–OH), small amounts of chlorine were also observed in IPL annealed SnO_2 films indicating the presence of chlorinated compounds such as $SnCl_4$. So too did, Ghahremani et al.[110] applied the IPL method (5 pulses of IPL, each carrying 2.1 kJ energy) for SnO_2 annealing and also made use of this method to anneal the perovskite absorbing layer. Also, Oh et al.[130] used IPL for 30 seconds (120 pulses of IPL, each carrying 1.84 J cm^{-2} energy) for sintering of amorphous SnO_2. It should be noted that before photonic annealing, the ETL layer was dried for 1 min at 100 °C. They reported the IPL annealing reduces hydroxyl groups and increases conductivity and electron mobility. Also, their results showed that IPL annealing can effectively control the ETL/perovskite interface in a short time by regulating intrinsic perovskite ($MAPbI_3$) properties such as stress and nucleation density. Thus, they improved the PCE from 7.06% (amorphous SnO_2) to 17.68% by using photonic annealing.

3.1.5. Water Treatment

The enhancement of SnO_2 ETL through water treatment has been undertaken in three avenues comprising hydrothermal treatment, water-bath treatment, and water-spin coat treatment. In the first two methods, SnO_2 ETL is initially deposited and thereafter treated with water. However, in the water-spin coat treatment method, water pretreatment is performed prior to the SnO_2 ETL deposition.

Hydrothermal Treatment: SnO_2 film destitute of treatment suffers from poor crystallinity, which leads to low conductivity and inferior charge transport at the interface between the ETL and the perovskite adsorbing layer. Notwithstanding, surfactants are normally added to colloidal SnO_2 solutions to maintain the dispersion of SnO_2 nanoparticles. These surfactant coatings on the surface of SnO_2 nanoparticles typically lay behind high resistance in SnO_2 film and are required to be discarded appropriately. In this line, thermal annealing is a prevailing procedure; however, annealing at low temperatures (<200 °C) fails to perfectly eliminate surfactants and leads to poor PSC performance. Moreover, the majority of surfactants include organic carbon (R) compounds that could be decomposed into gaseous hydrogen fuels through hot water steam: $R + H_2O = R(O) + H_2$. Therefore, SnO_2 water steam treatment might be capable of eliminating carbonaceous surfactants. Nevertheless, conventional water-gas shift reactions require relatively high-temperature (i.e., >200 °C) treatment steps. However, the thorough abolishment of the surfactants might be met by means of the high vapor pressure of water steams in the hydrothermal process which could proceed completely at low temperatures (≤100 °C). Hot water steam thoroughly annihilates the organic surfactants coated on the surface of SnO_2 nanoparticles facilitating the formation of a ligand-free SnO_2 ETL (**Figure 13**).[131]

Recently, Liu et al.[131] exploited a novel low-cost process to prepare high-quality SnO_2 ETLs at low temperatures (100 °C) by integrating spin-coat SnO_2 nanocrystalline solutions with hydrothermal treatment. As reported from their results, the performance of SnO_2 on the rigid ITO/Glass substrate showed that the hydrothermal treated SnO_2 ETL (HT-SnO_2) at 100 °C was furthermore higher in characteristics than that of SnO_2 ETL heat annealed (TA-SnO_2) at 150 °C. They also employed this process to fabricate SnO_2 ETLs on flexible PEN/ITO substrates and achieved an outstanding champion PCE of 18.1% for PSC devices (Figure 13).

Water-Bath Treatment: In the water-bath treatment method, irrespective of the ambient humidity, SnO_2 crystalline films are to be acquired using a sol–gel thin film water bath. The precursor residues in SnO_2 films prepared in ambient air are

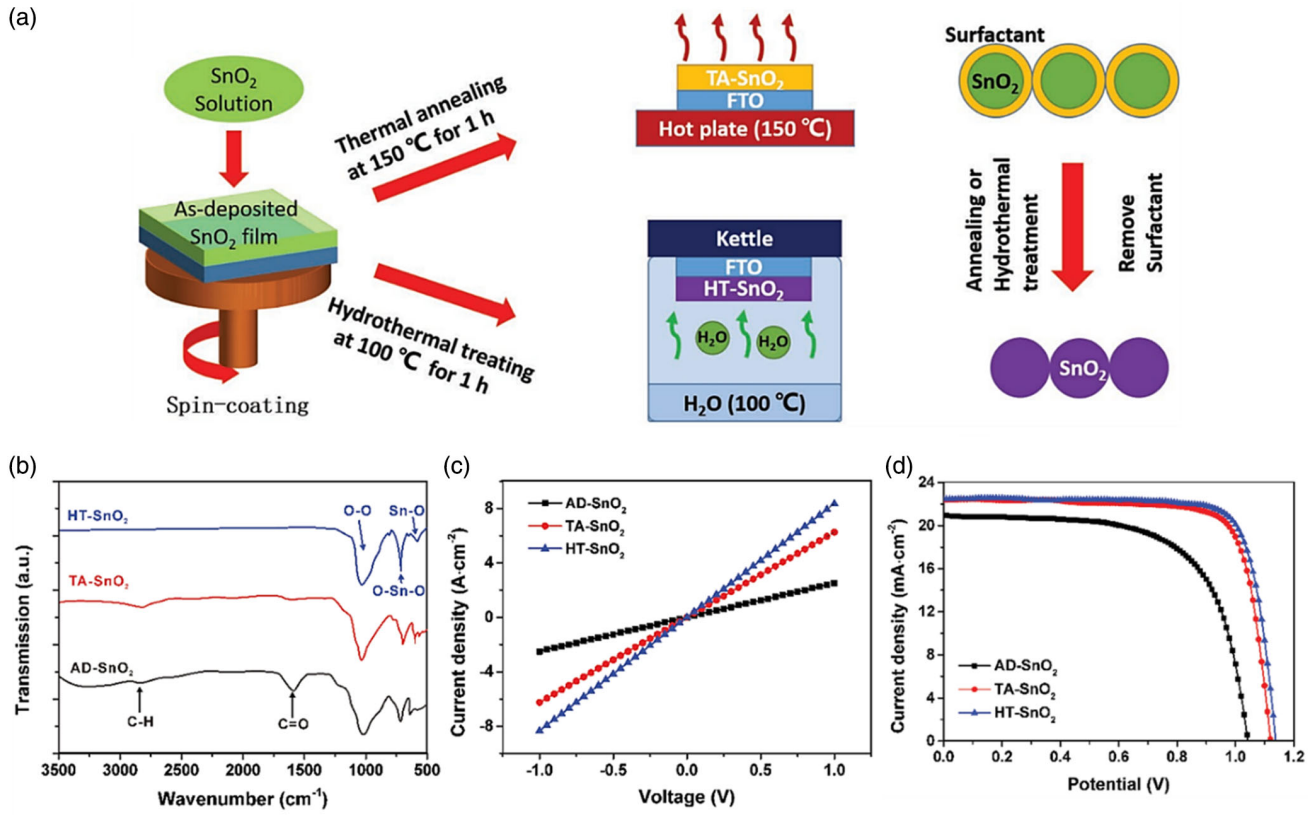

Figure 13. a) Schematic illustration of the fabrication process of SnO_2 thin film using thermal annealing or hydrothermal treatment. b) FTIR spectrum of as-deposited SnO_2 samples (AD-SnO_2), with thermal annealing (TA-SnO_2) and with hydrothermal treatment (HT-SnO_2). c) *J–V* curves of as-deposited (AD-SnO_2), with thermal annealing (TA-SnO_2), and with hydrothermal treatment (HT-SnO_2) SnO_2 films sandwiched between two gold contacts. d) *J–V* curves of PSCs using as-deposited SnO_2 films (AD-SnO_2), thermally annealed (TA-SnO_2), and hydrothermal treated SnO_2 films (HT-SnO_2) as ETL. Reproduced with permission.[131] Copyright 2019, John Wiley and Sons.

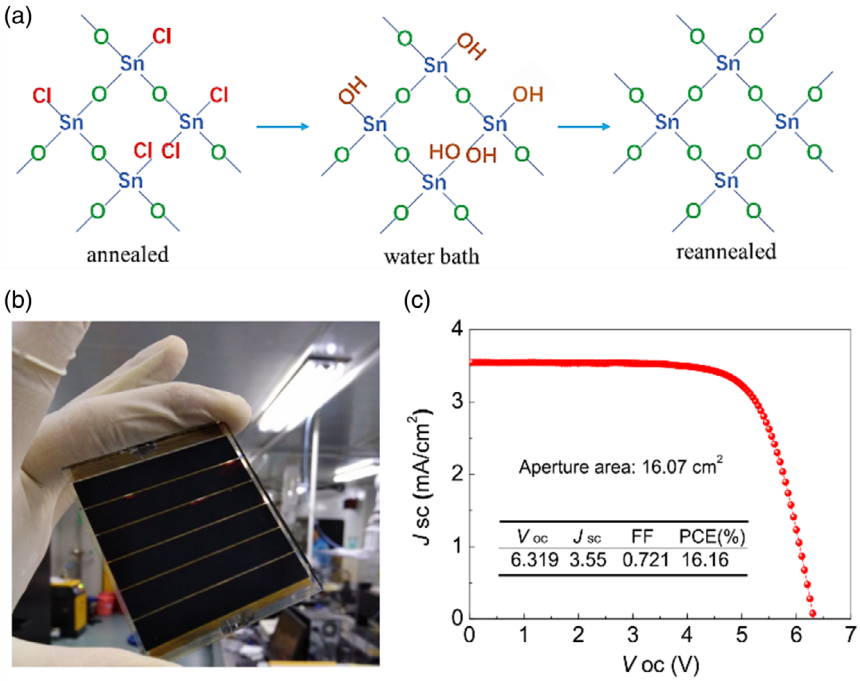

Figure 14. a) Schematic representation of the proposed reaction mechanism of SnO_2 films before and after water bath treatment. b) Picture of the large-area PSC module. c) *J–V* curve of PSC module with SnO_2 film with water bath treatment as ETL. Reproduced with permission.[121] Copyright 2018, John Wiley and Sons.

incapable of being thoroughly hydrolyzed to form SnO_2 and yet thermal annealing was applied. However, during the water-bath treatment process, the extant precursors undergo complete hydrolysis with the aid of large water molecules in the environment along with thermal energy. Thus, SnO_2 films treated with the water-bath method are composed of almost perfect crystalline SnO_2 nanocrystals, which facilitate the rapid extraction of electrons from the perovskite and the minimization of surface defects (**Figure 14**a). Therefore, the performance of the perovskite device is also remarkably improved.[121] In this line, Li et al.[121] applied this treatment on SnO_2 films prepared through spin-coating of $SnCl_4.5H_2O$/isopropanol solution in the air under diverse humidity range of 0–75% RH followed by thermal annealing at 180 °C and realized PSCs of 19.17% PCE, compared with that of devices fabricated of sol–gel thin films in the absence of water-bath treatment (i.e., 17.59%), possessing high reproducibility. Besides, using this method, they could manage to produce 16.16% PCE for the large-area PSC module with an area of 16.07 cm^2 (Figure 14b,c).

Water-Spin Coat Treatment: In the water-spin coat treatment method, ≈1—3 mL of DI water is spin-coated on the surface of the substrate preceding the SnO_2 ETL deposition not requiring subsequent annealing. The features of the SnO_2 layer largely depend on the hydrophilicity of the substrate. Moreover, SnO_2 film of fewer pinholes makes for a perovskite film having a uniform coating and a high-performance PSC. Eventhough the predominant ways such as UVO treatment are conventionally employed to produce the hydrophilicity, Wan and coworkers[99] made it through spin-coating the DI water on the substrate surface. The basis for this is, in the main, that the hydrophilic groups (–OH) are added through a water-spin coat on the substrate surface, which simultaneously favors the ductility of SnO_2 slurry to form a smooth film of high crystallinity and the enhancement of interface between SnO_2 and the substrate. Making use of this method and the consequent annihilation of pinholes and improvement of SnO_2 ETL films quality and its interface with the absorbing layer, they could successfully manage to reduce and increase the defects and charge transport in the perovskite/SnO_2 ETL interface, respectively, and realize PSC of 19.68% efficiency.

3.1.6. Sulfur Treatment

The sulfur treatment has been utilized for passivating the interface between ETL and perovskite. Also, solvents or sulfur-containing molecules have been employed directly to modify the perovskite layer. Sulfur-containing compounds extending from thiophene,[132] thiadiazole,[133] and thiourea[134] are capable of forming adducts with PbI_2 (a Lewis acid) in perovskite compound by interacting with a sulfur-bearing Lewis base.[135] Therefore, this would conduct to the elimination of deep traps and increment in the passivation between grain boundaries and perovskite crystallinity. Sulfur could be directly coordinated with lead atoms in the perovskite thereby interacting with the perovskite valence band, facilitating the efficient extraction of carriers from the perovskite and increasing the PSC efficiency.[132] Moreover, poor interaction between lead and sulfur (R2C = S·PbI_2) might regulate the perovskite nucleation and crystal growth.[133,134]

In the utility of sulfur treatment for the modification of the perovskite/SnO_2 interface, sulfur atoms would make bonding to Pb^{2+} in perovskite and SnO_2 simultaneously and, owing to resultant chemical interaction, lead to improved charge transport at the perovskite/SnO_2 interface. Although complex organic molecules such as heparin sodium[136] biopolymer are also utilized to facilitate accelerated charge transport in the interface as well as reduce hysteresis, plausible defects in the interconnections of organic molecules constrain the effectiveness of surface trap passivation which is undesired for the performance of the perovskite photovoltaic devices. Furthermore, sulfur mineral atoms at the SnO_2 surface have been reported to hold stronger electrostatic interactions with Pb in the perovskite than that of oxygen atoms in the SnO_2 ETL.[29] Actually, surface sulfur atoms desist traps in the shallow area and carrier recombination at the interface through filling the iodide vacancy at the interface. In order to apply the sulfur treatment on SnO_2 to functionalize it at relative humidity above 60% (RH), Wang and coworkers[102] loaded a solution of potassium O–hexyl xanthate in methanol on the SnO_2 surface for two minutes and then spin-coated. Subsequently, after three washes with methanol, the samples were annealed at 130 °C minutes to decompose xanthate (**Figure 15**a,b). According to the group, the surface of SnO_2 film came to be more hydrophilic owing to sulfur treatment and the decomposition of tin xanthate and the formation of tin sulfide, which stemmed from an affinity change from hydrogen to sulfur bonds. Moreover, sulfur treatment reduced the work function of SnO_2, which resulted in a superior energy band alignment between the perovskite and the ETL. Accordingly, the research group has attained PSCs possessing 18.41% PCE using sulfur treatment (Figure 15c).

To that end, Ai et al.[137] utilized $(NH_4)_2S$ for SnO_2 ETL sulfur treatment to passivate surface defects. They admixed different concentrations of $(NH_4)_2S$ in SnO_2 precursor colloids and subsequently prepared SnO_2 ETLs using the spin-coating method and annealed at 180 °C. Within SnO_2 ETL, there lie a great deal of lateral Sn bonds, and after applying the $(NH_4)_2S$ to SnO_2 colloids, the surface S atoms would impregnate the surface lateral Sn bonds to form the S–Sn bonds. Therefore, the formation of S–Sn bonds could partially eliminate surface oxygen vacancies. Furthermore, S–Sn surface bonds can harness the moisture diffusion into the cell, as shown in **Figure 16**. In addition, the anchor S bonds of the surface Sn–S bonds make bondage with lead atoms in the perovskite crystal process to form Sn–S–Pb. These anchors establish an interconnection from the perovskite directly to the ETL as a pathway for electron transport which thus improves electron extraction. This method reduces the density of surface defects in ETL, thereby removing electron transport obstacles and improving electron mobility and thus conductivity and stability. Conclusively, the research group could manage to achieve a PCE of over 20% making use of this sulfur treatment.

3.1.7. Self-Assembled Monolayer Treatment

In the self-assembled monolayer (SAM) treatment, the insertion of an interlayer in the perovskite/ETL interface would make for

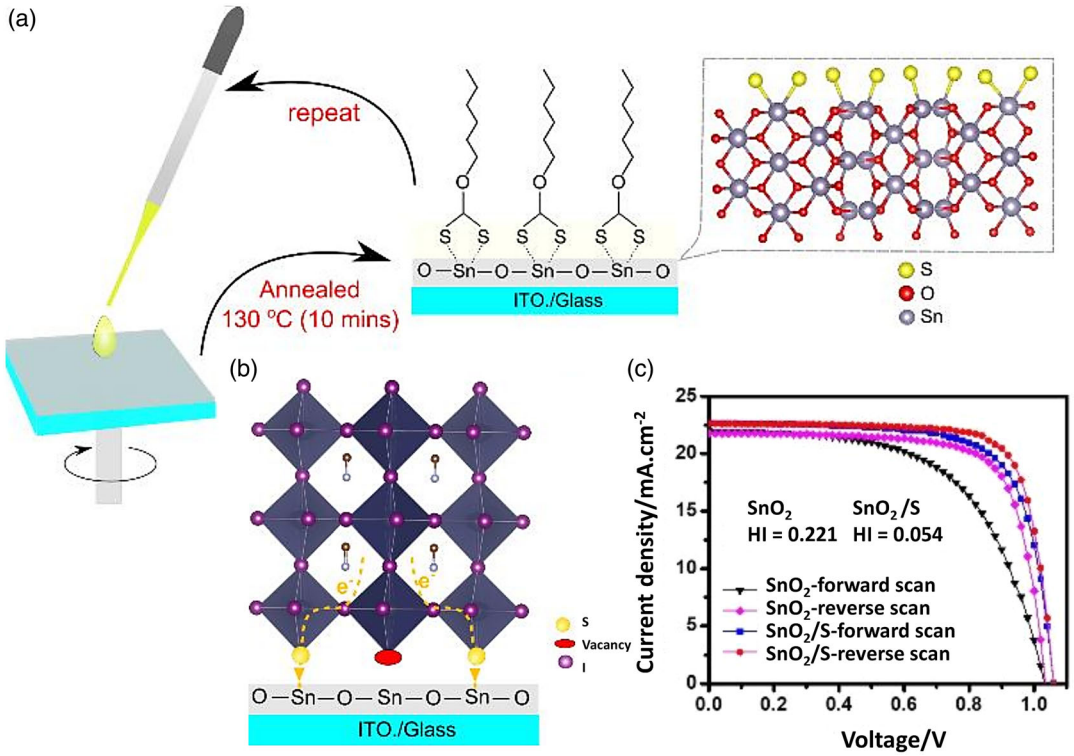

Figure 15. a) Schematic representation of sulfur treatment (sulfur functionalization) of ETL by xanthate annealing. b) Schematic illustration of the interface of the cell. c) Comparison of *J–V* curves for PSC using SnO_2 film with and without sulfur treatment as ETL (the hysteresis index (HI) value is noted in the figure). Reproduced with permission.[102] Copyright 2018, John Wiley and Sons.

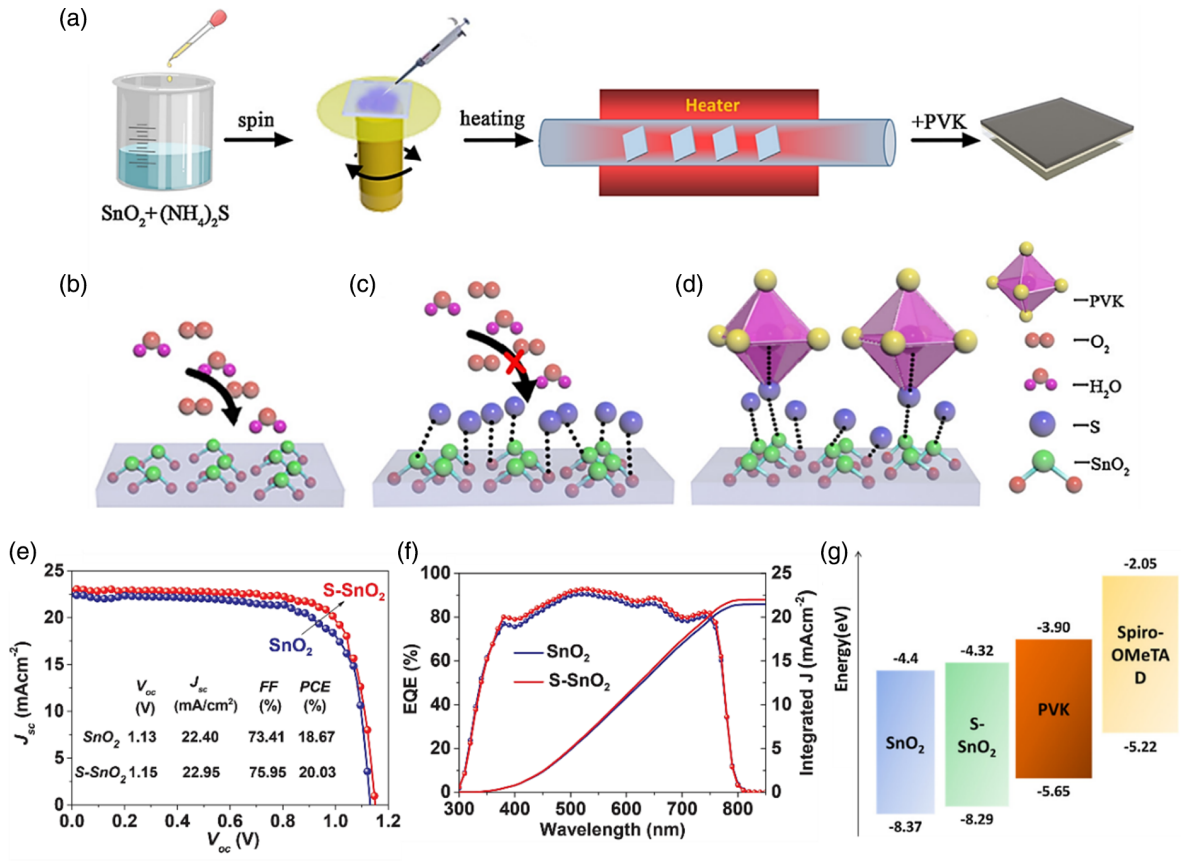

Figure 16. a) Schematic representation of the one-step deposition of modified SnO_2 ETL. The interface modification mechanisms using sulfur treatment: b) the diffusion of O_2 and H_2O into the SnO_2 surface. c) Formation of S–O and S–Sn bonds preclude the diffusivity of H_2O and O_2. d) Formation of Sn–S–Pb anchors to reduce the surface traps state. e) *J–V* curves, f) EQE, and g) energy bands for PSCs built on SnO_2 and sulfur-treated SnO_2 (S-SnO_2) as ETL. Reproduced with permission.[137] Copyright 2019, Elsevier.

the energy-level adjustment, the surface energy modification, and the enhancement of the films or substrates affinity. Moreover, this treatment has been utilized as a surface modification method in organic solar cells[138] and dye-sensitized solar cells.[139] SAM treatment is also reported to impress beneficial effects upon the interface modification and this is accomplished through manipulating the energy levels by creating a dipole moment at the interface.[140] Also to be found, it could also passivate the inorganic surface states using chemical bonds thus regulating surface electrical states. Furthermore, SAM treatment could exert influence on the growth process of organic semiconductors and make for various morphologies. Accordingly, SAM treatment has been employed as a streamlined procedure to optimize the SnO_2 ETL/perovskite interface in planar PSCs.[141,142] In general, SAMs molecules consist of three parts: anchoring, terminal, and spacer groups. The anchoring group can interact with the modified interface level and affect electronic performance and ETL specifications. The terminal group with perovskite layer can have interfacial chemistry and thus affect the quality of perovskite adsorbent film and carrier dynamics PSCs. The spacer group connects the anchoring and terminal groups and affects the attenuation rate of the transport.[143]

Si-Based Self-Assembled Monolayer Treatment: Yang et al.[142] had utilized the Si-based SAM treatment to modify the perovskite/SnO_2 ETL interface in which 3-aminopropyltriethoxysilane (APTES) SAM was employed as an interlayer for the modification of the interface between the SnO_2 ETL/perovskite layer. To do so, the prepared SnO_2 compact films were immersed in APTES solution in isopropanol (5 mM), then washed with isopropanol, and finally dried under N_2. The fabricated SAM layer enhanced the contact surface at the interface and improved the morphology and crystallization of perovskite films. Moreover, through the formation of dipoles, the functionalized APTES SAM could manage to give onto the tuning of energy band alignment, increment of the built-in potential, and reinforcement of the driving force to segregate the photo-produced carriers and thus accelerating the charge extraction (**Figure 17**b). With regard to the multifunctional character of APTES SAM, alkyl chains acted as an electrical insulation barrier thus intercepting the backward electron transport from the electrodes to the perovskite layer and remarkably reducing recombination processes. Likewise, the terminal groups passivated the trap states at the perovskite surface through hydrogen bond interactions (N–H...I) (Figure 17a) thus reducing the charge accumulation and recombination resulting from them. In conclusion, the result of the research works was

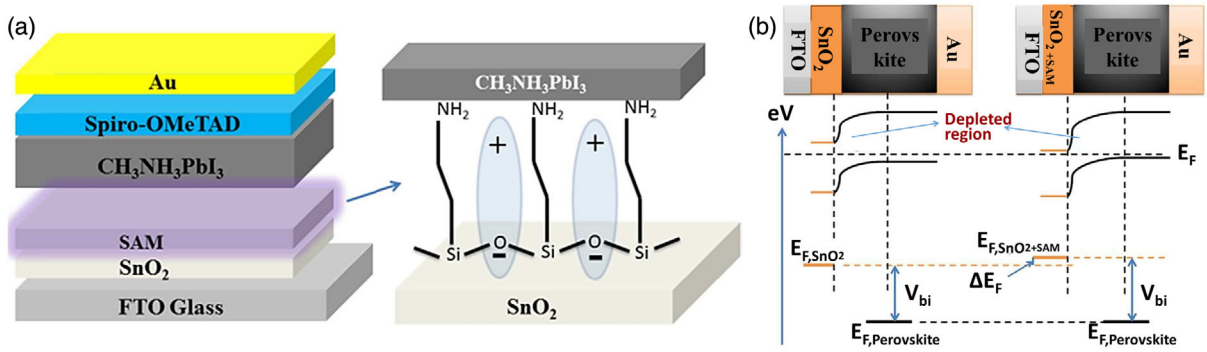

Figure 17. a) Schematic illustration of the PSC based on SnO_2 ETL with APTES SAM treatment. b) Schematic representation of band diagram in equilibrium for perovskite heterojunction with SnO_2 with and without APTES SAM treatment. The corresponding depletion areas and built-in voltages are demonstrated. Reproduced with permission.[141] Copyright 2017, John Wiley and Sons.

the achievement of a high PCE of 18% as well as low hysteresis for planar PSC using the surface treatment of SnO_2 with APTES SAM.

C_{60} Self-Assembled Monolayer Treatment: Fullerene (C_{60}) and its derivatives, such as PCBM, are the wide-utilized ETLs in invert structured PSCs in which they are highly efficient in electron extraction owing to their high mobility.[142] Besides, fullerenes could passivate surface defects of the perovskite layer.[88] The lower energy position of the SnO_2 conduction band than that of the $MAPbI_3$ perovskite conduction band by about 0.6 eV leads to undesired charge accumulation and recombination throughout charge transfer at the perovskite/SnO_2 interface.[144] The application of C_{60} SAM as a surface treatment in the SnO_2/perovskite interface would establish a firm electrical connection between SnO_2 and C_{60} SAM governing the surface properties of SnO_2 including the passivation of surface defects and reduction of ion migration.[88] Likewise, C_{60} SAM could set up a more perfect energy band alignment between the perovskite and C_{60} which leads to a facilitated electron extraction and transport from the perovskite to SnO_2, alleviating nonradiative recombination, and reducing hysteresis.[144,145] In addition to SnO_2, the utilization of C_{60} SAM for other ETLs such as TiO_2[146] and ZnO[147] have also been reported in the literature as surface treatment. In 2014, Snaith et al.[146] employed C_{60} SAM to reduce trap states at the TiO_2/perovskite interface, resulting in a more efficient charge generation process and expeditious pathway of electron transport. Notwithstanding the effectiveness of the C_{60} SAM treatment, it is not compatible for upscaling and mass production due to the long anchoring time required for SAM.[88] Accordingly, Liu et al.[63] prepared high-transparency SnO_2 layers using the dual-fuel fuel combustion method. Through the modification of SnO_2 layers with C_{60} SAM treatment, they were able to achieve a champion 15% PCE as well as negligible hysteresis.

Zwitterion Self-Assembled Monolayer Treatment: Zwitterion is a molecule that contains an equal number of positively- and negatively charged functional groups thereupon neutral. Choi et al.[148] reported a planar PSCs with zwitterion SAM-modified SnO_2 ETL of thermal stability and high efficiency. Therein, the zwitterionic compound, 3-(1-pyridinio)-1-propane sulfonate (NDSB-201), was utilized to surface modify SnO_2 ETL. Hydroxyl groups on the surface of SnO_2 chemically react to form bonds with zwitterion molecules containing anions such as–COO^-, –SO^{3-}, and –SO^{4-}. Consequently, the zwitterion SAM treatment of the SnO_2 ETL leads to the formation of surface dipoles, the shifting of the SnO_2 ETL work function, the inhibition of electron transport, and the abatement of charge recombination (**Figure 18**). Besides, zwitterion passivates perovskite Pb–I antisite traps using its positively charged atom and improves the thermal stability of the PSC. In culmination, this research group managed to obtain PSCs possessing PCE of 20.91% and 21.43% using Zwitterion modification of SnO_2 ETL prepared by spin-coating of tin chloride precursor solution and CBD, respectively.

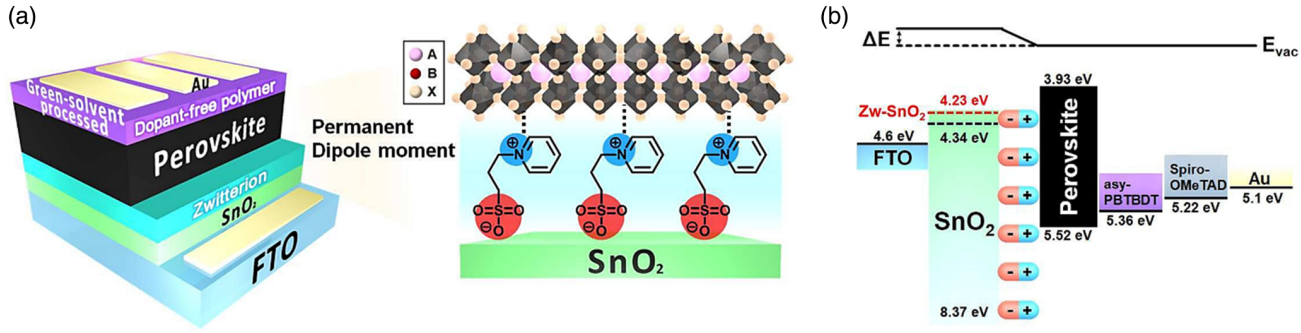

Figure 18. a) Schematic representation of the zwitterion SAM treatment of SnO_2 layer. b) Energy diagram of each layer, formation of surface dipoles, and the work function shifting of SnO_2 modified with zwitterion SAM. Reproduced with permission.[148] Copyright 2018, Royal Society of Chemistry.

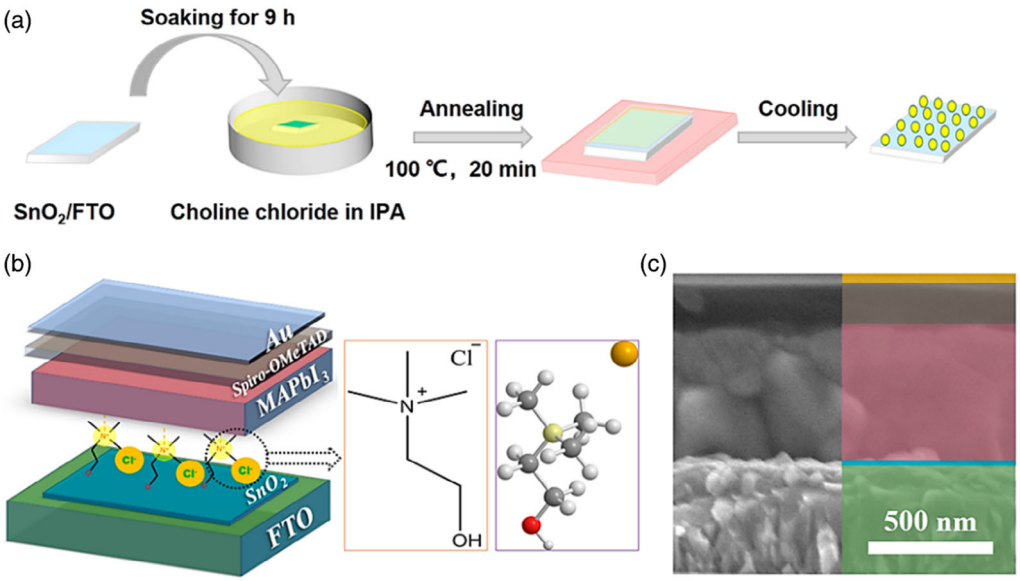

Figure 19. a) Schematic illustration of the choline chloride SAM treatment process on the SnO_2 layer. b) Schematic diagram of the formation of choline chloride SAM on the SnO_2 layer and three-dimensional structural diagram of choline chloride, and c) cross-section SEM image of PSC built on choline chloride SAM-treated SnO_2 ETL. Reproduced with permission.[150] Copyright 2020, American Chemical Society.

Zhao et al.[149] also used another material called diethylenetriaminepentakis (DETAPMP) to modify SnO_2 ETL surface. The phosphate group present in DETAPMP reacts with SnO and passively forms the SnO_2 defect by forming an ester bond. In addition, the ammonium group in DETAPMP balances the PbI_3^- charge and passivates the PbI_3^- defects. This group could reduce charge recombination and increase charge transport by improving the SnO_2 ETL layer zwitterion modification by DETAPMP, increasing the PCE from 17.74% to 20.02%. Also, by changing the absorber layer from $MAPbI_{3-x}Cl_x$ to $(FAPbI_3)_{0.95}(MAPbBr_3)_{0.05}$, they were achieved a yield of 21.65%.

Choline Chloride Self-Assembled Monolayer Treatment: Naturally occurring, choline chloride is a plant photosynthetic promoter substantively reverberating the plant performance increment. In this line, choline chloride increases electron transport in photosynthesis in thylakoid membranes, thereby conducting the synthesis of adenosine triphosphate (ATP) in chloroplasts. Inspired by this biological substance, Yan and their coworkers[150] made use of choline chloride SAM in PSC (**Figure 19**a,c). Supposedly, its performance in PSC is analogous to that of plant photosynthesis promoter in which improved electron transport and enabled ETL to extract electrons more efficiently. Furthermore, the utilization of this material in the ETL/perovskite interface serves to passivate oxygen vacancy defects at the ETL surface. Besides, choline chloride SAM anchors on SnO_2 ETL to impose a chemical interaction with the perovskite film (Figure 19b), which remarkably reduces the oxygen vacancies at the interface and improves electron transport, carrier lifetime, and open-circuit voltage (V_{OC}) of PSC. Besides, SnO_2 ETL modified with choline chloride SAM treatment could better the charge extraction, reduce recombination in the ETL/perovskite interface, and improve the quality of ETL and perovskite films.[150]

Thiol Silane Self-Assembled Monolayer Treatment: Shi et al.[143] used 3-mercaptopropyltrimethoxysilane (MPTMS) SAM as the material for the thiol silane SAM treatment, included three functional methoxy groups as the anchoring group, and one sulfhydryl group as the terminal group. Through the coordination of sulfhydryl groups in MPTMS with PbI_2, the perovskite crystal growth is slowed down and the crystal size of perovskite films is enlarged. MPTMS also smoothed out SnO_2 ETL surface and improved the quality of perovskite absorber films. In addition, S atoms in MPTMS anchor the Pb atoms, increasing the photo-electron extraction. The methoxy groups hydrolyzed on MPTMS reacted condensation with hydroxyl groups on the SnO_2 surface, thereby strengthening the perovskite structure. Thus, they increased the PCE from 16.24% to 20.03% by using thiol silane SAM treatment.

Carboxylic Acid-Based Self-Assembled Monolayer Treatment: Zhang et al.[151] examined and compared the performance of three molecules based on thiophene 3-thenoic acid (TA1), thiophene-3-acetic acid (TA2), and 3-thiophenepropanoic acid (TA3) as interlayer between SnO_2 ETL/Perovskite. These three molecules have thiophene and carboxylic acid functional groups, the structure of which is similar except for the length of the alkyl chains. Different lengths of alkyl chains affect the bipolar momentum of these molecules, leading to a change in the band structure of the SnO_2/perovskite interface in PSCs. These bipolar momentums, together with electron donation from thiophene rings to SnO_2, change the electronic states of the SnO_2 surface. Also, S atoms on thiophene rings with a pair of electrons bind only to Pb ions in the perovskite and –COOH terminal groups to SnO_2 ETL. Thus, they reported that carboxyl groups were able to passivate surface –OH terminal groups in SnO_2, which reduced nonradiative recombination and severe energy loss (E_{loss}) at the SnO_2/perovskite interface. These molecules with different dipole

momentum cause band bending at the SnO_2/perovskite interface, which facilitates load transfer and reduces E_{loss}. Also, the bonding of the S atoms in the thiophene ring with the lead atoms may have controlled the crystallization process of the perovskite film, leading to a reduction in undercoordinated Pb^{2+} defect states and better perovskite film quality. They report that the bipolar momentum of these molecules has altered the working function of SnO_2 ETL, in which the TA2 molecules with the highest bipolar momentum have the best effect and play an important role in facilitating transport and reducing charge recombination at the SnO2/perovskite interface. Using TA1, TA2, and TA3 molecules as interlayers, the efficiency of LT-SnO_2-based PSCs increased from 17.54% to 19.59%, 20.61% and 18.67%, respectively.

Ye et al.[152] used a combination of anchorable compounds of perylene diimides (PDI) and naphthalene diimide (NDI) along with carboxyl group-terminated anchoring chains for LT-SnO_2 surface treatment in PSC structures and compared their performance. These compounds are n-type organic semiconductors because the strong electron-acceptor imide groups decorated on conjugated polyaromatic hydrocarbons can significantly stabilize their HOMO and LUMO energy levels. Compared to NDI, the PDI core has a longer effective conjugation length, which due to the increased charge delocalization will be useful for further stabilization of the LUMO level and increase charge transfer. The group used three types of amino acids (β-aminopropionic acid, L-2-aminopropionic acid, and L-aspartic acid) to react with perylene-3,4,9,10-tetracarboxylic dianhydride and prepared the compounds PDI-P, PDI-LP, and PDI-LAS, respectively, containing anchoring chains with carboxylic acid as the terminal group on the nitrogen atom of the imide moiety. The n-type anchoring assembly-based organic semiconductors are chemically inert to perovskite and thus prevent adverse surface chemical reactions to achieve the excellent thermal stability of PSCs. According to their results, carboxylic acid groups can not only chemically adhere to the surface of indium tin oxide (ITO) electrode and increase the stability of organic ETL but also provide a hydrophilic contact to facilitate perovskite thin film deposition. The results of this group showed that, compared to NDI, LUMO energy levels PDI analogs had better alignment with the CB edge of the perovskite, reducing the electron transfer barrier and facilitating electron extraction. On the other hand, PDI-P based on linear anchoring chain has also performed poorly in ETL preparation due to poor solubility. Based on the results, the combination of branched anchoring chains could effectively solve the problem of solubility of PDI compounds and facilitate their solubility. In addition, perovskite crystallization was improved by increasing the number of anchoring groups.

3.1.8. Alkali Metal Treatment

In recent years, a great deal of research studies has demonstrated that doping with an alkali metal, especially potassium, imposes a positive effect upon PSCs performance.[105,153–156] Thereby, the addition of compounds including potassium halide (e.g., KI, KBr) to perovskite precursors make them incorporate potassium ions into the perovskite. As a consequence of potassium ions incorporation, the crystalline quality and light absorption of perovskite increase and the amount of trap states decreases.[153] Likewise, Bu et al.[26] examined the commercial colloidal solution of Alfa-SnO_2 and realized that a small amount of KOH was added to the solution for colloidal stability. In consequence of this addition, the perovskite/ETL interface would be passivated which, in turn, outstanding performance and a significant reduction in the hysteresis of PSCs based on Alfa-SnO_2 ETL was observed. Likewise, Wang et al.[156] applied a very thin layer of KCl as a buffer layer between the SnO_2 ETL and the perovskite (**Figure 20**a). According to their results, since the MA^+ cations and I^- anion take the possibility to immigrate and move in the perovskite and also, due to the smaller size of K^+ cation and Cl^- anion than that of MA^+ and I^-, the formers could easily diffuse and move into the absorbent layer throughout thermal annealing of the perovskite layer. According to the Goldschmidt tolerance factor, $KPbI_3$ and $KPbCl_3$ are incapable of forming a stable perovskite structure since the size of the K^+ cation (1.33 Å) is even smaller than that of the rubidium cation (1.48 Å). Therefore, the K^+ cation is inclined to reside and move at the interstitial site in the perovskite, whereas the Cl^- anion might either fill the halide vacancy states or remain in the interstitial position, as shown in Figure 20b. What is more, several trap states have proven to be formed during perovskite crystallization, particularly at the interface and grain boundary of the perovskite layer

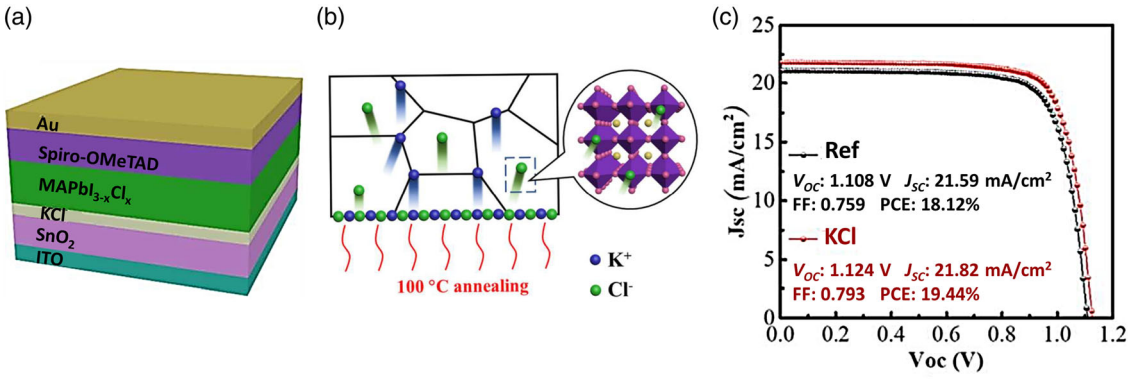

Figure 20. a) Schematic illustration of PSC based on SnO_2 ETL with potassium treatment. b) Schematic representation of the motion of K^+ cation and Cl^- anion in perovskite and c) comparison of *J–V* curves for PSC employing SnO_2 film with and without potassium treatment as ETL. Reproduced with permission.[156] Copyright 2018, Royal Society of Chemistry.

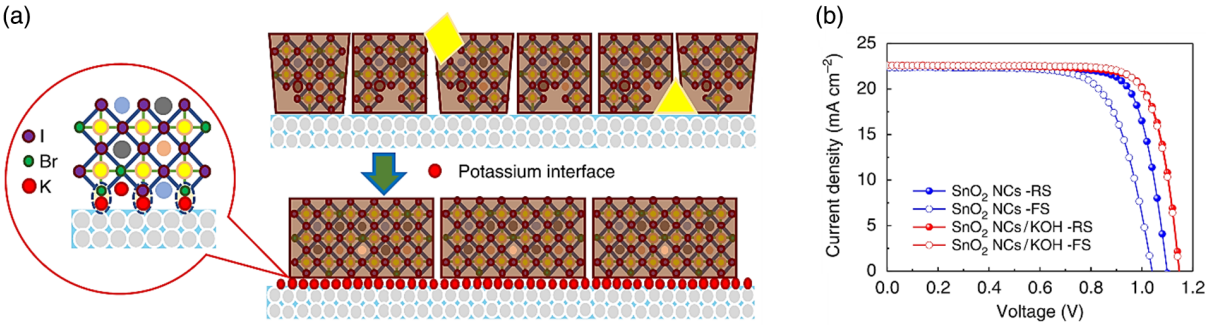

Figure 21. a) Schematic image of the perovskite growth process on different substrates without and with potassium interface. b) Comparison of *J–V* curves for PSC with SnO_2 film with and without potassium treatment (KOH) as ETL. Reproduced with permission under the terms of the Creative Commons CC BY license.[26] Copyright 2018, the Authors. Published by Springer Nature.

in which the diffusivity of the K^+ cation and the moving Cl^- anion should passivate these trap states and decorate the surfaces and grain boundaries as well. In this end, the research team was able to achieve PSCs of 19.44% PCE utilizing potassium treatment of SnO_2 ETL prepared by spin-coating the tin chloride precursor solution (Figure 20c).[156]

Correspondingly, Bu et al.[26] investigated the impact of K^+ cation through the deposition of potassium-containing compounds between SnO_2 ETL and perovskite(**Figure 21**a). On the contrary to preceding findings, they supposed that K^+ possessed a much more effective share than Cl^- anion in passivation, thereupon, nonhalide compounds such as KOH and KCH_3COO were employed to assert the claim and obtained analogous results with that of potassium halide. In consequence, they realized that the presence of K^+ cations in the SnO_2 ET/perovskite interface remarkably impressed upon the germination and growth of the perovskite layer. Moreover, potassium treatment leads to the formation of larger grains, a smoother surface, and the removal of PbI_2 impurities in the perovskite layer. Besides, they reported that, given the strong ion bond of KBr, K^+ cations hold the potential to easily react with Br ions through substitutional reaction to form KBr at the surface of the perovskite film. Thereby, KBr-rich interfaces could passivate the halide vacancies of the interface and enhance the PSC performance along with hysteresis abatement. Moreover, the strong KBr dipole preferentially binds to PbX_2 (Figure 21b) and serves as the nuclei for perovskite formation. Besides, Br-leaching of the perovskite film could provide the ground for the formation of I-rich perovskite, thereby expanding the perovskite crystal network by more incorporation of I^-. This might explain the manner in which PbI_2 impurities in the perovskite layer was removed. In conclusion, the group could obtain PSCs possessing PCEs of 20.50%, 17.18%, and 14.89% using potassium treatment for slot-die printed SnO_2 ETL on the rigid, small-size flexible (0.16 cm^2), and large-size flexible (16.07 cm^2) substrates, respectively.[26]

Recently, Huang et al.[105] have also systematically reported the influence of alkali metals (i.e., Li, Na, K, Rb, and Cs) in modifying the interface of PSCs. To modify the SnO_2 films, chloride salt solutions of each alkali metal were spin-coated on the surface of SnO_2 and then annealed at 150 °C. Based on the results therein, the surface roughness increased upon the increasing radius of alkali metal, and the conductivity of SnO_2 films in the presence of Na was higher than that of the other alkali metals owing to the higher conductivity of this element. The performance of PSCs based on SnO_2 ETL treated with alkali metals involving Li, Na, and K with PCEs of 18.29%, 18.57%, and 18.67%, respectively, was higher than that of PSCs built upon untreated SnO_2 ETL possessing 17.84% PCE. This is since alkaline metals incorporation has led to a decrement in the density of trap states as well as an increment in the mobility of the SnO_2 layer. However, PSCs based on SnO_2 ETL treated with alkaline metals including Rb and Cs, representing PCEs of 17.85% and 17.83%, respectively, fared poorly to demonstrate significant results compared to that of PSCs based upon untreated SnO_2 ETL.[105]

3.1.9. Halogen Treatment

SnO_2 film, much the same as other metal oxides (e.g., TiO_2, ZnO), bears oxygen-induced bulk and surface defects that might frustrate their electronic and charge transport properties.[150] The presence of halogens such as chlorine on the surface of SnO_2 ETL not only reduces surface defects in the ETL/perovskite interface but also constructs a bridge for electron transfer from the perovskite film to that of SnO_2 ETL.[120,157] Ren et al.[120] subjected the SnO_2 film into 1,2-dichlorobenzene solution as a source of chlorine under UVO for the chlorine treatment of SnO_2 ETL. The 1,2-dichlorobenzene solution is of high reactivity Cl radicals, which could enable deeper passivation, thus by bonding the chlorine anion to Sn on the SnO_2 ETL surface.[120] For bromine treatment of SnO_2 ETL, Liu et al.[157] placed the SnO_2 film in a solution of methanol containing 1-butyl-3-methylimidazolium bromide as a source of bromine in a nitrogen glove box. Thus, they were able to increase the PSC efficiency from 16.8% to 18.8% with bromine treatment.[157]

3.1.10. Amine-Based Treatment

In recent years, the amino acid ($HOOC\text{-}R\text{-}NH_2$) utility has been reported as a buffer layer in the ETL/perovskite interface for TiO_2 and ZnO ETL-based PSC devices.[147,158] The role of amine-based compounds has a close analogy to that of "linker" between ETL and perovskite. Furthermore, amine-based compounds could induce favorable growth of perovskite crystals and thus increase perovskite crystallinity.[34] However, modification of SnO_2 ETL

using the buffer layer of amine-based compounds and their role in manipulating the crystal lattice has been rarely reported.

Generally speaking, annealing of the SnO_2 layer for decreasing oxygen vacancies is performed in ambient air, which inevitably leads to the adsorption of oxygen on the SnO_2 nanocrystalline film.[86] The physical adsorption of these ambient oxygen molecules metamorphoses to chemisorption on the surface of SnO_2 through effectively extracting intrinsic electrons from the SnO_2 conduction band during the annealing process promoting the formation of O^{2-} on the surface. Therefore, a band bending and an energy barrier are formed between the perovskite and SnO_2 interface resulted in a significant reduction in SnO_2 conductivity. Due to the negative O^{2-} adsorbed charge, further charge recombination at the ETL/perovskite interface hinders the transport of electrons produced in the perovskite layer into SnO_2 and reduces the device efficiency.[159,160] On one side, a cation (i.e., positive charge) is required to compensate for this effect and tackle the issue. On the other side, it has been reported that the substitution of A-site ions in perovskite with multifunctional guanidinium cation would enhance the stability and performance of the device.[161] Besides that, as a large organic cation, the positive charge of guanidinium forms a strong bond with O^{2-} whereas the ammonium in guanidinium could form a firm hydrogen bond with iodide in the perovskite (**Figure 22**a,c). Consequently, the application of guanidinium as a linker in the SnO_2 ETL/perovskite interface can curb the energy barrier of charge transport stemmed from O^{2-} between SnO_2 and perovskite.[162] To accomplish guanidinium treatment, Yu et al.[162] initially spin-coated the guanidinium chloride solution on SnO_2 film and then annealed it at 80 °C. In consequence, guanidinium treatment enhanced the wettability of the SnO_2 layer in light of the formation of a strong hydrogen bond (N—H... I^-) between the amino groups of the guanidinium interlayer ions and the perovskite precursor iodide ions, as depicted in Figure 22c.

Although SnO_2 offers numerous merits as ETL it suffers from certain drawbacks common in metal oxides whatsoever including surface oxygen vacancies and containing surface hydroxyl groups making for trap states adjacent to the valence band.[104] According to the literature,[104,163] two types of hydroxyl groups on the metal oxide surface have been reported involving terminal-hydroxyls (OHT), which binds to one metal site of basic properties, and bridge-hydroxyls (OHB), which binds to two acidic metal sites. The presence of OHT on the hydroxylated surface creates deep energy states in the bandgap (**Figure 23**a), which behave as traps that result in the production of nonradiative recombination and energy loss. Thereupon, diminishing the defect sites on the SnO_2 surface is of paramount importance since they could engender nonradiative recombination in the

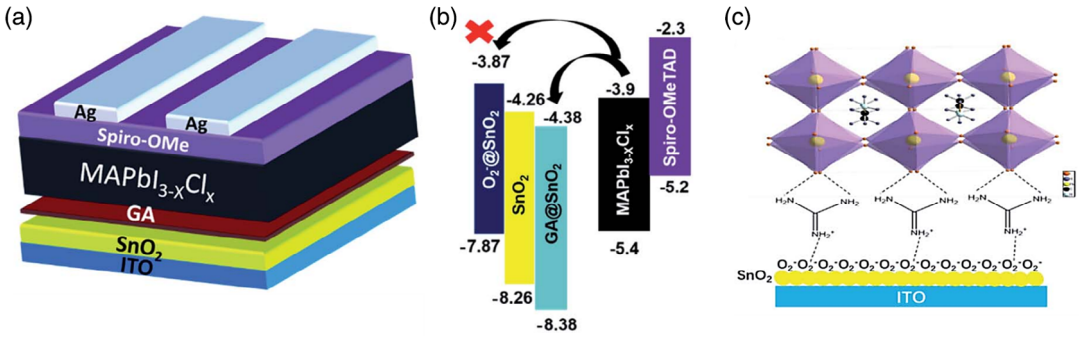

Figure 22. a) Schematic representation of a PSC built on SnO_2 ETL with guanidinium (GA) treatment. b) Schematic illustration of the relative vacuum-level energy band diagram for SnO_2, treated SnO_2 (GA@SnO_2), and SnO_2 with O^{2-} (O^{2-}@SnO_2) films. c) Schematic representation of guanidinium coating on SnO_2 layer. Coupling of positive charges in guanidinium and negative charges of chemisorbed oxygen O^{2-}, the two amine-based groups remnant in guanidinium interact with the iodide anion in the perovskite layer. Reproduced with permission.[162] Copyright 2020, Royal Society of Chemistry.

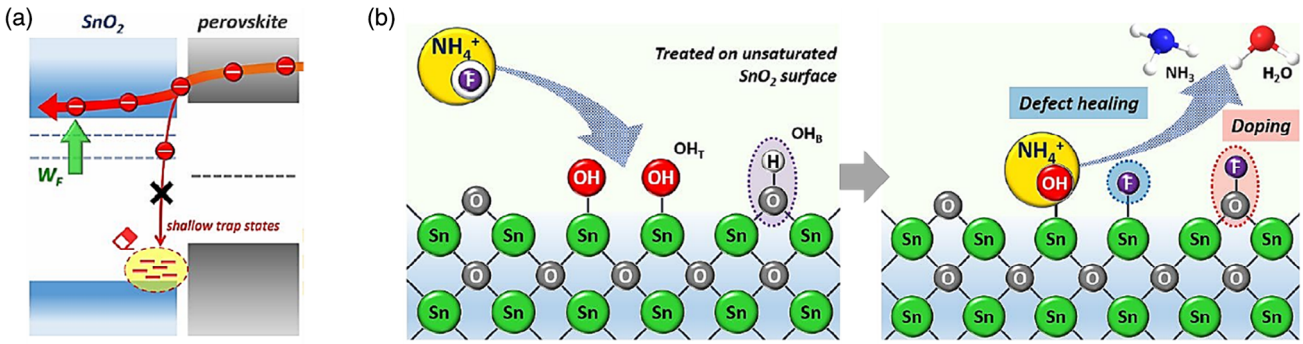

Figure 23. a) Schematic representation of the effect of NH_4F treatment on the work function and trap states in the SnO_2 bandgap and electron charge transport at the perovskite/SnO_2 interface. b) Schematic depiction of SnO_2 film treatment with NH_4F. Reproduced with permission.[104] Copyright 2020, American Chemical Society.

SnO_2/perovskite interface. However, adjusting the SnO_2 energy level through doping allows the enhancement of electron extraction from the perovskite.[104,164,165] Inspired by the thought of fluorine-doped SnO_2 (FTO) preparation through interaction between tin(IV)tetrahydroxide ($Sn(OH)_4$) and ammonium fluoride (NH_4F), surface treatment of SnO_2 with NH_4F could alleviate defect sites and regulate the Fermi level of SnO_2 thin films. Moreover, this treatment could annihilate hydroxyl groups from the SnO_2 surface and also dope it with fluoride ions (Figure 23b).[104] It is possible that the weakly acidic ammonium cation of NH_4F reacts with OHT on the SnO_2 surface producing ammonia gas and water vapor and replacing the fluoride anions at the defect sites, which regulates the SnO_2 energy level.[104] In this manner, four situations in the treatment of the hydroxylated surface with NH_4F would take place: 1) The first and most obvious is the reaction between the ammonium cation and the OHT group since OHT is alkaline and inclined to dissociate as an —OH anion. The removal of OHT surface hydroxyl groups relates to their basic nature as well as their readiness to react with the NH_4^+ cation, on the contrary, doubly-bonded OHB removal is more challenging. Thus, removing the OHT hydroxyl groups deletes the trap states which in turn enhances the V_{OC} of PSCs. 2) In the second plausible reaction with the OHT hydroxyl group, a fluorine atom is replaced through anion exchange and terminal fluorine (FT) is formed. As singly-bonded fluorine, FT possesses a lower electron density share of Sn compared to that of doubly-bonded substitutional fluorine. Therefore, FT brings about a higher positive electrostatic potential to bind to the electron and in consequence, OHT trap states are also eliminated once fluoride is exchanged. 3) The third scenario is the replacement of bridge oxygen with fluorine which is of minor effect on the band structure as trap states are not made thereof. 4) In the latter case, in which fluorine is attached to an oxygen bridge, the electronic structure of SnO_2 is remarkably influenced by n-type doping. Fluorine contributes directly to shallow states under the conduction band minimum and the work function of SnO_2 is reduced through NH_4F treatment.[104] Theretofore, Jung et al. could manage to elevate the PCE of PSC from 22.4% and 20.7% to 23.2% and 21.8% making use of NH_4F treatment of SnO_2 layer prepared by CBD method or spin coat of the commercial solution of SnO_2 nanoparticles, respectively.[104]

Glycine representing the $C_2H_5NO_2$ chemical formula has been employed by Du et al.[34] as a buffer layer between SnO_2 and the perovskite layer to control perovskite crystal growth. **Figure 24**a represents the chemical structure of glycine, which consists of the carboxylic acid and the amino group. When deposited on SnO_2, the glycine carboxylic acid group might react with hydroxyl groups on the SnO_2 surface, whereas its outer amine group assists in perovskite formation. Moreover, the presence of glycine would facilitate electron transport at the SnO_2/perovskite interface and obstruct carrier recombination thereof to a great extent (Figure 24b). Figure 24c exhibits the PSC energy level for each layer employed in its architecture. It is also demonstrated that charge carrier extraction and transport could be improved through proper alignment of the energy band at the interface. In this light, glycine treatment could considerably enhance the grain size and quality of the perovskite film as well as the charge extraction/transport at the perovskite/SnO_2 interface. Thereupon, Du et al.[34] managed to increase PSC efficiency from 18.40% to 20.68% using SnO_2 ETL glycine treatment.

Heretofore, tremendous efforts have been devoted to eliminate the defects and make molecular amendments in the ETL/perovskite interface using organic or inorganic interlayers.[166] In comparison with that of inorganic materials, organic materials, principally those of small molecules, present well-defined structural advantages, multifunctional anchoring groups, desirable surface coverage, as well as high reproducibility.[81,167] Sonmezoglu et al.[81] utilized the small organic molecule 2-methylbenzimidazole (MBIm) to modify the perovskite and ETL interface in which, owing to its peculiar structure, it is capable of making interactions with Lewis acid defects in the perovskite through the N atom, whereas the methyl chain is hydrophobic. The extant of these functional groups render supreme characteristics for well-ordered passivation. Furthermore, surface treatment triggers enhancement in the perovskite crystal quality as well as decreasing the density of trap-states in the interface and enabling faster electron transport through energetic disturbance minimization.[81] **Figure 25**a illustrates a schematic of the treatment of SnO_2 layer with small MBIm molecules. MBIm could represent an efficient passivation performance through donating lone electron pairs uncoordinated Pb^{2+} atoms, which operate as electron traps and attenuate

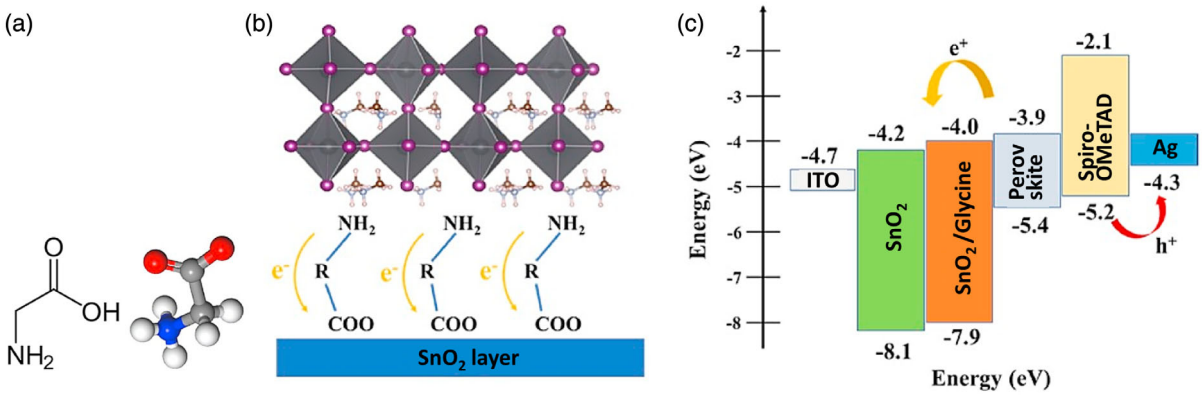

Figure 24. a) Molecular structure of glycine. b) Schematic of SnO_2 ETL where HOCO-R-NH_2 is inserted between the perovskite layer and SnO_2. c) Energy band diagram of the materials utilized in the device. Reproduced with permission.[34] Copyright 2020, Elsevier.

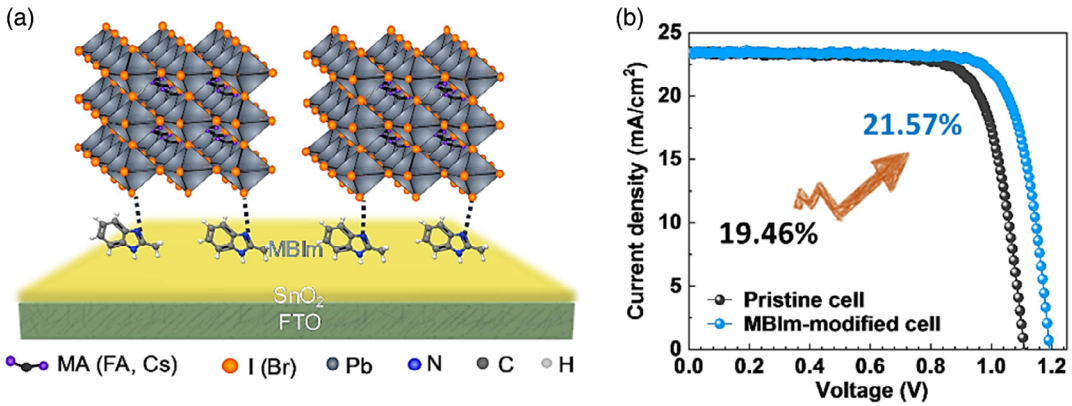

Figure 25. a) Schematic depiction of MBIm anchoring between ETL and perovskite layer. b) *J–V* characteristics of PSCs based upon SnO_2 ETL without and with MBIm treatment. Reproduced with permission.[81] Copyright 2020, Elsevier.

charge transport efficiency. The formation of a coordinate or dative-covalent bond with the beneath surface of the perovskite layer makes the electron valence density to delocalize from the surface in contact with Pb into the bulk. Consequently, this feature improves miscibility with the perovskite layer, which indicates the enhanced perovskite crystallization and a superior passivation effect. This "anchoring effect" associated with MBIm treatment allows the reduction of recombination at the interface and the improvement of V_{OC}. Therefore, Sonmezoglu and coworkers could successfully elevate the PCE of PSCs from 19.46% to 21.57% using the SnO_2 layer treatment with MBIm (Figure 25b).[81]

The presence of surface energy bond bending in SnO_2, due to high oxygen vacancy, causes undesirable accumulation and recombination of electrons in the ETL interface and perovskite layer. Also, the deep-level defects (Pb_I, Pb_i, IP_b) in solution-processed polycrystalline perovskite films intensify the uncoordinated and nonradiative energy band recombination. Sun[168] and colleagues used the amphoteric linking molecule *p*-amino benzenesulfonic acid (ABSA) to modify the interface between SnO_2 ETL and the perovskite layer. Sulfonic acid groups in ABSA, especially the active S–OH group, obtain a stable sulfonate by passivating the undercoordinated Sn ions, which causes the undercoordinated Sn or O ions to become inactive. Pass the SnO_2 film level. In addition, electron-rich alkaline amino groups can passivate the perovskite layer by providing single electron pairs, defect V_I, and deep-level I-Pb antisite defects. The amino may also interact with the iodide ion to stabilize its position. ABSA makes electron loss difficult by passively activating undercoordinated Sn ions. Following the lower electron loss, the modified SnO_2 has a higher N_D and a smaller $eV_{surface}$, which reduces the energy band bending and energy band barrier. Thus, it both reduces recombination at the interface and helps increase conductivity. The team was able to increase the efficiency of LT-SnO_2-based PSCs from 18.02% to 20.32% after using ABSA.

3.2. Multilayer Electron Transporting Layer

A further type of strategy toward the enhancement of PSCs performance based on LT-SnO_2 involves the utilization of multilayer structures for ETL with that of SnO_2. Usually, the application of a single-layer structure does not allow for uniform coverage of the surface, resulting in pinholes and cracks in the layer. These adverse morphological properties would lead to electron recombination with the substrate, poor-quality perovskite layer, current leakage in the cell, and ultimately efficiency loss. Besides, oxygen vacancy (V_O) and Sn interstitials (Sn_i) are conventional defects in the SnO_2 layer due to their ultralow formation energy. It is worth noting that the defects within the layer might affect its electrical and optical properties. Moreover, inherent and bulk defects in the layers might bring about surface recombination, which severely impacts the performance of the PSCs.[86] However then again, one of the most important issues in the efficiency and performance of the PSCs is the energy band alignment at the interface between the ETL/perovskite layer and that of the ETL/electrode. Theretofore, to address these concerns, the utility of a thin layer of organic/inorganic metal oxide compounds alongside that of the SnO_2 layer as an effective approach has been explored by researchers. In this section, we will review the remarkable research works on the application of a multilayer structure (two-layer or sandwich) for ETL alongside SnO_2, in three categories including organic, inorganic oxide, and hybrid compounds atop and/or beneath the SnO_2 layer. Also, a thorough investigation of their working mechanisms and operations in LT-SnO_2-based PSCs will be provided. **Table 3** summarizes the performance and detailed parameters of PSCs built on LT-SnO_2 designated with a multilayer structure. Likewise, **Figure 26** demonstrates LT-SnO_2-based ETLs designed with a multilayer structure.

3.2.1. SnO_2 and Organic Materials

Organic compounds of fullerene and its derivatives extending from C_{60}, phenyl-C_{61}-butyric acid methyl ester (PCBM), and C_9 represent desirable charge extraction as well as the ability to passivate the interfacial defects of the perovskite layer/ETL. A great deal of research studies has been paid on the modification of SnO_2 surface using compounds of fullerenes or graphene to overcome the related issues of this layer and thus improve the performance of the device. Among the most remarkable

Table 3. Performance and characteristics of LT-SnO_2-based PSCs designed with a multilayer structure.

SnO_2 modification				Cell configuration	J_{SC} [mA cm^{-2}]	V_{OC} [V]	FF [%]	Eff [%]	Ref.
ETL multilayer structure	Organic materials	C_{60}	Inverted	FTO/NiO/$MAPbI_3$/C_{60}/SnO_2/Ag	21.80	1.12	77.10	18.80	[51]
			Inverted	ITO/PTAA/$Cs_{0.4}FA_{0.6}PbI_{1.95}Br_{1.05}$/$C_{60}$/$SnO_{1.76}$/Cu	16.50	1.23	78.90	16.00	[37]
			Planar	FTO/SnO_2/C_{60}/$MAPbI_3$/Spiro-MeOTAD/Au	23.70	1.10	77.30	20.20	[169]
			Planar	ITO/SnO_x/C_{60}/$Cs_{0.17}FA_{0.83}Pb(Br_{0.17}I_{0.83})_3$/ Spiro-MeOTAD/Ag	20.3	1.02	61.00	12.60	[170]
			Tandem	ITO/PTAA/$Cs_{0.4}FA_{0.6}PbI_{1.95}Br_{1.05}$/$C_{60}$/$SnO_{1.76}$/ $Cs_{0.05}MA_{0.45}FA_{0.5}Pb_{0.5}Sn_{0.5}I_3$/$C_{60}$/BCP/Cu	15.20	2.03	79.70	24.60	[37]
		C_9	Planar	ITO/SnO_2/C_9/$(FAPbI_3)_x(MAPbBr_3)_{1-x}$/ Spiro-MeOTAD/Au	24.10	1.12	78.90	21.30	[174]
		DPC_{60}	Planar	ITO/SnO_2/DPC_{60}/$FA_{0.81}MA_{0.10}Cs_{0.04}PbI_{2.55}Br_{0.40}$/ Spiro-MeOTAD/Au	22.50	1.11	75.50	18.80	[177]
		PTCDA	Planar	ITO/SnO_2/PTCDA/$MAPbI_3$/PTA/MoO_3/Ag	21.90	0.98	72.00	15.20	[178]
		CPTA	Planar	ITO/SnO_2/CPTA/$MAPbI_3$/Spiro-MeOTAD/Au	22.78	1.09	77.00	19.14	[171]
			Planar	PEN/ITO/SnO_2/CPTA/$MAPbI_3$/Spiro-MeOTAD/Au	22.39	1.08	75.00	18.36	[171]
			Planar	ITO/SnO_2/CPTA/$MAPbI_3$/Spiro-MeOTAD/Au	22.67	1.06	79.50	19.20	[173]
		PCBM	Planar	PEN/ITO/SnO_2/PCBM/$MAPbI_3$/Spiro-MeOTAD/Au	16.19	1.04	66.00	11.13	[171]
			Planar	ITO/SnO_2/PCBM/$Cs_{0.05}(FA_{0.85}MA_{0.15})_{0.95}Pb(I_{0.85}Br_{0.15})_3$/Ag	21.55	1.16	69.40	17.43	[179]
			Planar	ITO/SnO_2/PCBM/$MAPbI_3$/Spiro-MeOTAD/Au	21.91	1.06	77.40	17.90	[173]
			Planar	ITO/SnO_2/PCBM/$Cs_{0.04}FA_{0.92}MA_{0.04}PbI_3$/Spiro-MeOTAD/Au	24.50	1.15	76.65	21.57	[172]
		PCBM:Bphen	Planar	ITO/SnO_2/PCBM:Bphen/$Cs_{0.04}FA_{0.92}MA_{0.04}PbI_3$/ Spiro-MeOTAD/Au	25.15	1.16	78.64	23.09	[172]
		PMMA:PCBM	Planar	ITO/SnO_2/PMMA:PCBM/$Cs_{0.05}(FA_{0.85}MA_{0.15})_{0.95}$ $Pb(I_{0.85}Br_{0.15})_3$/Spiro-MeOTAD/Ag	22.73	1.17	69.87	18.63	[179]
		PMMA:C_{60}	Planar	ITO/SnO_2/PMMA:C_{60}/$MAPbI_3$/Spiro-MeOTAD/Ag	22.64	1.10	76.03	18.99	[175]
			Planar	ITO/SnO_2/PMMA:C_{60}/$Cs_{0.15}FA_{0.85}PbI_3$/Spiro-MeOTAD/Ag	22.98	1.09	78.94	19.82	[175]
			Planar	ITO/SnO_2/PMMA:C_{60}/$Cs_{0.15}FA_{0.75}MA_{0.1}PbI_3$/Spiro-MeOTAD/Ag	23.55	1.15	79.15	21.41	[175]
		PEIE	Planar	ITO/PEIE/SnO_2/$FA_{0.66}MA_{0.27}Cs_{0.035}Rb_{0.035}$ $PbI_{2.73}Br_{0.1}Cl_{0.17}$/PTAA/Au	21.46	0.92	53.26	10.52	[180]
			Planar	ITO/PEIE/SnO_2/$FA_{0.66}MA_{0.27}Cs_{0.035}Rb_{0.035}$ $PbI_{2.73}Br_{0.1}Cl_{0.17}$/PTAA/Au	24.34	1.12	78.64	21.44	
		TPFPB	Planar	ITO/SnO_2/TPFPB/$MAPbI_3$/Spiro-MeOTAD/Ag	23.04	1.07	75.75	18.68	[181]
		I-GQD	Planar	ITO/SnO_2/I-GQD/$FAPbI_3$/Spiro-MeOTAD/PCBM:C_{60}/Ag	25.42	1.07	82.00	22.37	[182]
		FROS	Planar	FTO/SnO_2/IDT-I/$FAMAPb(I,Br,Cl)_3$/Spiro-MeOTAD/Au	24.02	1.05	78.22	19.75	[183]
			Planar	FTO/SnO_2/IDT-T/$FAMAPb(I,Br,Cl)_3$/Spiro-MeOTAD/Au	24.00	1.02	78.91	19.37	
			Planar	FTO/SnO_2/IDDT-T/$FAMAPb(I,Br,Cl)_3$/Spiro-MeOTAD/Au	23.80	1.02	79.44	19.32	
	Oxide inorganic materials	SnO_x	Planar	FTO/SnO_2/SnO_2/$Cs(FAMA)Pb(I,Br)_3$/Spiro-MeOTAD/Au	22.70	1.13	78.00	20.30	[199]
			Planar	ITO/SnO_2/SnO_2/$(FAPbI_3)_{1-x}(MAPbBr_3)_x$/Spiro-MeOTAD/Au	24.63	1.11	77.97	21.28	[207]
			Planar	FTO/SnO_x/SnO_2/$MAPbI_3$/Spiro-MeOTAD/Au	23.20	1.12	71.40	18.60	[200]
			Planar	FTO/SnO_2/SnO_x/$MAPbI_3$/Spiro-MeOTAD/Au	22.39	1.10	70.10	16.90	[200]
			Planar	FTO/SnO_2/SnO_x/$MAPbI_3$/Spiro-MeOTAD/Au	20.92	1.08	72.1	16.29	[201]
			Planar	ITO/SnO_x/SnO_2/$Cs_{0.05}(FAPbI_3)_{0.85}(MAPbBr_3)_{0.15}$/ Spiro-MeOTAD/Ag	23.26	1.13	77.92	20.39	[202]
			Planar	FTO/SnO_2/SnO_x/$Cs_{0.05}(FA_{0.83}MA_{0.17})_{0.95}Pb(I_{0.83}Br_{0.17})_3$/ Spiro-MeOTAD/Ag	18.90	1.04	77.01	15.11	[203]
		SnO_2:$InCl_3$	Planar	ITO/SnO_2:$InCl_3$/$Cs_{0.05}MA_yFA_{0.95-y}PbI_{3-x}Cl_x$/ Spiro-MeOTAD/Ag	23.70	1.07	76.02	20.80	[291]
		SnO_2:NH_4Cl	Planar	ITO/SnO_2:NH_4Cl/SnO_2:NH_4Cl/ $CsFAMAPb(I,Cl,Br)_3$/Spiro-MeOTAD/Au	23.60	1.21	76.20	21.75	[205]
			Planar	ITO/SnO_2/SnO_2:NH_4Cl/$CsFAMAPb(I,Cl,Br)_3$/ Spiro-MeOTAD/Au	24.37	1.10	78.31	21.01	[206]

Table 3. Continued.

SnO_2 modification			Cell configuration	J_{SC} [mA cm^{-2}]	V_{OC} [V]	FF [%]	Eff [%]	Ref.
	TiO_2	Planar	FTO/TiO_2/SnO_2/$CsPbBr_3$/CuPc/C	8.24	1.31	81.40	8.79	[184]
		Planar	FTO/TiO_2/SnO_2/$MAPbI_3$/Spiro-MeOTAD/Au	21.77	1.05	78.79	18.05	[185]
		Planar	FTO/TiO_2/SnO_2/$MAPbI_3$/Spiro-MeOTAD/Au	21.08	1.06	75.10	16.74	[186]
		Planar	ITO/TiO_2/SnO_2/$(FAPbI_3)_x(MAPbBr_3)_{1-x}$/ Spiro-MeOTAD/Ag	22.77	1.15	72.38	19.11	[84]
		Planar	FTO/TiO_2/SnO_2/$MAPbI_3$/Spiro-MeOTAD/Ag	22.52	1.10	76.10	18.85	[187]
		Planar	ITO/SnO_2/TiO_2/$MAPbI_3$/PTAA/Au	21.70	0.98	71.30	15.20	[85]
		Planar	ITO/SnO_2/TiO_2/$(FAPbI_3)_{1-x}(MAPbBr_3)_x$/ Spiro-MeOTAD/Au	24.20	1.10	77.00	20.50	[188]
		Planar	FTO/TiO_2/SnO_2/$FA_{0.9}Cs_{0.07}MA_{0.03}Pb(I_{0.92}Br_{0.08})_3$/ Spiro-MeOTAD/Au	23.87	1.18	79.28	22.33	[190]
	SnO_2:TiO_2	Planar	FTO/TiO_2:SnO_2/SnO_2/$(FAI)_{0.90}(PbI_2)_{0.94}(MABr)_{0.1}$ $(PbBr_2)_{0.1}$/Spiro-MeOTAD/MoO_3/Ag	26.00	1.13	75.00	22.04	[189]
	MgO	Planar	FTO/MgO/SnO_2/$MAPbI_3$/Spiro-MeOTAD/Au	22.39	1.14	74.00	18.82	[191]
		Planar	ITO/MgO/SnO_2/$MAPbI_3$/Spiro-MeOTAD/Au	22.70	1.10	73.00	18.23	[191]
		Planar	ITO/SnO_2/MgO/$MAPbI_3$/Spiro-MeOTAD/Au	22.10	1.13	75.70	19.00	[108]
		Planar	ITO/SnO_2/MgO/$CsPbIBr_2$/Spiro-MeOTAD/Ag	11.07	1.36	69.35	11.04	[192]
	ZnO	Planar	ITO/ZnO/SnO_2/$CsPbI_2Br$/Spiro-MeOTAD/Ag	14.90	1.22	75.30	13.70	[195]
		Planar	ITO/SnO_2/ZnO/$CsPbI_2Br$/Spiro-MeOTAD/MoO_3/Ag	15.00	1.23	78.80	14.30	[193]
		Planar	ITO/SnO_2/ZnO/$MAPbI_3$/Spiro-MeOTAD/Au	22.10	1.20	77.00	20.43	[194]
	In_2O_3	Planar	ITO/In_2O_3/SnO_2/$(FA,MA)Pb(I_x,Cl_{1-x})_3$/ Spiro-MeOTAD/Au	24.45	1.17	81.09	23.24	[196]
	Al_2O_3	Planar	ITO/SnO_2/Al_2O_3/$MAPbI_3$/Spiro-MeOTAD/Au	23.20	1.14	75.70	20.10	[107]
	ZrO_2	Planar	ITO/ZrO_2/SnO_2/$MAPbI_{3-x}Cl_x$/Spiro-MeOTAD/Ag	23.32	1.07	78.20	19.48	[198]
	WO_x	Planar	ITO/WO_x/SnO_2/$MAPbI_3$/Spiro-MeOTAD/Ag	23.01	1.11	80.34	20.52	[197]
	MAI-capped rare earth-doped WO_x nanorods	Planar	FTO/SnO_2/MAI-capped La:WO_x nanorods/ $CsFAMAPb(I,Br)_3$/Spiro-MeOTAD/Au	23.87	1.14	78.71	21.42	[208]
		Planar	FTO/SnO_2/MAI-capped Sm:WO_x nanorods/ $CsFAMAPb(I,Br)_3$/Spiro-MeOTAD/Au	23.80	1.14	78.65	21.34	
		Planar	FTO/SnO_2/MAI-capped Eu:WO_x nanorods/ $CsFAMAPb(I,Br)_3$/Spiro-MeOTAD/Au	23.75	1.14	78.63	21.29	
		Planar	FTO/SnO_2/MAI-capped Dy:WO_x nanorods/ $CsFAMAPb(I,Br)_3$/Spiro-MeOTAD/Au	23.68	1.14	78.20	21.11	
		Planar	FTO/SnO_2/MAI-capped Er:WO_x nanorods/ $CsFAMAPb(I,Br)_3$/Spiro-MeOTAD/Au	23.64	1.13	77.79	20.78	
		Planar	FTO/SnO_2/MAI-capped Yb:WO_x nanorods/ $CsFAMAPb(I,Br)_3$/Spiro-MeOTAD/Au	23.55	1.13	77.37	20.59	
	Rb halides	Planar	ITO/SnO_2/RbF/$CsFAMAPb(I,Br,Cl)_3$/Spiro-MeOTAD/Au	24.32	1.21	79.29	23.38	[209]
		Planar	ITO/SnO_2/RbCl/$CsFAMAPb(I,Br,Cl)_3$/Spiro-MeOTAD/Au	22.60	1.16	77.16	20.32	
		Planar	ITO/SnO_2/RbI/$CsFAMAPb(I,Br,Cl)_3$/Spiro-MeOTAD/Au	22.57	1.15	77.99	20.37	
	B_2Cat_2	Planar	ITO/SnO_2/B_2Cat_2/$CsFAMAPb(I,Br,Cl)_3$/Spiro-MeOTAD	23.70	1.148	80.98	22.04	[210]
	Bi_2O_2Se	Planar	ITO/SnO_2/Bi_2O_2Se/$MAPbI_3$/Spiro-MeOTAD/MoO_x/Ag	23.48	1.07	75.85	19.06	[211]
	$Ti_3C_2T_x$ MXene	Planar	FTO/$Ti_3C_2T_x$ MXene/SnO_2/ $Cs_{0.05}FA_{0.76}MA_{0.19}PbI_{2.715}Br_{0.285}$/ Spiro-MeOTAD/Au	24.34	1.11	74.00	20.65	[214]
	$Al(acac)_3$	Planar	PET/ITO/SnO_2/$Al(acac)_3$/ $FAMAPb(I,Cl)_3$/Spiro-MeOTAD/MoO_x/Au	24.69	1.13	74.63	20.87	[215]
Organic/inorganic materials	C QDs/SnO_2	Planar	ITO/SnO_2/C QDs/SnO_2/ $MAPbI_3$/Spiro-MeOTAD/Ag	23.52	1.13	78.20	20.78	[216]
	SnO_2/ PMMA:PCBM	Planar	FTO/SnO_2/SnO_2/PMMA:PCBM/ $(FA_{0.83}MA_{0.17})_{0.95}Cs_{0.05}PbI_{2.5}Br_{0.5}$/Spiro-OMeTAD/Au	23.60	1.18	70.00	19.50	[217]

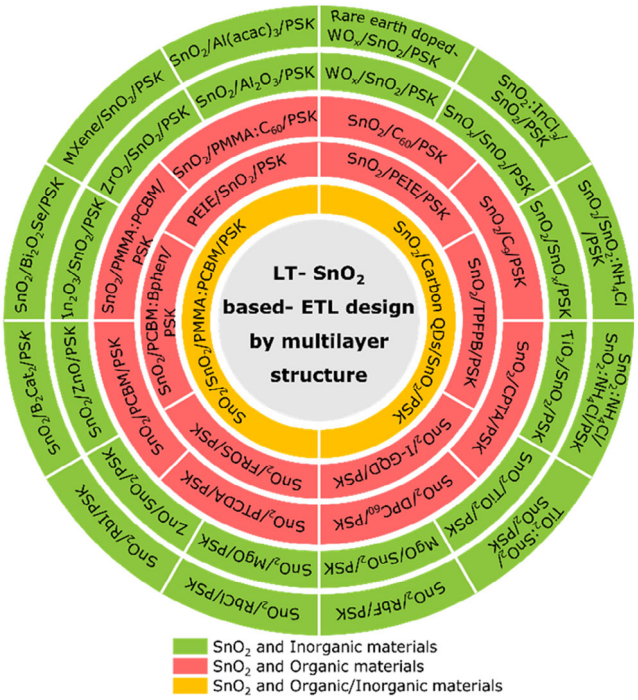

Figure 26. LT-SnO_2-based ETLs designated with a multilayer structure.

advantages of utilizing organic compounds between the perovskite layer and SnO_2 ETL is the coupling in the perovskite/organic layer interface as well as passivation in both the perovskite/organic layer and organic/SnO_2 layer interface. The use of organic compounds increases the extraction and transport of electrons from the perovskite absorbing layer into the electrode by passivating the SnO_2 film surface and optimizing the E_{CB}, which makes for reducing the recombination at the perovskite/ETL interface as well as significant hysteresis abatement.

Zhu et al.[51] could enhance electron extraction by inserting the C_{60} layer between that of the perovskite and the SnO_2 layer in the inverted structure PSC. They prepared the SnO_2 layer through sol–gel and hydrothermal methods and observed that the performance of the layer prepared by the latter was superior. In respect of both the E_{CB}s of the SnO_2 and C_{60}, 4.5 and 3.9 eV, respectively, and the E_{CB} difference between those of the SnO_2 and the perovskite (about 0.6 eV), which might lead to undesirable charge accumulation at the interface, the presence of C_{60} in between could be profitable. What is more, the remarkable effect of the C_{60} layer made for a perfect hysteresis elimination and subsequent PCE enhancement from 15.05% to 18.82%. Furthermore, Mahmood et al.[169] realized that SnO_2 nanosheets prepared through the electrospray technique demonstrated higher performance than that of the hydrothermal method in a planar PSC structure. The SnO_2 nanosheets synthesized by high electrospray possessing high mesoporosity resulted in reduced hysteresis, increased charge collection efficiency, and improved environmental stability. Therein, intending to optimize the interface between SnO_2 and perovskite layer, they employed a C_{60} layer to alleviate the recombination and enhance the band energy alignment. Therefore, utilizing the C_{60} interlayer, they could increase the efficiency of planar PSCs based on electrospray-prepared SnO_2 ETL from 15.69% to 20.20%. Zhao et al.[170] used a low-temperature, open-air plasma process for deposition of SnO_x thin films. They optimized the deposition conditions and parameters and fabricated a SnO_x thin film on substrates up to 100 cm^2 without any post-annealing. Also, Zhong et al.[171] applied a fullerene derivative with a carboxylic group (C_{60} pyrrolidine tris-acid, CPTA) between the SnO_2 ETL and perovskite interface. The presence of CPTA as an interface modification agent increased conductivity and electron transport and, consequently, the efficiency of PSC on rigid glass/ITO and flexible PEN/ITO substrates elevated from 16.91% to 19.14% and from 15.35% to 18.36%, respectively. Moreover, the result of this work involved the comparison between that of CPTA and PBCM as organic compounds in which the former demonstrated higher performance. Hang et al.[172] modified PCBM ester by a small amount of the bathophenanthroline (Bphen), which could stabilized the C_{60}-cage via the formation of much more thermodynamically stable charge-transfer complexes against the stress of natural light. Huang et al.[173] compared CPTA and 6,6-phenyl C_{61}-butyric acid methyl ester ($PC_{61}BM$)-modified SnO_2 as bilayer ETLs in PSCs. CPTA and $PC_{61}BM$ have a favorable energy band edge alignment to perovskites, so enhanced electron injection rate. They reported that the interfacial tailored chemical bond between the SnO_2 surface and carboxylic acids of CPTA leads to interface dipoles. Due to the presence of interface dipoles, the chemisorption of CPTA fullerene functions acts as a recombination suppressor in both the SnO_2/perovskite interface and perovskite. In contrast, the physisorption of $PC_{61}BM$ fullerene exhibits relatively high recombination rates both in the SnO_2/perovskite interface and within the perovskite. Likewise, Liu and coworkers[174] utilized a fullerene-derived compound, i.e., C_9 as the passive layer between the perovskite layer and the SnO_2 layer. The consequent effective passivation of oxygen vacancy defects on the SnO_2 surface resulting from this compound inhibited charge recombination by forming a Lewis adduct between Sn and that of the C_9 lateral hydroxyl groups. Besides, surface modification with C_9 increases the current thoroughly owing to the negligible barrier against charge extraction and strong electron demand. In a similar manner, the utilization of C_9 in addition to surface passivation improved the quality of the perovskite film through the grain size enlargement as well as diminishing the grain boundaries and the crystallinity enhancement. Also, Chen et al.[175] used PMMA:C_{60} composite as an interlayer between perovskite and SnO_2 layer and could realize PCEs of 18.99%, 19.82%, and 21.41%, through reducing trap sites in PSCs based on different absorbents of $MAPbI_3$, $CsFAPbI_3$, and $CsFAMAPbI_3$, respectively. They made use of PTABr to modify perovskite to increase grain size and diminish grain boundaries in the absorbent layers.

Delgado et al.[176] utilized C_{60} interlayers deposited through solution processing and vacuum-based thermal evaporation methods at the interface between SnO_2 and the perovskite ($MAPbI_{3-x}Cl_x$) layer and optimized the thickness of this layer. In the optimized conditions, C_{60} passivated the trap states at the SnO_2/perovskite interface reducing the charge carrier accumulation at the ETL/Perovskite interface, enhancing the charge extraction, facilitating the charge transport, as well as increasing the fill factor. Eventually, the reported champion efficiency of

PSC therein was 18.9% with 10 nm C_{60} thickness. Tian and coworkers[177] have also employed yet another derivative of fullerene, i.e., amine-functionalized group, 2,5-diphenyl C_{60} fulleropyrrolidine (DPC_{60}) for passivating the interfacial defects between perovskite and SnO_2 ETL. Furthermore, the hydrophobicity of the DPC_{60} layer suppressed heterogeneous nucleation and boosted the crystallinity of the perovskite film and the stability of the cells. Tsarev et al.[178] deposited an optimized thickness of a low-cost organic *n*-type semiconductor, perylenetetracarboxylic dianhydride (PTCDA), via thermal evaporation as an interlayer between perovskite/SnO_2 for planar PSCs. Hu and coworkers[179] have presented a passivating agent for the limitation of the interfacial carrier recombination and hysteresis employing an ultrathin composite layer of PMMA: PCBM. Besides the inverted and planar structured PSCs, Yu et al.[37] have employed C_{60} as an interlayer between the perovskite and the SnO_2 layer in the all-perovskite tandem structure. C_{60} interlayer acts as an effective electron collecting layer along with a SnO_{2-x} ($0 < x < 1$) layer rendering an ambipolar carrier transport property for the presence of a large density of Sn^{2+} which this approach induces ohmic contacts with both wide and narrow bandgap perovskites as well as low contact resistivity. Moreover, the fullerene layer avoids the formation of a reverse-biased diode between the two subcells, which would enhance the PCEs of small-area tandem cells (5.9 mm^2) and large-area tandem cells (1.15 cm^2) to 24.4% and 22.2%, respectively, representing high light stability.

He's group[180] used polyethylenimine ethoxylated (PEIE) in the SnO_2 ETL structure as composite (SnO_2:PEIE) and bilayers (PEIE/SnO_2 and SnO_2/PEIE) structures, that PEIE is a polyelectrolyte containing simple aliphatic amine groups. By comparing these three ETL structures, they found that the presence of PEIE layer under SnO_2 layer has the best performance. As the underneath PEIE layer, by adjusting the surface energy and work function of the top SnO_2 layer, improved the nucleation process of perovskite layer and reduced the energy-level mismatch between ETL and perovskite layer. Accordingly, they succeeded to achieve PCE of 21.44% using PEIE/SnO_2 bilayer ETL compared to pure SnO_2 (18.42%), SnO_2/PEIE bilayer (10.52%), and SnO_2:PEIE composite (19.06%) ETLs. Li et al.[181] by adding tris(pentafluorophenyl) boron (TPFPB) as interfacial modification layer between SnO_2 ETL and perovskite layer formed a compact perovskite layer and decreased defects on SnO_2 film. They reported that the presence of the interfacial TPFPB layer improves the interface performance and enhances the crystallinity of $MAPbI_3$, and thus the fabricated device with TPFPB modification shown fast charge transfer and low trap state density. By optimizing the amount of TPFPB, they enhanced PCE from 16.92% to 19.41%, which resulted from the weak chemical bonds between TPFPB and the top and underneath layers, i.e., the F and B atoms in TPFPB forming H–F, N–B bonds with SnO_2 and perovskite ($MAPbI_3$), respectively. Gao et al.[182] demonstrated to regulate the interface ETL/perovskite by imidazole bromide functionalized graphene quantum dots (I-GQDs). Their results showed the incorporation of the functional groups on the surface of I-GQDs at the interface can improve the conductivity and eliminate surface defects of SnO_2 ETL to achieve a better E_{CB} alignment between SnO_2/perovskite. The presence of I-GQD interlayer enhanced the interfacial charge carrier transfer and inhibited the interface charge recombination. Gao group[183] modified the SnO_2-based ETL in PSCs by insertion of fused-ring organic semiconductors (FROSs) layer on the SnO_2 layer. They used three types of FROSs (IDT-I, IDT-T, and IDDT-T), which include indacenodithiophene (IDT) or indacenodithienothiophene (IDDT) as the bridging donor moiety and 1,3-diethyl-2-thiobarbituric or 1,1-dicyromethylene-3-indanone as the strong electron-withdrawing units. IDT-T and IDT-I include one IDT backbone with two 1,3-diethyl-2-thiobarbituric and two 1,1-dicyromethylene-3-indanone electron-withdrawing end groups, respectively. In comparison, IDDT-T include an IDDT ore with two 1,3-diethyl-2-thiobarbituric terminal groups. The interface decorated by FROSs enhances the charge extraction and transportation at the interface between ETL/perovskite layer.

3.2.2. SnO_2 and Inorganic Materials

In addition to organic compounds, inorganic materials along with SnO_2 have been utilized as ETL in PSCs, which could better the morphological properties, tune the band alignment, and enhance the V_{OC} in PSCs.[184,185] Case in point, the application of TiO_2 in combination with SnO_2 as ETL promotes more perfect segregation of photogenerated carriers and electron transport due to the increased charge extraction ability and the hindrance of carrier recombination in the ETL/perovskite interface. Liu et al.[184] utilized SnO_2 to passivate TiO_2 surface aimed at the fabrication of PSCs based on carbon electrode with the $CsPbBr_3$ perovskite material. By inserting a SnO_2 layer between the TiO_2 layer and that of the perovskite, they could elevate the efficiency from 8.12% to 8.79%. Furthermore, they could successfully achieve a PCE of 6.9% for the module based on TiO_2/SnO_2 bilayer ETL with an active area of 1 cm^2. Correspondingly, Deng et al.[186] could realize the PCE of 15.14% utilizing the TiO_2/SnO_2 bilayer layer as ETL in the planar structured PSC. Besides, they could manage to increase the efficiency to 16.74% through the modification of TiO_2 with HI and by the optimization of the conditions, a further PCE enhancement of up to 18.05% was achieved.[185] Li et al.[84] employed TiO_2, SnO_2, and TiO_2/SnO_2 bilayer as ETL in planar structured PSCs and obtained PCEs of 14.53%, 17.21%, and 19.11%, respectively. In like manner, Xie et al.[187] could achieve the PCEs of 13.15%, 16.7%, and 18.85%, respectively, wherein TiO_2, SnO_2, and TiO_2/SnO_2 bilayer was employed as ETL in the planar PSCs.

The utilization of TiO_2 is not merely limited to beneath the SnO_2 layer as the TiO_2/SnO_2 bilayer ETL, and its utility above the SnO_2 as the structure of SnO_2/TiO_2 bilayer ETL has also been reported. Martinez-Denegri et al.[85] achieved efficiencies of 14.2%, 8.6%, and 14.9%, respectively, using TiO_2, SnO_2, and SnO_2/TiO_2 bilayer as ETL in planar structured PSC. Hu et al.[188] made use of SnO_2/TiO_2 and improved the PCE from 18.09% to 20.50% in light of cascade-aligned energy levels of ITO/SnO_2/TiO_2/perovskite, multicomponent for the charge transporting layers including ETLs and HTLs and the reduced defects in the perovskite film. Wu's group[189] designed five LT-processed ETLs (SnO_2, TiO_2, TiO_2:SnO_2 composite, TiO_2/SnO_2 bilayer, and TiO_2:SnO_2/SnO_2 bilayer) and found TiO_2:SnO_2/SnO_2 bilayer is optimized ETL structure with PCE of 22.04%. In this optimized design, there was TiO_2:SnO_2 layer

as the bottom layer that contained the small TiO_2 and highly conducting big SnO_2 nanoparticles for making a dense film to avoid the short circuit, and increasing the conductivity of ETL, adjusting the CB level for reducing the charge accumulation and series resistance of the cell, respectively. A top SnO_2 layer was used to facility electron transport and to create a hydrophilic surface for deposition of high-quality perovskite films. The TiO_2:SnO_2 nanoparticle suspension used for fabricating a TiO_2:SnO_2 nanocomposite was prepared by ball grinding of the TiO_2 and SnO_2 powder mixture in ethanol at room temperature without adding any surfactant and the top SnO_2 layer was spin-coated from Alfa-SnO_2 nanoparticle water suspension. Rao et al.[190] used TiO_2 compact layer between FTO substrate and SnO_2 layer, and they improved the PCE by reducing the trap-assisted recombination with the incorporation of KI and $KC_6H_5BF_3$, respectively, into perovskite film.

In addition to TiO_2, MgO has also been recognized as a promising candidate to use as ETL along with SnO_2. Ma et al.[191] by adding a thin layer of MgO between the substrate and SnO_2, could substantially increase the PSC efficiency from 16.43% to 18.23%. Likewise, Dagar et al.[108] were able to increase PSC performance by employing a thin layer of MgO to the SnO_2 layer, therein making use of MgO, SnO_2, SnO_2/MgO bilayer, and SnO_2/SnO_2 bilayer as ETLs in planar PSCs. Also Wang et al.[192] used MgO layer between the SnO_2 and perovskite ($CsPbIBr_2$) to passivate the undesirable recombination and thereby V_{oc} increases. The top MgO layer provided a better qualify perovskite formation and reduced the interface vacancy defects and also its tunneling effect and better band alignment with perovskite effectively blocked the hole carriers and accelerated the electron carriers to the electrode. Yan and coworkers[193] realized the highest V_{oc}e of 1.23 V for PSCs based upon SnO_2/ZnO bilayer using a ZnO layer of optimized thickness on the SnO_2 layer. The presence of the ZnO layer possessing a conduction band position between SnO_2 and the perovskite layer makes improvements in the extraction and transport of carriers and reduces recombination as well. Therefore, utilizing ZnO, SnO_2, and SnO_2/ZnO bilayer as ETL in planar PSCs. To diminish the energy loss in $MAPbI_3$-based planar PSCs, Noh et al.[194] proposed the utilization of SnO_2/ZnO bilayer ETL owing to its befitting energy band matching at the interface of $MAPbI_3$. Besides, thermal annealing lowered the Fermi level of the bottom ZnO (not-annealed) layer in the bilayer ETL and enhanced the superior film quality, suppressed the trap density, and reduced the charge recombination at the interface of ETL/perovskite making for PCE increment up to 20.43%. Yang et al.,[195] as to the lower work function of ZnO compared to that of SnO_2 curtailing the energy losses, have employed ZnO/SnO_2 bilayer as ETL. With this bilayer ETL, a high iodine content $CsPbI_2Br$ film was formed on which a regular crystal grain, as well as full coating coverage and a more perfect crystal matching between perovskite and SnO_2, was realized.

Since the conduction band of In_2O_3 is higher than that of Sn-doped In_2O_3 (ITO), Wang[196] has utilized In_2O_3/SnO_2 bilayer ETL and enhanced the charge transport from perovskite to the ETL. Whereas SnO_2 layers yielded 21.42% efficiency, and the obtained ETL represented high uniformity, compactness, as well as low-trap-density and elevated the PCE further to 23.24%. Dagar et al.[107] also applied an Al_2O_3 layer on the SnO_2 layer as the ETL bilayer in the planar PSCs. Nevertheless, Al_2O_3 had previously been employed as a scaffold, a thin layer of 50 nm particles was deposited therein. The effect of this layer on the shunt and series resistance (R_{sh} and R_s) and series as well as charge extraction facilitation made for enhanced efficiency. Therefore, they could realize the PCE elevation from 15.3% in PSCs based on SnO_2 ETL to 20.1% in that of PSCs based on SnO_2/Al_2O_3 bilayer ETL. Furthermore, another method of the hole blocking as well as preventing the recombination on defective surface coverage is by far the utilization of a WO_x layer between the electrode and SnO_2. By applying this, Wang et al.[197] managed to increase the PCE of SnO_2 ETL-based PSCs from 17.67% to 20.44%. Sun and coworkers[198] modified ITO using a ZrO_2 interlayer between ITO and SnO_2 prepared through ultraviolet (UV) treatment at room temperature. The effects of the interlayer on the performance of $MAPbI_{3-x}Cl_x$-based PSCs could reach to champion efficiency of 19.48% with negligible $J-V$ hysteresis (more than reference 15.56%). The improved performance has resulted from the reduced trap states, the promoted charge extraction at the ITO/SnO_2 interface, and the suppressed carrier recombination at the ITO/SnO_2 interface.

Lin et al.[199] utilized SnO_2/SnO_2 bilayer ETL to diminish the hysteresis of PSCs based on LT-SnO_2 ETL in which the lower SnO_2 layer was prepared through spin-coating of chloride precursor and that of the upper layer was prepared through the spin-coating of colloidal nanoparticle ink. Zhang et al[200] introduced an ultrathin and compact SnO_x amorphous layer derived from $SnCl_4$ at the interface of SnO_2/perovskite or FTO/SnO_2 to form SnO_2/SnO_x bilayer ETL or SnO_x/SnO_2 bilayer ETL, respectively, to enhance the electron coupling between layers, passivate the trapping defects, and optimize the energy-level alignment. As a result of the increased interface electron collection and reduced interface recombination, the planar PSC with pretreated SnO_2 nanocrystal ETL exhibited boosted efficiency from 16.3% to 18.6%. Besides, posttreated SnO_2 nanocrystal ETL made the efficiency increment from 16.3% to 17.3% which these results indicate that both treatment methods could improve the performance of the PSCs to great effect. Likewise, Sun et al.[201] could manage to fabricate a PSC based on SnO_2/SnO_x bilayer ETL by inserting an amorphous SnO_x layer via a tin chloride precursor ink spin-coated on the SnO_2 nanocrystalline layer. Also Kang's group[202] used SnO_x/SnO_2 bilayer ETL for ohmic contact improvement and recombination decreasing in the ETL/perovskite interface to achieve the PCE of ≈20.39% for lab scale and ≈14.93% for large-area PSCs (active areas of ≈3.55 cm^2). Moreover Choopun's group[203] used SnO_2/SnO_x bilayer ETL and compared with SnO_2 ETL in PSCs. Guo et al.[204] used the SnO_2:$InCl_3$ as a top layer on SnO_2, because the Cl ions can well passivate the SnO_2 surface defects and perovskite grain boundaries by Cl ions diffusion into the perovskite layer and Pb–Cl bonds formation with Pb ions in the perovskite, furthermore, In can improve the SnO_2 electron mobility. Hereupon, the PCE increased because of the lower interfacial trap density, larger perovskite grain size, and higher ETL electron mobility. Ye et al.[205] fabricated several types of SnO_2-based ETLs by pure, low-, and high-amount NH_4Cl-doped SnO_2 (L-NH_4Cl:SnO_2 and H-NH_4Cl:SnO_2). Based on their results, they found the best performance for L-NH_4Cl:SnO_2/H-NH_4Cl:SnO_2 bilayer as an ETL. Also Song et al.[206] designed and used a SnO_2/NH_4Cl:

SnO_2 bilayer as an ETL in PSC structure. They reported the top layer showed a better energy-level alignment with perovskite and reduced the alkalinity of ETL/perovskite interface to avoid perovskite degradation and hereupon enhanced electron extraction and interfacial stability. Also the underneath SnO_2 retained the capability of efficient carrier transport to avoid charge accumulation.

Shi et al.[207] obtained the optimized PCE of 21.28% in the PSC through the application of a two-step deposition of SnO_2 following UV-assisted thermal annealing for SnO_2/SnO_2 bilayer ETL. Thereafter, they could also manage to passivate oxygen vacancy defects through the deposition of the small multifunctional molecule pentetic acid (i.e., DTPA) on the surface of the ETL bilayer and the consequent formation of a chemical reaction and bonding between the DTPA carboxylic groups and the undercoordinated Sn on the surface of the SnO_2 bilayer ETL. What is more, the presence of hydrophilic DTPA on the ETL surface allowed the homogeneous perovskite nucleation via reducing Gibbs-free energy in the DTPA-SnO_2 complex. Furthermore, the formation of coordination of DTPA carboxylic groups with undercoordinated Pb ions made for the passivation of perovskite.

Chen et al.[208] used the Lanthanide ions (La^{3+},Sm^{3+}, Eu^{3+}, Dy^{3+}, Er^{3+}, Yb^{3+}) doped WO_x nanorods were prepared by the hot solvent method for perovskite crystal quality improving and charge recombination hindering by interface traps/defects reducing between the ETL and perovskite. As their result, the La:WO_x/SnO_2 bilayer ETL showed the best PCE of 21.42% with high stability in compared to SnO_2-based devices (19.08%). Zhuang et al.[209] used rubidium halides (RbF, RbCl, and RbI) as the top layer of SnO_2 to form SnO_2-based bilayer ETLs, based on their efficiency (21.12%, 20.37%, and 20.32%), RbF showed the best performance. They also used RbF to prepare the SnO_2:RbF composite ETL and compared its performance with the SnO_2/RbF bilayer ETL. According to their achievements, in SnO_2:RbF composite ETL, F and Sn have strong interaction and contributing to the improved electron mobility of SnO_2 and charge transport, and in SnO_2/RbF bilayer ETL, Rb^+ cations actively escape into the interstitial sites of the perovskite lattice to inhibit ions migration and reduce nonradiative recombination, which dedicates to the improved V_{oc}. Also, they noted that F^- stays in place and does not enter the perovskite. Finally, they were able to increase the PCE to 23.38% by modifying the perovskite via *p*-methoxyphenethylammonium iodide (CH_3O-PEAI).

Zhou's group[210] has reported using the diboron (B_2Cat_2) molecule as the interfacial modifier between SnO_2 and perovskite. Based on the SnO_2/B_2Cat_2 bilayer ETL, they obtained a higher E_F on the surface of SnO_2, resulting from a better energy matching at ETL/perovskite interface and a higher PCE of 22.04%. They showed SnO_2/B_2Cat_2 bilayer possesses some Sn^{3+} species, acting as electron donors to obtain a more n-type nature of ETLs. And speculate that the formation of surface diboron–oxygen Lewis pair induces a reducing state of diboron complexes, which further enables spontaneous electron redistribution for the formation of Sn^{3+}–$O^{-\bullet}$species on the surface of SnO_2Chen et al.[211] introduced two-dimensional Bi_2O_2Se nanoflakes to modify the surface of SnO_2 thin film with high charge mobility. They synthesized Bi_2O_2Se nanoflakes by facile composited molten salt method. SnO_2/Bi_2O_2Se bilayer ETL provides a smoother and more hydrophobic surface for larger perovskite crystal formation. The PCE of PSCs based on SnO_2/Bi_2O_2Se bilayer ETL compared with PSCs based on SnO_2 ETL was improved to 19.06% from 16.29%.

MXenes are 2D mineral sheets of transition metal carbides and nitrides, which have been highly interested owing to their metal conductivity, low electrical resistance, high hydrophilicity, and structural diversity.[212] The general formula of MXenes is $M_{n+1}X_nT_x$, in which M represents an early transition metal, X is carbon and/or nitrogen, $n = 1$–3, and T_x stands for the termination functional groups (O, OH, and/or F).[91,212,213] Highly transparent $Ti_3C_2T_x$ MXene with high electron mobility also possesses excellent metallic conductivity and superior thermal stability.[214] Due to the rich functionalized surface groups of $Ti_3C_2T_x$ MXene, the work function of $Ti_3C_2T_x$ MXene ranges from 1.6 to 6.25 eV.[214] Wang et al.[214] modified surface between FTO and SnO_2 by inserting a thin layer of $Ti_3C_2T_x$ MXene, which led to well energy-level alignment, enhanced electron mobility, and efficient charge transfer dynamics. MXene/SnO_2 bilayer ETL led to a significantly reduced nonradiative recombination and enhanced charge extraction. In addition, surface of MXene/SnO_2 bilayer ETL has a more hydrophobic and smoother morphology, beneficial for the growth of a perovskite film with low trap density which achieved an enhanced efficiency of 20.65%. Zhang group[215] by using aluminum acetylacetonate ($Al(acac)_3$) as a cross-linking agent, which is used for interface layer between SnO_2 and perovskite could achieve high reported PCE (20.87%) for flexible PSCs up to now. It was due to the well-matched energy levels and improved grain size and crystallinity of the perovskite and also $Al(acac)_3$ is similar to the spiderweb which can act as an effective barrier. Based on their achievements, the oxygen moiety of the carbonyl group of $Al(acac)_3$ can interact with Pb atoms of perovskite and forming a Lewis adduct to passivate defects at the grain surface. Also, adhesive interaction of the $Al(acac)_3$ can produce a compact and protective structure to resist water infiltration and mechanical bending, improving the overall stability of flexible PSCs and enhancing bending resistance. So that attributed to the $Al(acac)_3$ super bending resistance, more than 91% of the original PCE.

3.2.3. SnO_2 and Organic/Inorganic Materials

He et al.[216] designed a sandwich-like architecture using an ultrathin bandgap tunable carbon quantum dots (CQDs) layer inserted between ultrathin SnO_2 bottom layer and SnO_2 top layer like SnO_2/CQDs/SnO_2. The bottom ultrathin SnO_2 layer passivates the defects of FTO and reduces the carrier recombination, while the CQDs layer enhances the optical transmission of ETLs, accelerates the carrier transport process, and improves the hole-blocking ability, resulting in the PCE of 20.78% (boosted from 17.46%) which is hysteresis free. Prasad'S and Ng's groups[217] introduced an optimal amount of organic cross-linker, 2,20—(ethylenedioxy)bis (ethylammonium iodide) (EDAI) for defect passivation in the bulk of mixed cation perovskite and ETL consisted of SnO_2 quantum dots (SnO_2 QD) or SnO_2 nanoparticles (SnO_2 NP). By this approach due to the generation of defects and electrically insulating properties of EDAI, the hysteresis is reduced, efficiency enhanced, and stability improved. Therein, they employed a SnO_2 QD/SnO_2 NP/PMMA: PCBM

Table 4. Performance and featured characteristics of PSCs based on LT-SnO_2 ETL modified via elemental doping.

SnO_2 modification				Cell configuration	J_{SC} [mA cm^{-2}]	V_{OC} [V]	FF [%]	Eff [%]	Ref.
Elemental Doping	Electrical properties	Sb	Planar	ITO/Sb:SnO_2/$MAPbI_3$/Spiro-MeOTAD/Au	22.60	1.06	72.00	17.70	[229]
		Nb	Planar	FTO/Nb:SnO_2/$(FAPbI_3)_{0.85}(MAPbBr_3)_{0.15}$/Spiro-MeOTAD/Au	22.72	1.18	73.00	19.38	[221]
		Al	Planar	FTO/Al:SnO_2/$MAPbI_3$/Spiro-MeOTAD/Au	19.40	1.03	58.00	12.10	[222]
		Li	Planar	FTO/Li:SnO_2/$MAPbI_3$/Spiro-MeOTAD/Au	23.27	1.11	70.71	18.20	[27]
			Planar	ITO/Li:SnO_2/$MAPbI_3$/Spiro-MeOTAD/Au	22.28	1.07	76.11	18.35	[292]
		Mo	Planar	FTO/Mo:SnO_2/$MAPbI_3$/Spiro-MeOTAD/Au	15.20	0.97	71.10	10.52	[230]
		Zn	Planar	FTO/Zn:SnO_2/$Cs_{0.05}FA_{0.79}MA_{0.16}PbI_{2.5}Br_{0.5}$/CuPc/C	23.40	1.10	69.20	17.78	[40]
		Y	Planar	FTO/Y:SnO_2/$Cs_{0.05}(MA_{0.15}FA_{0.85})_{0.95}Pb(I_{0.85}Br_{0.15})_3$/Spiro-MeOTAD/Au	23.56	1.13	77.78	20.71	[293]
	Structure properties	Ga	Planar	ITO/Ga:SnO_2/$(FAPbI_3)_x(MAPbBr_3)_{1-x}$/Spiro-MeOTAD/Ag	23.90	1.07	71.40	18.18	[223]
		Gd	Planar	ITO/Gd:SnO_2/$MaFAPb(I,Br,Cl)_3$/Spiro-MeOTAD/Au	23.80	1.14	82.00	22.40	[225]
		Eu	Planar	FTO/Eu:SnO_2/$MAPbI_3$/Spiro-MeOTAD/Au	22.61	1.13	78.76	20.14	[235]
		Zn	Planar	FTO/Zn:SnO_2/$MAPbI_3$/Spiro-MeOTAD/Au	23.39	1.11	77.30	20.16	[76]
		Ta	Planar	ITO/Ta:SnO_2/$Cs_{0.05}(MA_{0.15}FA_{0.85})_{0.95}Pb(I_{0.85}Br_{0.15})_3$/Spiro-MeOTAD/Au	22.79	1.16	78.60	20.80	[294]
				FTO/Ta:SnO_2/$MAPbI_3$/Spiro-MeOTAD/MoO_3/Ag	22.56	1.08	75.00	18.23	[224]
		Li	Planar	ITO/Li:SnO_2/$MAPbI_3$/Spiro-MeOTAD/Au	22.20	1.08	69.20	19.09	[233]
			Planar	FTO/Li:SnO_2/$MAPbI_3$/C	19.91	0.77	59.00	9.13	[218]
			Mesoporous	FTO/Li:SnO_2/Al_2O_3 + $MAPbI_3$/C	22.18	0.76	59.00	10.01	[218]
		Nd	Planar	FTO/Nd:SnO_2/$Cs_{0.05}(MA_{0.17}FA_{0.83})_{0.95}Pb(I_{0.83}Br_{0.17})_3$/PCBM/Au	23.85	1.22	78.20	20.92	[234]
		Zr	Planar	FTO/SnO_2/$MAPbI_3$/Spiro-MeOTAD/Au	23.50	1.08	72.00	19.54	[231]
		F	Planar	FTO/F:SnO_2/$(FAPbI_3)_{0.85}(MAPbBr_3)_{0.15}$/Spiro-MeOTAD/Au	22.92	1.13	78.05	20.20	[227]
		Cl	Planar	FTO/Cl:SnO_2/$K_{0.035}Cs_{0.05}(FA_{0.85}MA_{0.15})_{0.95}Pb(I_{0.85}Br_{0.15})_3$/Spiro-MeOTAD/Au	22.10	1.20	75.60	20.00	[236]
	Optical properties	Cl	Planar	FTO/Cl:SnO_2/$(FAPbI_3)_{0.85}(MAPbBr_3)_{0.15}$/Spiro-MeOTAD/Au	23.60	1.10	69.20	18.10	[165]
		Y	Mesoporous	FTO/Y:SnO_2/$MAPbI_3$/Spiro-MeOTAD/Au	22.45	1.08	70.00	17.29	[219]
		Nb	Planar	FTO/Nb:SnO_2/$MAPbI_3$/Spiro-MeOTAD/Au	22.36	1.08	72.70	17.57	[237]
		Yb	Planar	FTO/Yb:SnO_2/$(FAPbI_3)_{0.85}(MAPbBr_3)_{0.15}$/Spiro-MeOTAD/Au	21.85	1.06	74.40	17.31	[226]
		La	Planar	FTO/La:SnO_2/$MAPbI_3$/Spiro-MeOTAD/Au	21.77	1.09	72.00	17.08	[41]
	Codoped	Al/La	Planar	FTO/Al/La:SnO_2/$Cs_{0.05}(MA_{0.17}FA_{0.83})_{0.95}Pb(I_{0.83}Br_{0.17})_3$/Spiro-MeOTAD/Au	21.92	1.11	78.08	19.13	[164]
		Zr/F	Planar	FTO/Zr/F:SnO_2/$MAPbI_3$/Spiro-MeOTAD/Au	24.39	1.11	71.20	19.19	[238]
		K/F	Planar	ITO/K/F:SnO_2/$CsPbI_2Br$/Spiro-MeOTAD/Ag	14.79	1.31	79.15	15.39	[239]

multilayer as an ETL in PSCs which yielded the PCE of 19.5% for 0.06 cm^2 active area and 12–18% for the larger area devices from 0.15 to 0.85 cm^2 active area.

3.3. Additives

3.3.1. Dopants

Among the initiatives for modifying the LT-SnO_2 ETL is the application of elemental dopants in the SnO_2 crystal lattice. The elements employed as dopants are principally cationic metal elements of different capacities (Li, Al, Ga, La, Ta, Nb, Y, Yb, and Gd)[41,218–226] and anionic halogens including F, Cl.[165,227,228] Broadly speaking, the presence of dopants in SnO_2 could enhance its electrical, optical, and structural properties; however, their mechanisms of action in SnO_2 appeared to be intricate. **Table 4** summarizes the performance and precise parameters of PSCs based on LT-SnO_2 ETL modified via elemental doping. Besides, the doped elements in LT-SnO_2 along with their improved properties have been depicted in **Figure 27**.

Improvement of Electrical Properties: In the case of the electrical properties improvement, the dopants make for the desired energy band alignment between SnO_2 and the perovskite through the energy position shifting of the E_{CB}.[40,229] The

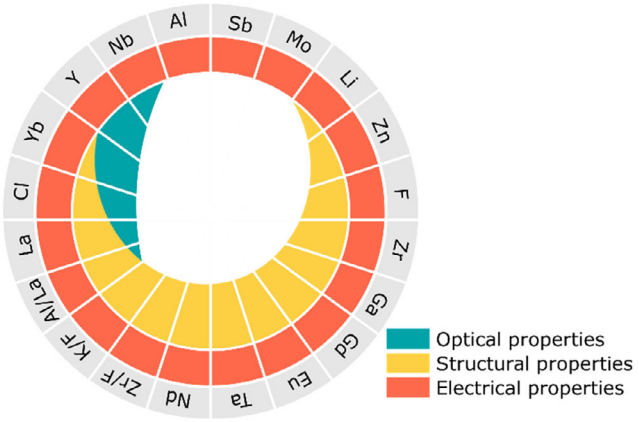

Figure 27. Doped elements in LT-SnO_2 with their improved properties.

cationic and anionic dopants enhance the conductivity or mobility of SnO_2 through increasing the diffusion coefficient and the density of the free charge carriers, respectively.[229,230] Moreover, the enhancement of these electrical properties of SnO_2 leads to reduced resistance, current leakage, and nonradiative charge recombination at the ETL/perovskite interface.[221,231,232] Consequently, the extraction and transport of electron charge at the perovskite/ETL interface are upgraded.[40]

Liu and coworkers[221] have for the first time utilized Nb^{5+} as a dopant in the SnO_2 structure owing to its ionic radius close to Sn^{4+} to adjust the electrical properties of the SnO_2 layers as well as the energy band alignment between SnO_2 and the perovskite. The results demonstrated that Nb^{5+} doping increased the conductivity of SnO_2 ETL and made for a downward shift of E_{CB} position of SnO_2 toward that of the perovskite E_{CB}. Hence, this facilitates the injection of electrons from the perovskite into SnO_2 accelerating the charge transport and reducing nonradiative recombination. Accordingly, they could successfully improve the PCE of PSC devices from 18.06% to 19.38% through the Nb^{5+} doping in SnO_2 ETL.

Bai et al.[229] proposed SnO_2 doping with Sb for the efficient development of inorganic ETLs. Thereby, the doping of SnO_2 with the Sb has resulted in the significant electrical conductivity enhancement due to the increase in the electron carrier concentration. The free electrons overflow has partially pervaded the surface traps and caused the Fermi-level energy position to shift upwards (**Figure 28**). In consequence, the optimized energy band alignment between SnO_2 and perovskite stemming from the change in Fermi-level shifting reduced the charge recombination and thus sustained the electron recombination lifetime and improved the V_{OC}. As a result, the group could manage to increase PSC efficiency from 15.7% to 17.7% through the doping of Sb into SnO_2 ETL. Moreover, the further investigation of this group indicated that the highest conductivity of Sb-doped SnO_2 occurs in the presence of a certain amount of Sb dopant (i.e., 3–5 mol%) in which the concentration of charge carriers, as well as mobility, was at an elevated level. However, the excessive amount of Sb dopant higher than the optimized would bring about the increment in the effective activation energy of the

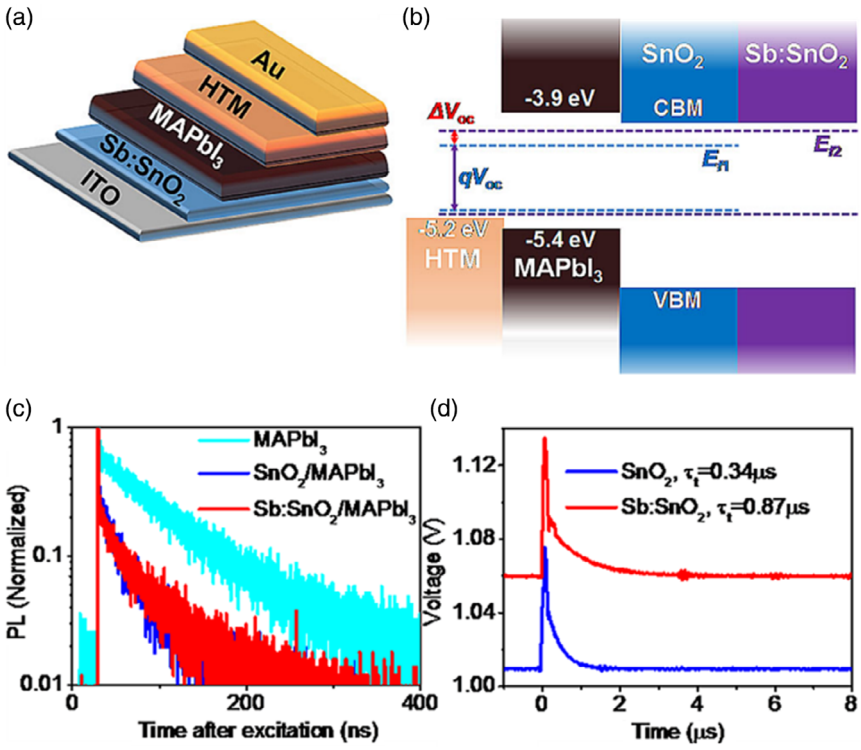

Figure 28. a) Schematic representation of Sb-doped SnO_2-based PSC. b) Energy band diagrams of PSCs based on SnO_2 and Sb-doped SnO_2 ETL, c) normalized TRPL decay curves of perovskite, perovskite/SnO_2, and perovskite/Sb-doped SnO_2 layers, and d) normalized transient photo-voltage decay curves of ETLs based on SnO_2 and Sb-doped SnO_2 under 1 sun. Reproduced with permission.[229] Copyright 2016, John Wiley and Sons.

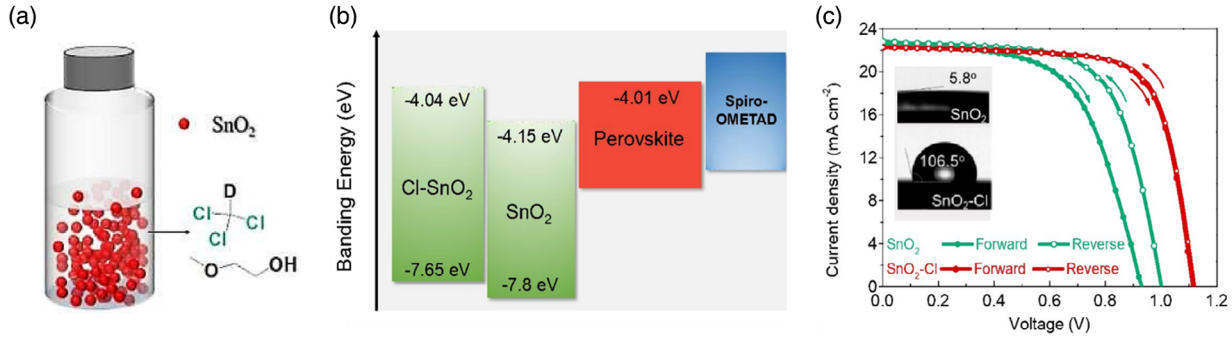

Figure 29. a) Schematic representation of the process of formation of Cl-doped SnO_2 through dispersing SnO_2 nanocrystals in 2-methoxy ethanol and chloroform-D solution with a volume ratio of 1:1. b) Energy band diagram of PSCs based on SnO_2 and Cl -doped SnO_2, and c) *J–V* characteristics of SnO_2 and Cl-doped SnO_2-based devices along with contact angle of perovskite solution on SnO_2 and Cl-doped SnO_2 ETLs indicating the hydrophobic surface of the latter. Reproduced with permission.[165] Copyright 2020, Royal Society of Chemistry.

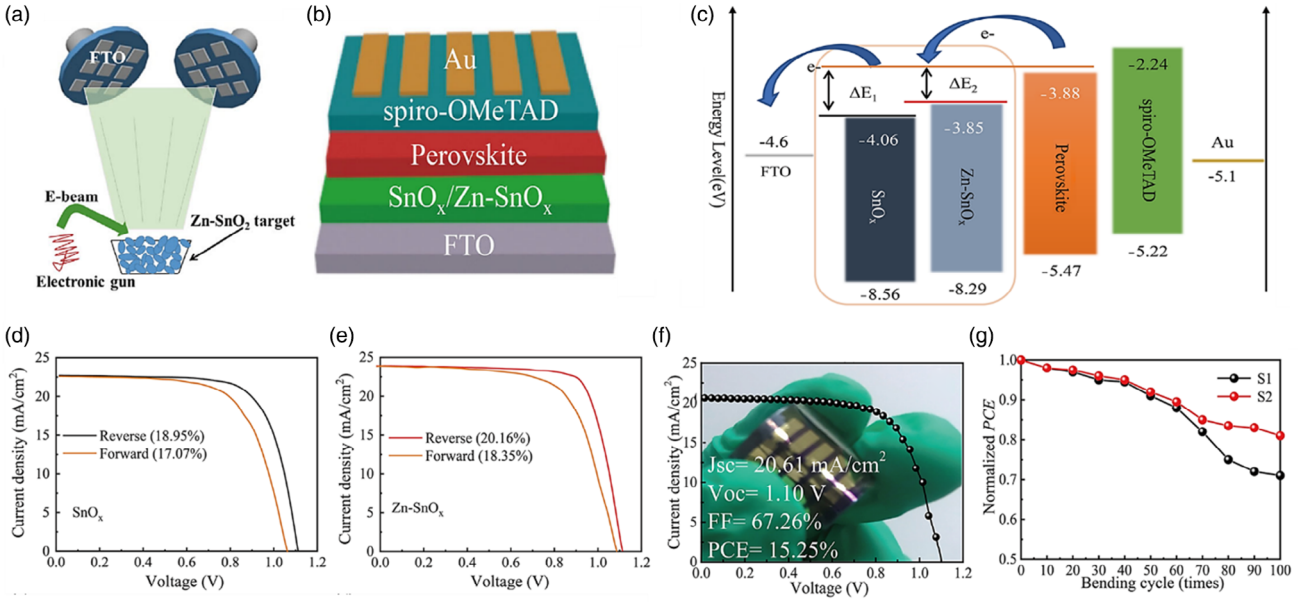

Figure 30. a) Schematic representation of the Zn-doped SnO_2 deposition process through E-beam evaporation method. b) Schematic depiction of PSC structure based on SnO_2 and Zn-doped SnO_2 ETLs. c) Energy band diagram of PSCs based on SnO_2 and Zn-doped SnO_2, *J–V* characteristics of the devices based on d) SnO_2 and e) Zn-doped SnO_2. f) *J–V* characteristics and g) normalized PCE against the number of bending cycles of the flexible devices based on Zn-doped SnO_2 ETL. Reproduced with permission.[76] Copyright 2020, John Wiley and Sons.

donor and a rapid decrement in carrier mobility leading to intensified disorder or scattering.

Enhancement of Structural Properties: With regard to the utility of dopants for structural properties improvement, their presence in the SnO_2 crystal lattice would increase the lattice constant which in turn increases the grain size and diminishes the crystal aggregation.[41,220] Hence, these phenomena induce the formation of a layer of uniform, dense, and pinhole-free coverage[220] impacting upon the perovskite deposition and leading to an increase in the size of perovskite grains as well as a grain boundary decrease in the perovskite layer.[165] Furthermore, it is observed that cationic dopants of capacities less than Sn^{4+} (e.g., Li^{+}, La^{+}, Zr^{3+}, Eu^{3+}, and Nd^{2+}),[41,231,233–235] as well as anionic dopants (i.e., F^{-}, Cl^{-}),[165,227,236] could passivate the oxygen vacancy defects. Therefore, in the company of these dopants, a reduction in interfacial defect or trap density is realized.[236] What is more, it has been specifically reported that SnO_2 doped with halogen element fluorine represents superior lattice matching with that of the FTO substrate owing to its high resemblance with FTO.[227]

Gong and coworkers[165] produced chlorine-doped SnO_2 nanocrystals (Cl-doped SnO_2) (**Figure 29**a). They recognized that in consequence of the Cl halogen making the surface of Cl-doped SnO_2 ETL more hydrophobic (Figure 29c), the grain size and crystallization of perovskite have been remarkably enhanced which, in turn, led to a significant reduction in the charge trap density and recombination of perovskite film. Besides, more expedited charge extraction and transport are brought about by the establishment of the desired band alignment between the perovskite and the ETL (Figure 29b). Accordingly, via doping

SnO_2 with chlorine, the group could successfully increase the PCE of PSCs from 15.07% to 18.1% (Figure 29c).

Song et al.[76] could also improve the electrical conductivity of ETL via doping LT-SnO_2 ETL with Zn (**Figure 30**a,b). This might have reduced the distance between the Fermi level and the E_{CB} of ETL (Figure 30c) and have enhanced its conductivity through the formation of zinc interstitials (Zn_i) or oxygen vacancies (V_O). Notwithstanding, semiconductor conductivity could be enhanced by the reduction in defect density. Besides, due to the presence of Zn^{2+} dopant, the UV-ray absorption of ETL increased which alleviated the perovskite layer impairments under UV light. Moreover, the results demonstrated that the SnO_2 crystal lattice size came to have a significant increment with zinc doping which implies the larger the lattice size the lower the defect density. Therefore, the doping of Zn^{2+} in SnO_2 reduces the resistance of ETLs. Furthermore, Zn^{2+} doping elevated the E_{CB} of the ETL, leading to a more perfect electron transport as well as reducing the E_{CB} difference between the perovskite and that of the ETL, resulting in a V_{OC} decline mitigation. On that account, the group could manage to boost the PCE of PSCs from 18.95% to 20.16% through doping SnO_2 with Zn (Figure 30d,e). Thereupon, they could also fabricate a flexible PSC based upon Zn doped-SnO_2 ETL exhibiting a 15.25% PCE which retained 84% of its initial efficiency after 100 bending cycles (Figure 30f,g).

Improvement in Optical Properties: Dopants usually change the electrical properties of SnO_2. Nevertheless, some of them, such as La,[41] Nb,[237] Y,[219] and Cl,[165] enhance the transparency of the SnO_2 layer through the elevation of the bandgap,[219] reducing the crystalline aggregation[41] and/or smoothing the surface.[237] Thus, these dopants increase the photocurrent in PSCs by improving the optical properties of SnO_2 ETL.[41,219,237] Xu and coworkers[41] employed La-doped SnO_2 as a blocking layer within planar PSCs. The inferior surface morphology of LT-SnO_2, especially the presence of pinholes after the low-temperature annealing process, confines its application in the PSCs. Therefore, to surmount the SnO_2 drawbacks, the group-doped lanthanum (La) in the SnO_2 layer, which has resulted in the reduced aggregation of SnO_2 crystals and construction of a uniform film. Moreover, it was observed that La doping affects the crystallization of SnO_2 during the annealing process and improves the morphology of the SnO_2 layer. Besides, La doping makes for an enhancement in the conductivity and upward shifting of the E_{CB} of the ETL, which in turn leads to electron extraction and V_{OC} increment as well as recombination and hysteresis abolishment. In consequence, the group could manage to advance the performance of PSCs from 14.24% to 17.08% PCE via doping SnO_2 with the La.

Yang et al.[219] reported that SnO_2 doped with yttrium (Y-doped SnO_2) has significantly reduced hysteresis and elevated PSC performance (**Figure 31**a). This facilitated the formation of well-aligned SnO_2 nanosheet arrays of a higher homogeneous distribution, which has served the more beneficial perovskite diffusion and the better interface between perovskite and ETL. Furthermore, the Y-doped SnO_2 nanosheet arrays demonstrate higher conductivity as well as facile and firm charge extraction and transport (Figure 31b). Ever since the ETL bandgap is ascended by the Y doping in SnO_2, the optical transparency of the layer increases as well (Figure 31c). What is more, owing to the more perfect homogeneous distribution of Y-doped SnO_2 nanosheet arrays, light scattering is also reduced in order that the light absorption of perovskite film using Y-doped SnO_2 ETL is approximately higher than that of the pristine SnO_2 ETL throughout the visible spectrum. This could be attributed to the enhancement of the perovskite/ETL interface and the superior deposition of the perovskite material. This improved light absorption property of the perovskite film built upon the Y-doped SnO_2 ETL might enable the perovskite absorbent layer to harvest light more efficiently and thus render a higher J_{SC} in PSCs based on Y-doped SnO_2 ETL. Conclusively, by employing the doping of SnO_2 with Yttrium, the group could boost the PCE of PSCs from 13.38% to 17.29%.

Elemental Co-Dope: Simultaneous co-doping of two elements has been utilized to further improve the properties of SnO_2 ETL. Sakthivel et al.[164] fabricated planar PSCs based upon SnO_2 ETL doped with the trivalent metals Al and La. Therein, they could manage to enhance the transparency by adding aluminum to SnO_2 ETL which increased J_{SC}, whereas the addition of lanthanum to SnO_2 ETL made for an increased FF and conductivity achievement. Besides, the simultaneous co-doping of the two elements Al and La in an equal proportion allowed the elevation in band alignment and electron injection between the perovskite/ETL. Despite that of SnO_2 ETL, Al/La co-doped SnO_2 ETL possessed high transmittance, desired energy band

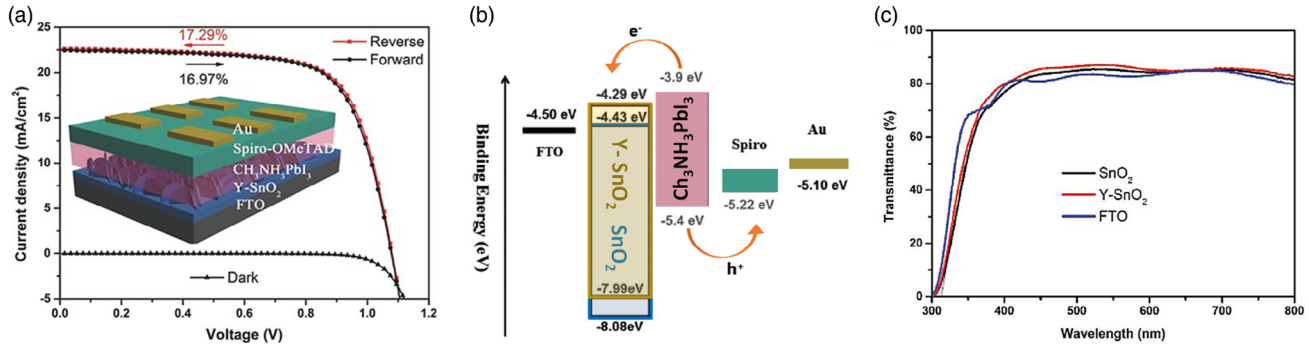

Figure 31. a) *J–V* characteristics of the PSC device based on Y-doped SnO_2 with a schematic representation of the PSC structure based on Y-doped SnO_2 ETL. b) Energy band diagram of PSCs based on SnO_2 and Y-doped SnO_2, and c) Transmittance spectra of SnO_2 and Y-doped SnO_2 layers with FTO substrate. Reproduced with permission.[219] Copyright 2017, John Wiley VCH.

alignment between perovskite/ETL, and efficient charge transport. Therefore, the group could enhance the PCE of PSCs from 17.21% to 19.13% through co-doping of SnO_2 ETL with equivalent amounts of Al and La elements.

The energy band position and the conductivity of the ETL are fundamental factors suppressing the performance of PSCs. To tackle these sticking points, Tian and coworkers[238] applied co-doping of Zr/F in SnO_2 ETL through the addition of ZrF_4. Since ZrO_2 is of a high conduction band position, doping the Zr increases that of the E_{CB} of SnO_2 that facilitates its alignment with the perovskite, diminishes the energy obstacle against electron extraction, avoids the recombination at the ETL/perovskite interface, and thus increases the V_{OC}. Correspondingly, halogen F doping is of the n-type doping that contributes to the electron carrier density increment in SnO_2, thereby improving the conductivity of ETL and J_{SC}. In conclusion, they managed successfully to raise the PCE of PSCs from 17.35% to 19.19% through simultaneous co-doping of SnO_2 ETL with F and Zr elements. Zhang et al.[239] also used simultaneous K/F doping in SnO_2 ETL with the addition of KF. Thus, by adjusting the conduction band of the SnO_2 film, they created a better match with the conduction band of the perovskite film, thus increasing the V_{OC}. In addition, fluoride ions from ETL can migrate to the bottom of the perovskite layer and reduce nonradiative recombination and trap states of perovskite films by passivating the ETL/perovskite interface.

3.3.2. LT-SnO_2-Based Composites and Complexes

The utilization of SnO_2-based nanocomposites in the other solar cell configurations including dye sensitized solar cells (DSSCs) has been already suggested.[240] In the whole course, to improve the performance of LT-SnO_2 ETLs, both organic materials such as graphene,[241] carbon nanodots,[242] and nanotubes,[243] as well as inorganics such as Bi_2O_2S,[244] KCl,[245] and MXene,[91] have been utilized to form a complex with SnO_2. The application of these complexes renders several advantages like reduced recombination at the interface, elevated charge transport, increased stability of the precursor ink, and higher wettability. In this section, the research literature on the application of SnO_2 ETL composite and complex is surveyed in three categories including SnO_2/carbon composites, SnO_2/inorganic composites, and SnO_2-based complexes which their working mechanisms and performances in PSCs based on LT-SnO_2 are thoroughly discussed. Eventually, the performance and precise PV characteristics of PSCs based on LT-SnO_2 composites and complexes are summarized in **Table 5**.

SnO_2/Carbon Composites: Wang and coworkers[242] obtained carbon nanodots (NDs) using the hydrothermal method and applied them within SnO_2 ETLs (**Figure 32**a). The results demonstrated that owing to the presence of carbon NDs, the density of trap states was reduced and the mobility in SnO_2 film was enhanced. The schematic illustration of the electron transport from the perovskite layer to the SnO_2: carbon NDs composite layer is represented in Figure 32b,c. Therein, resulting from the reduction of defect and resistance in SnO_2: carbon NDs ETL and the interaction between carbon NDs and FA or MA cations in the perovskite layer, electrons could be extracted and transported more facilely by means of carbon NDs in ETL. Therefore, through the formation of SnO_2: carbon NDs composites, this group could successfully increase the PCE of LT-SnO_2-based PSCs from 18.54% to 20.03% (Figure 32d).

Tang et al.[243] utilized carbon nanotubes (CNTs) in SnO_2 ETLs and designated high-performance, hysteresis-free planar PSCs. Under the utility of SnO_2 and CNTs composites, the conductivity of ETL has been significantly improved, and the trap states density has been reduced leading to a more effective electron extraction and transport. Therein, they could elevate the PCE of LT-SnO_2-based PSCs from 17.9% to 20.33% by making the composites of SnO_2:CNTs. Hui et al.[246] employed red carbon quantum dots (QDs) enriched by carboxylic acid and hydroxyl functional groups for synthesizing the composites with SnO_2 and the preparation of ETL. The results showed that by making composites of SnO_2 with red carbon QDs, the quality of perovskite films was improved due to the reduction in Gibbs-free energy of SnO_2 surface owing to the thereby increased hydrophilicity. This was remarkable in the way that the crystal phase of perovskites grown on SnO_2: red carbon QDs composite ETL was purer and more uniform than that of the perovskites grown on SnO_2 ETL. Moreover, mobility has been significantly enhanced in this composite compared to that of the pristine SnO_2, which leads to improved charge extraction and transport. Conclusively, through the application of SnO_2 with red carbon QDs composite, they could manage to increase the efficiency of LT-SnO_2-based PSCs from 19.15% to 22.77%.

Employing a furnace aerosol reactor, Kouhnavard and coworkers[247] converted 2D graphene oxide (GO) nanosheets into 3D crumpled structures, then utilized them to make a composite with SnO_2 and further improve the performance of PSCs based on SnO_2 ETL. They demonstrated that the application of SnO_2 with crumpled-GO composite ETL enhanced the charge transport in ETL and reduced charge recombination in the perovskite layer. Likewise, Zhou et al.[248] applied the SnO_2:graphene QDs composite as the LT-ETL in the PSC. The results indicated that this composite presented higher electron mobility, a more perfect film coverage, and desired energy level compared with that of SnO_2, which facilitated and alleviated the charge transport and recombination, respectively. By optimizing the size and concentration of graphene QDs, they improved the conductivity, the film coating uniformity, and the Fermi-level energy adjustment of the ETL with perovskite which better electron transport and reduced charge recombination at the interface. In consequence, benefitting from SnO_2 with graphene QDs (with 0.5% wt. of graphene QDs) composite ETL, the group could successfully boost the efficiency of LT-SnO_2-based PSCs from 16.80% to 19.60%. In the same manner, Pang et al.[249] employed SnO_2 with Graphene QDs composited as ETL in the architecture of planar PSCs. There again, the results demonstrated that the incorporation of the graphene QDs between SnO_2 and perovskite could enhance the perovskite film quality, expedite the electron transport, and diminish the charge recombination. Consequently, they could increase the PCE of LT-SnO_2-based PSCs from 18.60% to 21.10% making use of SnO_2 with graphene QDs composite. Zhang et al.[250] used graphdiyne (GDY) to prepare the SnO_2 ETL layer. GDY has a new carbon allotrope with a combination of sp and sp^2 and a completely π-conjugated and rigid structure. By maximizing collocation between SnO_2 and perovskite, GDY accelerates electron extraction and improves interface as well as

Table 5. Precise performance and characteristics of PSCs based on LT-SnO_2 composites and complexes.

SnO_2 modification				Cell configuration	J_{SC} [mA cm^{-2}]	V_{OC} [V]	FF [%]	Eff [%]	Ref.
Compositing & Complexing	SnO_2/Organic Composites	Carbon NDs	Planar	ITO/SnO_2:Carbon NDs/ $Cs_{0.05}FA_{0.81}MA_{0.14}PbI_{2.55}Br_{0.45}$/ Spiro-MeOTAD/Au	23.14	1.10	79.00	20.03	[242]
		Carbon NTs	Planar	ITO/SnO_2:Carbon NTs/$MAPbI_3$/ Spiro-MeOTAD/Au	23.26	1.12	78.23	20.33	[243]
		Red Carbon QDs	Panar	ITO/SnO_2:Red Carbon QDs/ $Cs_{0.05}FA_{0.81}MA_{0.14}PbI_{2.55}Br_{0.45}$/ Spiro-MeOTAD/$MoO_3$/Au	24.10	1.14	82.90	22.77	[246]
		crumpled-GO	Planar	FTO/SnO_2:crumpled GO/$MAPbI_3$/ Spiro-MeOTAD/Au	21.03	0.95	54.00	10.86	[247]
		Graphene QDs	Planar	FTO/SnO_2:Graphene QDs/ $Cs_{0.05}FA_{0.81}MA_{0.14}PbI_{2.55}Br_{0.45}$/ Spiro-MeOTAD/Au	23.50	1.08	77.00	19.60	[248]
			Planar	ITO/SnO_2:Graphene QDs/$MAFAPbI_3Cl_{3-x}$/ Spiro-MeOTAD/Ag	24.40	1.11	78.00	21.10	[249]
		Graphdiyne (GDY)	Planar	ITO/SnO_2:GDY/$CsFAMAPb(I_xBr_{1-x})_3$/ Spiro-MeOTAD/Au	23.32	1.13	79.62	21.11	[250]
		g-C_3N_4 QDs	Planar	ITO/SnO_2:g-C_3N_4 QDs/ $Cs_{0.05}FA_{0.81}MA_{0.14}PbI_{2.55}Br_{0.45}$/ Spiro-MeOTAD/Au	24.03	1.17	78.00	22.13	[241]
		S doped g-C_3N_4	Planar	FTO/SnO_2:S-doped g-C_3N_4/$CsFAMAPbIBr_2$/ Spiro-MeOTAD/Au	23.43	1.13	76.00	20.33	[251]
		TFE	Planar	ITO/SnO_2:TFE/$FA_xMA_{1-x}Pb(I_y,Cl_z,Br_{1-y-z})_3$/ Spiro-MeOTAD/Au	23.91	1.12	78.00	20.92	[123]
		TMAH	Planar	ITO/SnO_2:TMAH/$FA_{0.75}MA_{0.25}PbI_{2.5}Br_{0.5}$/ Spiro-MeOTAD/Au	23.31	1.15	78.43	21.05	[252]
		Girard's reagent T (GRT)	Planar	ITO/SnO_2:GRT/ $Rb_{0.05}(FA_{0.95}MA_{0.05})_{0.95}PbI_{2.85}Br_{0.15}$/ Spiro-MeOTAD/Au	22.92	1.14	82.30	21.63	[253]
		Monosodium glutamate (MSG)	Planar	FTO/SnO_2:MSG/$FA_{0.5}MA_{0.5}PbI_3$/ Spiro-MeOTAD/Au	22.55	1.05	74.38	17.71	[254]
		Ethoxylated polyethylenimine (PEIE)	Planar	ITO/SnO_2:PEIE/$Cs_xFA_yMA_{1-x-y}PbI_{3-x}Cl_x$/ Spiro-MeOTAD/Ag	23.83	1.14	76.00	20.61	[255]
		Heparin potassium (HP)	Planar	ITO/SnO_2:HP/ $Cs_{0.05}FA_{0.85}MA_{0.10}Pb(I_{0.97}Br_{0.03})_3$/ Spiro-MeOTAD/Au	25.00	1.16	79.20	23.03	[256]
				PET/ITO/SnO_2:HP/ $Cs_{0.05}FA_{0.85}MA_{0.10}Pb(I_{0.97}Br_{0.03})_3$/ Spiro-MeOTAD/Au	23.74	1.09	75.24	19.47	
		PVP	Planar	FTO/SnO_2:PVP/$(FAPbI_3)_{0.97}(MAPbBr_3)_{0.03}$/ Spiro-MeOTAD/$MoO_3$/Ag	23.83	1.12	73.27	19.55	[257]
	SnO_2/Inorganic Composites	ZnO	Planar	ITO/SnO_2:ZnO/$MAPbI_3$/ Spiro-MeOTAD/Ag	19.60	1.06	68.80	14.30	[240]
			Mesoporous	ITO/SnO_2:ZnO/Al_2O_3/$MAPbI_3$/Spiro-MeOTAD/Ag	19.50	1.07	72.80	15.20	[240]
		KCl	planar	ITO/SnO_2:KCl/$(FAPbI_3)_{0.95}(MAPbBr_3)_{0.05}$/ Spiro-MeOTAD/Au	24.20	1.13	80.70	22.20	[245]
		CdS QD	Planar	FTO/SnO_2:CdS QD/$MAPbI_3$/ Spiro-MeOTAD/Ag	23.45	1.13	78.42	20.78	[258]
		Bi_2O_2S	Planar	ITO/SnO_2:Bi_2O_2S/$MAPbI_3$/Spiro-MeOTAD/ MoO_3/Ag	22.35	1.09	70.30	17.13	[244]
			Planar	ITO/SnO_2: Bi_2O_2S $Cs_{-0.05}FA_{0.81}MA_{0.14}PbI_{2.55}Br_{0.45}$/ Spiro-MeOTAD/$MoO_3$/Ag	22.98	1.15	76.20	20.14	[244]

Table 5. Continued.

SnO_2 modification			Cell configuration	J_{SC} [mA cm^{-2}]	V_{OC} [V]	FF [%]	Eff [%]	Ref.
	Bismuthene	Planar	FTO/SnO_2:Bismuthene/ $(FAPbI_3)_{0.97}(MAPbBr_3)_{0.03}$/ Spiro-MeOTAD/Au	24.71	1.09	75.49	18.75	[259]
	TiAcAc	Planar	ITO/SnO_2:TiAcAc/$FA_{0.85}MA_{0.15}PbI_{3-x}Br_x$/ Spiro-MeOTAD/$MoO_x$/Au	24.30	1.13	74.40	20.40	[295]
	MXene (Ti_3C_2)	Planar	ITO/SnO_2:Ti_3C_2/$MAPbI_3$/Spiro-MeOTAD/Ag	23.14	1.06	75.00	18.34	[213]
	MXene-basedTiO_2 QDs	Planar	FTO/SnO_2:MXene-based TiO_2 QDs/ $(FAPbI_3)_{0.97}(MAPbBr_3)_{0.03}$/ Spiro-MeOTAD/Au	24.16	1.07	74.00	19.14	[91]
	N,S codoped MXene QD	Planar	ITO/SnO_2: N, S codoped-Mxene QD/ $FA_{0.9}MA_{0.05}Cs_{0.05}PbI_{0.98}Br_{0.02}$/ Spiro-MeOTAD/$MoO_3$/Au	24.96	1.17	79.00	23.34	[260]
	PMo_{12}	Mesoporous	FTO/SnO_2:PMo_{12}/*m*-TiO_2/ZrO_2 + $MAPbI_3$/C	22.70	0.85	64.00	12.60	[261]
	AlO_6	Planar	FTO/SnO_2:AlO_6/$MAPbI_3$/Spiro-MeOTAD/Au	23.31	1.13	79.80	21.04	[262]
SnO_2-based Complexes	PEG	Planar	ITO/SnO_2—PEG/ $Cs_{0.05}FA_{0.81}MA_{0.14}PbI_{2.55}Br_{0.45}$/ Spiro-OMeTAD/Au	22.67	1.11	81.80	20.80	[265]
		Planar	ITO/SnO_2—PEG/ $MA_{0.61}FA_{0.37}Cs_{0.02}PbI_{2.96}Br_{0.074}$/PEDOT:PSS/ MoO_3/Ag	18.34	0.96	61.50	10.82	[264]
		Mesoporous	ITO/SnO_2/SnO_2—PEG/ $(Cs_{0.05}FA_{0.95}PbI_3)_{0.97}(MAPbBr_3)_{0.03}$/ Spiro-MeOTAD/Ag	24.56	1.10	77.10	20.82	[267]
	Thiourea	Planar	ITO/SnO_2—Thiourea/ $Cs_{0.05}FA_{0.81}MA_{0.14}PbI_{2.55}Br_{0.45}$/C	22.19	1.08	56.64	13.64	[268]
	Urea	Planar	ITO/SnO_2—Urea/$MAPbI_3$/Spiro-MeOTAD/Au	23.51	1.13	76.24	20.25	[269]
	BF_4^-	Mesoporous	FTO/SnO_2 NR/SnO_2—BF_4^-/ $Cs_{0.05}(MA_{0.15}FA_{0.85})_{0.95}Pb(I_{0.85}Br_{0.15})_3$/ Spiro-MeOTAD/Au	23.45	1.15	78.77	21.35	[270]
	Oleic acid (OA)	Inverted	FTO/NiO_x/$MAPbI_3$/$PC_{61}BM$/SnO_2—OA/Ag	21.04	0.85	51.10	9.17	[271]
	TMAOH	Inverted	FTO/NiO_x/$MAPbI_3$/$PC_{61}BM$/ SnO_2—TMAOH/Ag	19.51	1.06	75.70	15.66	
	TBAOH	Inverted	FTO/NiO_x/$MAPbI_3$/$PC_{61}BM$/ SnO_2—TBAOH/Ag	21.62	1.08	80.50	18.77	
	Phytic acid (PA)	Planar	FTO/SnO_2—PA/$MAPbI_3$/Spiro-MeOTAD/Ag	23.76	1.07	81.00	21.43	[272]
	TASiW-12	Planar	ITO/SnO_2—TASiW-12/FAMAPb(I,Br,Cl)$_3$/ Spiro-MeOTAD/Au	24.28	1.16	81.35	22.84	[273]

[a]Nanodots: NDs, Nanotubes: NTs, Quantum dots: QDs.

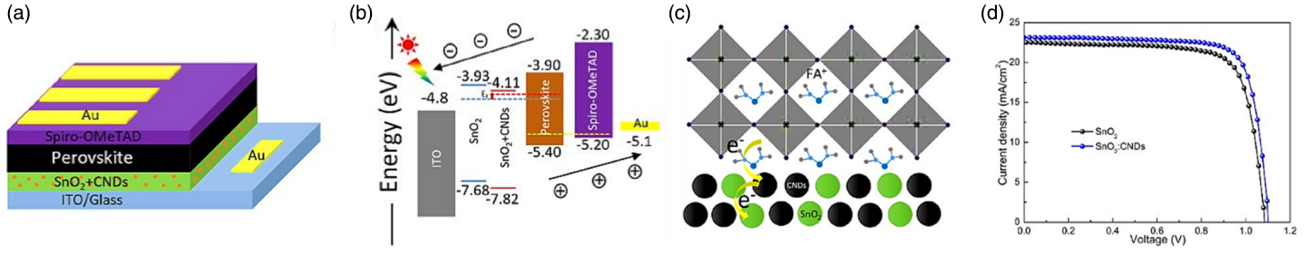

Figure 32. a) Structure representation of the SnO_2:carbon NDs PSC device. b) Energy-level diagram of each layer. c) A schematic of the electron transport from the perovskite layer to the SnO_2:carbon NDs. d) *J*–*V* curves of the PSC device based on SnO_2 and SnO_2:carbon NDs. (In the images, SnO_2:carbon NDs is labeled as SnO_2 + CND.). Reproduced with permission.[242] Copyright 2019, Royal Society of Chemistry.

passivates surface defects. Thus, they succeeded to achieve PCE of 21.11% using SnO_2:GDY composite.

Chen and coworkers[241] utilized a carbonitride-modified SnO_2 nanocomposite, i.e., SnO_2/graphitic carbon nitride (g-C_3N_4) quantum dots nanocomposite, as the ETL in the PSC structure. g-C_3N_4 possesses high conductivity and chemical stability, the capability to improve traps, and corrosion resistance. As such, they exhibited that the high-conductive g-C_3N_4 could effectively passivate oxygen-vacancy-reduced-traps through modifying the electron density distribution around the SnO_2 crystal unit, thereby increasing charge transport within the bulk and at the interface. Furthermore, besides the high conductivity, this nanocomposite offers extra desirable electrical properties such as optimal energy-level alignment. Therefore, they could manage to elevate the efficiency of LT-SnO_2-based PSCs from 20.21% to 22.13% with the utility of making SnO_2:g-C_3N_4 nanocomposite. Cao et al.[251] also used sulfur-doped g-C_3N_4 nanoparticles (S doped-g-C_3N_4) to prepare the SnO_2:S-doped g-C_3N_4 nanocomposite, which increased electron mobility and conductivity of ETL layer. In addition, by passivation of the ETL/perovskite interface via the interaction of sulfur atoms in S-doped g-C_3N_4 with undercoordinated lead (Pb) ions in perovskite films, the surface recombination of the carriers was significantly reduced. Therefore, using this strategy, the PCE increased from 18.98% to 20.33%.

Luan et al.[123] employed 2,2,2-trifluoroethanol (TFE) in SnO_2 ETL and increased its mobility through the preparation of a composite. They showed that this structure has dramatically decreased the density of trap states at the interface and thorough the perovskite absorbent which in turn has remarkably diminished the charge recombination. Therein, by making a composite of SnO_2 with TFE, the group realized the efficiency enhancement of LT-SnO_2-based PSCs from 19.17% to 20.92%. Huang and coworkers[252] fabricated and developed highly efficient PSCs using SnO_2 and tetramethylammonium hydroxide (TMAH) composites as LT-ETL. The results indicated that TMAH has led to conductivity enhancement as well as charge transport enhancement and accordingly, they could manage to increase the efficiency of LT-SnO_2-based PSCs from 18.14% to 21.05% using this composite structure.

Bi et al.[253] using Girard's Reagent T (GRT) incorporating molecules with several functional groups to modify SnO_2 nanoparticles. Using SnO_2: GRT nanocomposite, they were able to increase the PCE of PSCs from 19.77% to 21.63% through the following three factors: 1) Improving the electrical properties and quality of SnO_2 film by inhibiting nanoparticle agglomeration through strong chemical interactions between GRT and SnO_2 2) facilitate vertical growth and grain size increasing of perovskite crystals by improving wettability and reducing the surface roughness of the SnO_2 layer, and 3) reduction of surface defects through the effective passivation of the quaternary ammonium cation and chloride in GRT for anionic and cationic defects at the surface of the perovskite film.

Zhang et al.[254] used monosodium glutamate (MSG) to prepare the SnO_2:MSG composite. MSG is known as gourmet powder and includes certain functional groups such as carboxyl group, amino group, and Na^+ cation ion. As a food additive, MSG is a nontoxic, low-cost, and abundant reserves, and more importantly, MSG can be dissolved directly in water. They reported that due to the interaction between electrical dipole and strong crosslinking MSG, the ETL/perovskite interface is optimized, charge transfer is accelerated, and interface defects are reduced. Accordingly, this group succeeded to increase the PCE from 16.56% to 17.71%. Huang et al.[255] used polyethylenimine ethoxylated (PEIE) to make the SnO_2: PEIE nanocomposite. PEIE is an organic polymer with a simple aliphatic amine group that can effectively smoothen the surface of the substrate (such as ITO) and reduce its work function. In addition, the presence of PEIE improves the conductivity and mobility of SnO_2 film. Finally, this group was able to increase the PCE of PSCs from 18.74% to 20.61% by using SnO_2: PEIE composite.

You et al.[256] reported that they used a biological polymer of heparin potassium (HP) to modulate the arrangement of SnO_2 nanocrystals and to fabricate the SnO_2:HP composite. Heparin is a linear sulfated polysaccharide containing ≈2.7 sulfate groups per saccharide, which can be coordinated with Pb atoms of perovskite. High negative charge density of HP leads to stabilization of SnO_2 nanocrystals in dispersion. Functional groups in HP can bind perovskites to well-arranged SnO_2 nanocrystals, leading to vertically aligned crystal growth. Thus, using SnO_2:HP composite, they managed to achieve PCEs to 23.03% (with rigid glass/ITO substrate) and 19.47% (with flexible PET/ITO substrate). Zhang et al.[257] used poly vinylpyrrolidone (PVP) to fabricate the SnO_2:PVP composite. They reported that by placing of PVP chains between SnO_2 nanoparticles, the accumulation of SnO_2 nanoparticles is inhibited, and the morphology of SnO_2 film is improved. PVP reduces leakage current at the interface by suppressing ETL/perovskite interface defects and thus improves PSC performance. According to their results, charge transfer at very high PVP concentrations is reduced due to poor PVP conductivity. As a result, it is necessary to optimize the PVP concentration to achieve the desired efficiency (optimal PVP concentration = 2 mg mL^{-1}). Using SnO_2:PVP compound.

SnO_2/Inorganic Composites: Song et al.[240] prepared SnO_2: ZnO nanocomposites with different ZnO/SnO_2 ratios as low-temperature ETL to use in planar PSCs and compared this composite ETL with those of pristine ZnO and SnO_2. The resulted composite exhibited higher temperature stability than that of pure ZnO since the number of hydroxyl groups and acetate ligands remaining on the surface has been decreased. Moreover, the results implied a high increase in electron extraction and charge recombination resistance at the perovskite/ETL interface in PSCs based on SnO_2:ZnO composite ETL in comparison with that of PSCs based on pristine ZnO and SnO_2 ETLs. Accordingly, this group could successfully achieve a PCE of 14.3% for planar PSCs based on SnO_2:ZnO and 13.9% and 12.4% for PSCs based upon pristine ZnO and SnO_2 ETLs, respectively. What is more, they also employed the mesoporous Al_2O_3 layer between the composite ETL and the perovskite layer to further enhance the efficiency and performance of SnO_2:ZnO ETL-based PSCs and realized a 15.2% PCE for SnO_2:ZnO ETL-based mesoporous PSCs.

In the application of other inorganic material, Zhu et al.[245] utilized the SnO_2:KCl composite as a LT-ETL in planar PSCs to simultaneously passivate the defects at the ETL/perovskite interface as well as the perovskite film boundaries owing to the infiltration of K^+ ions from the ETL into the perovskite. Therefore, by the alternative SnO_2:KCl composite ETL to that of SnO_2 ETL in planar PSC structure, they managed to elevate

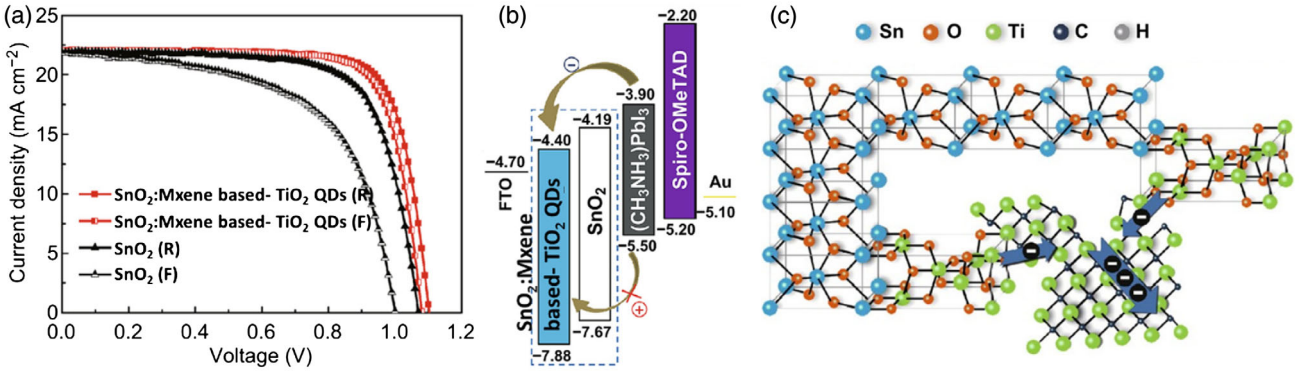

Figure 33. a) Hysteresis and *J–V* curves of champion PSCs with SnO_2:MXene-based TiO_2 QDs and SnO_2 ETL. b) Energy-level diagram of each layer. c) The role of 2D MXene as conductive bonded bridges in the SnO_2:MXene based- TiO_2 QDs composite. Reproduced with permission under the terms of the Creative Commons CC BY license.[91] Copyright 2020, the Authors. Published by Springer Nature.

the PCE from 20.2% to 22.2%. Lv et al.[258] used the SnO_2:CdS QD composite as ETL in the PSC structure. Adding CdS QD to SnO_2 has three advantages: 1) ETL electrical conductivity improvement, 2) charge transfer acceleration due to better energy-level matching between ETL and perovskite, and 3) passivation of Pb defects in the ETL/perovskite interface by the coordination reaction of S^{2-} ions in ETL. Therefore, with aid of SnO_2: CdS QD composite, they increased the PCE of PSCs from 18.27% to 20.78%.

Chen and coworkers[244] prepared and employed SnO_2:Bi_2O_2S composite as a LT-ETL in the fabrication of planar PSCs and compared its performance with that of SnO_2 ETL. Therein, Bi_2O_2S nanoparticles served to alleviate the recombination and increase charge transport as well as PSC stability by passivating oxygen vacancy defects throughout the SnO_2 film. Besides, SnO_2: Bi_2O_2S composite film enhanced perovskite crystalline quality owing to the adjustment of ETL morphology and interface. Thereupon, according to the results, the replacement of SnO_2 ETL with that of SnO_2:Bi_2O_2S composite ETL in the architecture of planar PSCs resulted in an efficiency increment from 14.61% to 17.13%. Furthermore, they could manage to boost the PCE to 20.14% through the alteration of the $MAPbI_3$ absorbent layer to $Cs_{0.05}FA_{0.81}MA_{0.14}PbI_{2.55}Br_{0.45}$. Through the combination of Bismuthene with SnO_2, Xue et al.[259] developed a LT-SnO_2-based composite ETL and compared its performance with that of SnO_2 ETL in PSC. As regards the lower surface roughness and hydrophobicity of SnO_2:Bismuthene composite layer than that of the pristine SnO_2, it served to increase the grain size of the perovskite layer and the energy bands in this composite shifted to higher levels compared with that of SnO_2. Besides, the utilization of Bismuthene has led to an improvement in the optical transmittance and electrical conductivity of ETL and decreased the interfacial resistance between the perovskite/ETL. Moreover, SnO_2: Bismuthene composite has significantly assisted in the combination of a lattice-matching attribute of adjacent lattice-spacing between Bismuthene and SnO_2 crystals owing to its lower interfacial mismatch than that of the pristine SnO_2. They demonstrated that the PCE of PSCs increased from 18.55% to 19.38% by the alternative application of SnO_2: Bismuthene composite ETL to the pristine SnO_2 ETL. Qian et al.[237] optimized the electron transport property of SnO_2 by adding the titanium diisopropoxide bis (acetylacetonate) (TiAcAc) agent molecule in a solution of SnO_2 nanoparticles and making the SnO_2:TiAcAc composite. The TiAcAc molecule has a TiO_4^{4-} nucleus, a functional group –C=O, and long alkene groups. According to their report, the TiO_4^{4-} nucleus regulates the electrical properties of the SnO_2 layer and the long alkenes act as stabilizer to prevent the accumulation of nanoparticles and electronic glue among SnO_2 nanoparticles and increase its homogeneity and conductivity. The remained –C=O factor groups at the ETL surface also make a strong bond with Pb^{2+} and improve the intimacy interface between ETL and perovskite. Their results demonstrated increase the efficiency of PSCs from 19.00% to 20.4% by using SnO_2: TiAcAc composite as ETL.

Yang and coworkers[213] utilized Ti_3C_2 MXene in LT-SnO_2 ETL to benefit from its metal high conductivity. The results showed that the presence of Ti_3C_2 MXene metal nanosheets in this composite ETL leads to an enhancement in charge extraction and transport, electron mobility increment, and reduced electron transport resistance at the ETL/perovskite interface and thus leads to the increased photocurrent. Therefore, compared with that of the PSCs based on SnO_2 ETL yielding a PCE of 17.23%, the efficiency of PSCs based on SnO_2:Ti_3C_2 composite ETL was elevated to 18.34%. Huang et al.[91] fabricated a composite of SnO_2, MXene, and the anatase phase of TiO_2 QDs through the ad-mixing of MXene to SnO_2 solution and two-step annealing at low temperatures of 150 °C under air and N_2. In the first and second step of annealing under the air and N_2 atmosphere, respectively, SnO_2 and TiO_2 anatase crystals were produced and kept growing. In the subsequent annealing in N_2, a more stable phase and then nanoscale TiO_2/SnO_2 heterojunctions were formed. At last, the 2D MXene sheets performed as conductive bridges bonding these TiO_2/SnO_2 heterojunctions at the edge region of the sheet and constructed the final multidimensional conductive network (MDCN) structure. Also, in comparison of the performance of this composite ETL with that of SnO_2 ETL in the PSC configuration, the presence of 2D MXene as conductive bonded bridges made for an enhancement in electrical conductivity of the layer and the ETL/perovskite interface modification (**Figure 33**b,c). In the case of PCE enhancement, the efficiency of PSCs boosted from 16.83% to 19.14% in consequence

of replacing SnO_2 ETL with SnO_2:MXene-based TiO_2 QDs composite ETL (Figure 33a).[91]

Yang et al.[260] used N, S co-doped MXene QDs to prepare the SnO_2: N, S co-doped MXene QD composite. According to their results, the presence of this composite as ETL led to an increase in the nucleation rate of perovskite crystals during the initial spin-coating process and the formation of an intermediate phase of perovskite after antisolvent treatment, which achieved high quality perovskite crystals during the annealing process. Thus, they succeeded to achieve a PCE of 23.30%. Tao et al.[261] developed an efficient ETL using SnO_2:PMo_{12} composite for printable HTL-free mesoporous PSCs in which PMo_{12} is the representative of Keggin-type polyoxometalate (POM) $H_3PMo_{12}O_{40}$. POMs are a large group of metal-oxo cluster compounds extensively employed in a broad range of applications. Among their outstanding features is their ability to perform as shallow electron traps, effectively segregating the photogenerated excitons thereof and thus enhancing the efficiency and performance of the solar cells. The utilization of SnO_2:PMo_{12} composite ETL making use of the synergistic effect of PMO has resulted in electron mobility enhancement, more expedited electron extraction, and downward shift of the conduction band, which facilitates the injection and transport of electrons from the perovskite to the ETL and desirably diminishes the charge recombination. Therein, the results of this group demonstrated that the PCE of mesoporous PSCs has been raised from 9.8% to 12.6% utilizing the SnO_2:PMo_{12} composite rather than that of the SnO_2 compact layer.[261]

Jung et al.[262] used SnO_2:AlO_6 nanocomposites as ETLs and achieved PCE of 21.04%. By synthesizing amorphous AlO_6 and SnO_2 (SnO_2:AlO_6) nanocomposite films from aluminum chloride hexahydrate precursor, they formed an amorphous AlO_6 octahedra in the amorphous SnO_2 network, which is clearly different from Al-doped crystalline SnO_2. According to their achievements, the SnO_2:AlO_6 nanocomposite increases perovskite grain size, decreases perovskite grain density, stress, and also internal and surface nonradiative recombination. In addition, they reported that the SnO_2:AlO_6 nanocomposite exhibits desirable properties such as high conductivity, fast charge extraction, and excellent recombination resistance. Also, the SnO_2:AlO_6 ETL formed a better energy band alignment with the perovskite band structure with the upward shift of its Fermi level.

SnO_2-Based Complexes: In a different manner to element doping in which the introduced dopant incorporates the crystal lattice, organic molecules could alternatively form a hybrid organic–inorganic complex with the inorganic host materials. When organic molecules are adsorbed on the surface of inorganic nanocrystals, charge transfer might occur from the organic molecules into the inorganic semiconductor without inducing defects within the inorganic lattice matrix. This strategy has been proved to be effective when applying to optoelectronics and energy devices.[263]

Polyethylene glycol (PEG) is one of the organic materials exhibiting a higher tendency compared with those of other polymers, to form complexes with SnO_2. In consequence of using this polymer, a SnO_2 in a polymer matrix is constructed in which PEG molecules are arranged around SnO_2 nanoparticles resembling the ligands and reduce the aggregation of nanoparticles in the ink. Therefore, due to the reduction of agglomeration as well as improvement of the morphology of SnO_2 film, the wettability of the layer is enhanced by the formation of a hydrogen bond of PEG with SnO_2.[264–266] Wei et al.[265] could successfully increase the PCE of planar structured PSC from 19.2% to 20.8% by the utility of SnO_2-PEG ETL instead of SnO_2 ETL. Also, Mathiazhagan et al.[264] investigated several additives including PEG, polyvinyl acetate (PVA), and ethylene glycol (EG), to avoid the agglomeration in the slot-die deposited SnO_2 film and to enable improved wetting in the perovskite solution. Nevertheless, PEG has formed the best film through the slot-die coating and also improved the wettability of the perovskite solution. Hence, they could finally achieve PSCs with a PCE of 10.82% by the substitution of the layer of SnO_2 ETL with that of SnO_2-PEG ETL. In a similar procedure, Wang et al.[267] employed PEG as a pore-forming agent in the colloidal precursor solution of SnO_2 nanoparticles to prepare LT-SnO_2 mesoporous ETL, and thereafter the application of a low-temperature annealing process (≈180 °C), the PEG in the deposited layer was eliminated. According to their results, the PCE of PSCs based on this mesoporous SnO_2 ETL was obtained to be 20.82%.

Vijayaraghavan and coworkers[268] utilized SnO_2 QDs as ETLs to fabricate HTL-free PSCs based on carbon electrodes. They could avoid the SnO_2 QDs aggregation through the addition of thiourea as a reaction accelerator and stabilizer to the SnO_2 precursor solution owing to the QDs surrounded with the amino groups and realized a PCE of 13.64% for PSCs thereof.

Gao et al.[269] synthesized the SnO_2–urea complex by adding urea to the ethanolic $SnCl_4$ solution. The SnO_2–urea complex is obtained by binding the amino group (–NH_2) to SnO_2 via Sn–N chemical bonds. They reported that SnO_2–urea ETLs improved the electrical performance of SnO_2 and passivated the surface trap states of the perovskite film. As a result, they improved the PCE of these PSCs from 17.60% (SnO_2) to 20.25% (SnO_2–urea complex).

To prepare high-quality mesoporous SnO_2 ETL, Song et al.[270] initially synthesized high-aspect-ratio and well-crystallized SnO_2 nanorods (NRs) using oleic acid (OA) ligands via the solvothermal method. Thereafter, the OA-capped SnO_2 NRs are self-assembled into SnO_2 emulsified microspheres (SnO_2 EMs) by the emulsion-based bottom-up self-assembly strategy. Finally, the SnO_2 EMs are used to fabricate mesoporous SnO_2 ETLs at a low temperature and the insulating OA ligands surrounding the surfaces of SnO_2 NRs are in situ stripped by using a $NOBF_4$ solution. The in situ substitution of OA ligands with BF_4^- ligands guarantees effective electron extraction and suppression of dark recombination, which is supported by the better charge carrier dynamics and lower trap-state densities compared with the planar SnO_2 NR and mesoporous OA-capped SnO_2 EM samples. Furthermore, they could manage to boost the PCE from 16.28% to 21.35% by changing the ligand from OA to BF_4-.

To prepare SnO_2 ETL in an inverted PSC structure (FTO/NiO_x/$PC_{61}BM$/SnO_2/Ag), Lee et al.[271] first synthesized SnO_2 nanoparticles by solvothermal method, which were easily aggregated and could not form a well-dispersed suspension in any of the polar or nonpolar solvents. They first prepared OA-capped SnO_2 nanoparticles using oleic acid (OA) ligands that were well dispersed in nonpolar solvents (such as chlorobenzene or chloroform). But the used nonpolar solvent caused damage to the PC61BM layer As a result, they benefited from the alteration of the OA ligand to tetramethylammonium hydroxide

Table 6. Performance and precise PV characteristics of PSCs based on LT-ETLs of Sn-TMOs.

			Cell configuration	J_{SC} [mA cm^{-2}]	V_{OC} [V]	FF [%]	Eff [%]	Ref.
Sn-TMOs	$Sn_xIn_{1-x}O$ (TIO)	Planar	ITO/$Sn_{0.77}In_{0.23}O$/$Cs_{0.05}(FA_{0.87}\ MA_{0.13})_{0.95}$ $Pb(Br_{0.13}I_{0.87})_3$/Spiro-MeOTAD/Au	19.95	1.05	71.00	14.88	[281]
		planar	ITO/$Sn_{0.83}In_{0.17}O$/$Cs_{0.05}(FA_{0.87}\ MA_{0.13})_{0.95}$ $Pb(Br_{0.13}I_{0.87})_3$/Spiro-MeOTAD/Au	19.95	1.05	71.00	15.00	[282]
	$ZrSnO_4$	Planar	ITO/$ZrSnO_4$/$((FAPbI_3)_{0.95}(MAPbBr_3)_{0.05})$/Spiro-MeOTAD/Au	24.75	1.00	67.00	16.76	[279]
	$SrSnO_3$	Planar	FTO/$SrSnO_3$/$FA_{0.85}MA_{0.15}Pb(I_{0.85}Br_{0.15})_3$/Spiro-MeOTAD/Au	22.30	1.13	67.00	16.90	[285]
		planar	FTO/Y:$SrSnO_3$/$FA_{0.85}MA_{0.15}Pb(I_{0.85}Br_{0.15})_3$/Spiro-MeOTAD/Au	22.70	1.14	74.00	19.00	[285]
	Zn_2SnO_4	planar	ITO/Zn_2SnO_4 (NP)/$MAPbI_3$/PTAA/Au	21.60	1.05	67.00	15.30	[43]
		planar	ITO/Zn_2SnO_4 (QD)/$MAPbI_3$/PTAA/Au	21.30	1.03	64.00	14.00	[278]
		planar	ITO/Zn_2SnO_4 (NP)/Zn_2SnO_4 (QD)/$MAPbI_3$/PTAA/Au	21.80	1.06	74.00	17.10	[278]
		planar	ITO/Zn_2SnO_4 (NP)/Zn_2SnO_4 (QD)/$MAPb(I_{0.9}Br_{0.1})_3$/PTAA/Au	21.20	1.11	74.00	17.60	[278]
		Inverted	ITO/NiO_x/$MA_{0.8}FA_{0.2}Pb(I_{0.87}Br_{0.13})_3$/PCBM/$Zn_2SnO_4$/Ag	21.34	1.15	72.30	17.76	[276]
		Planar	ITO/Zn_2SnO_4/PCBM/$MA_{0.8}FA_{0.2}Pb(I_{0.87}Br_{0.13})_3$/Spiro-MeOTAD/Ag	21.08	1.08	65.90	15.01	[276]
		Planar	PEN/ITO/Zn_2SnO_4 (NP)/$MAPbI_3$/PTAA/Au	20.20	1.03	73.68	15.32	[274]
		Mesoporous	PEN/ITO/Zn_2SnO_4 (NP) & SnO_2 (NR)/$MAPbI_3$/PTAA/Au	21.13	1.04	73.95	16.20	[274]
		Mesoporous	PEN/ITO/Zn_2SnO_4 (NC) & SnO_2 (NR)/$MAPbI_3$/PTAA/Au	22.11	1.01	75.53	17.54	[274]
		Planar	FTO/Zn_2SnO_4/$MAPbI_3$/Spiro-MeOTAD/Ag	20.46	1.03	67.00	14.02	[277]
		Planar	FTO/Zn_2SnO_4/$Cs_{0.05}(MA_{0.15}FA_{0.85})_{0.95}Pb$ $(Br_{0.15}I_{0.85})_3$/Spiro-MeOTAD/Au	23.02	1.09	76.00	19.30	[275]
		Mesoporous	FTO/Zn_2SnO_4/Zn_2SnO_4/$Cs_{0.05}(MA_{0.15}FA_{0.85})_{0.95}Pb$ $(Br_{0.15}I_{0.85})_3$/Spiro-MeOTAD/Au	23.60	1.14	79.00	21.30	[275]

[a]Quantum dot: QD, nanoparticle: NP, nanorod: NR, nanocube: NC.

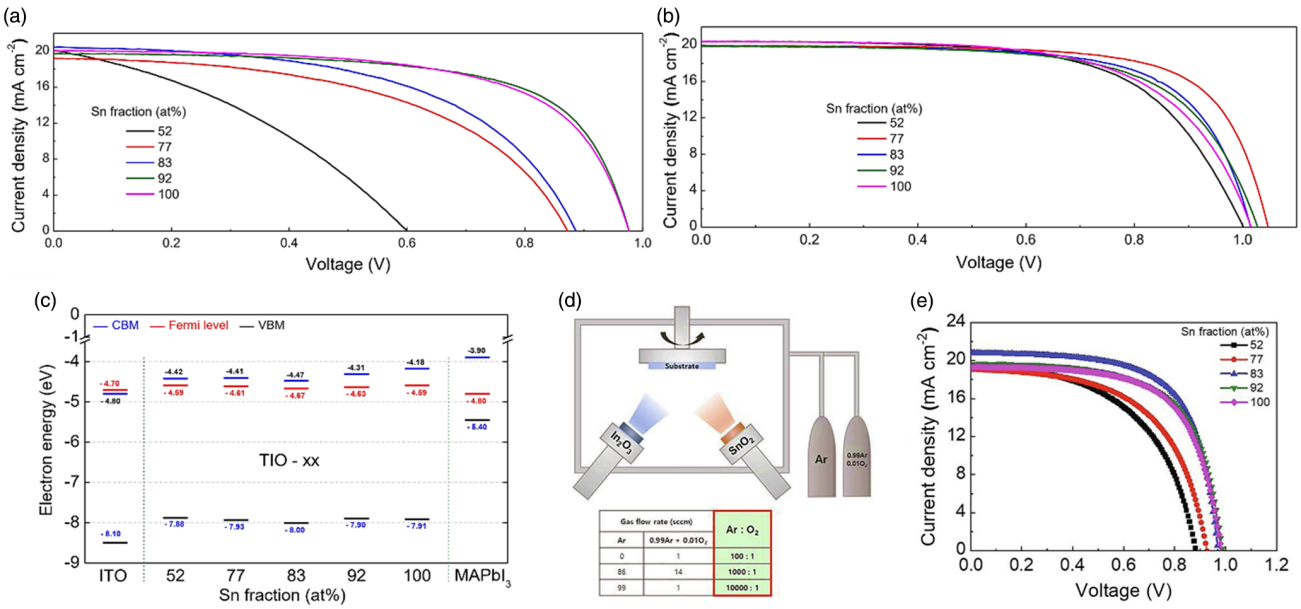

Figure 34. a) *J–V* curves of the TIO ETL-based PSCs with different Sn fractions. b) *J–V* curves of the $TiCl_4$-treated TIO ETL-based PSCs with different Sn fractions. c) Conduction band minimum (CBM), valence band maximum (VBM), and Fermi levels of the TIO films. Reproduced with permission.[281] Copyright 2020, Elsevier. d) Schematic illustration of TIO thin films deposition via magnetron cosputtering, the table showing used Ar:O_2 gas ratio flow rates. e) *J–V* curves of $TiCl_4$-treated TIO films with various Sn fractions at Ar:O_2 = 10 000:1. Reproduced with permission.[282] Copyright 2019, Elsevier.

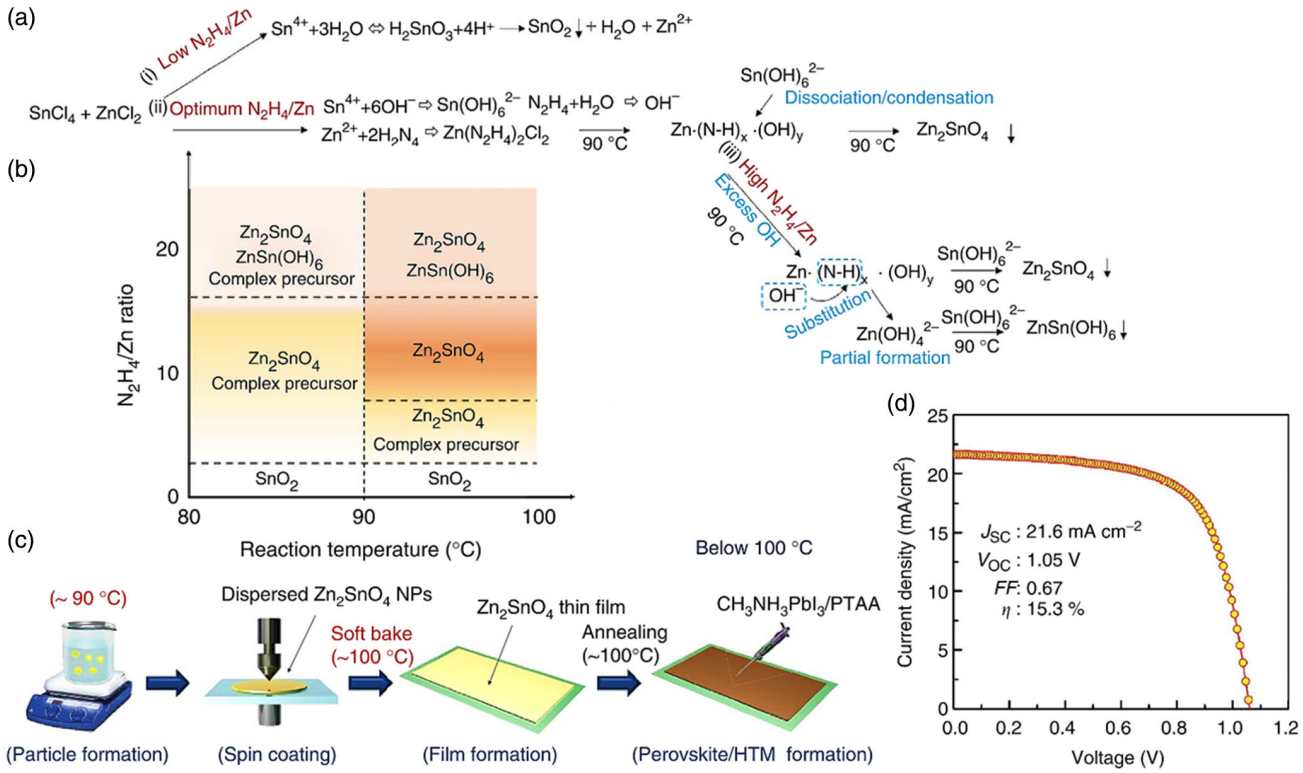

Figure 35. a) Schematic illustration of the formation mechanism of crystalline Zn_2SnO_4 NPs via a low-temperature process below 100 °C. b) Formation map of Zn_2SnO_4 with different temperatures and hydrazine/Zn ratio. c) Schematic illustration of the low-temperature process for fabricating a flexible device with Zn_2SnO_4 NPs. d) *J–V* curve measured by the reverse scan with 10 mV voltage steps and 40 ms delay times under AM 1.5 G illumination. Reproduced with permission under the terms of the Creative Commons CC BY license.[43] Copyright 2015, the Authors. Published by Springer Nature.

pentahydrate (TMAOH) and tetrabutylammonium hydroxide (TBAOH) for performance improvement. The surfactant capability of OA and TBAOH is better than TMAOH due to their higher molecular volume. On the other hand, the work function modifier capability of TMAOH and TBAOH ligands is more suitable than OA due to their larger bipolar momentums. Based on their results, TBAOH performed better as a capping molecule for SnO_2 nanoparticles as both a surfactant and a work function modifier. Thus, using OA, TMAOH, and TBAOH ligands, they improved the efficiency of PSCs from 3.57% to 9.17%, 15.66%, and 18.77%, respectively.

Liu and colleagues[272] used phytic acid (PA) to make the SnO_2–PA complex. PA, as a powerful chemical material consisting of six groups of phosphonic acids, can adhere to the metal surface by complexing between lone electron pair of oxygen in PA with metal ions. The nontoxic PA can use the assembly of coordination complexes between PA and SnO_2 nanocrystals in the form of a new Sn–O–P bond and effectively passivate the inherent dangling bonds in Sn. They reported that the SnO_2–PA complex could significantly separate SnO_2 oligomers and control the cluster size distribution well. It also reduces trap states in SnO_2 surface and makes suitable energy-level alignment in the ETL/perovskite interface. Thus, they succeeded to achieve 21.43% efficiency using SnO_2-PA complex, which is approximately 10.9% higher than the efficiency of pure SnO_2 ETL-based PSCs.

Shi et al.[273] used a supra-molecular complex $[(C_8H_{17})_4N]_4[SiW_{12}O_{40}]$ (TASiW-12) to prepare the SnO_2-TASiW-12 complex and increased the efficiency from 19.70% to 22.84%. They synthesized the n-type TASiW-12 complex using the commercial surfactant tetraoctylammonium bromide (TOAB) and $H_4SiW_{12}O_{40}$. The structure of TASiW-12 is formed by the bonding of four $[(C_8H_{17})_4N]^+$ and one $[SiW_{12}O_{40}]^{4-}$ via electrostatic complexation. Also, each $[(C_8H_{17})_4N]^+$ group can redistribute $[SiW_{12}O_{40}]^{4-}$ by changing its electrostatic interaction. Proton deficiency in TASiW-12 prevents acidic damage of ETL or perovskite. Based on the results of this group, the presence of TASiW-12 has led to the improvement of the ETL bulk and the ETL/perovskite interface.

3.3.3. Sn-Based Ternary Metal Oxides

Ternary metal oxides (TMOs) are another group of oxide semiconductors that have attracted plenty of research interests due to their tunable optical and electronic properties. The majority of TMOs employed in PSCs are prepared at high temperatures which hinders their further development toward low-cost production and practical applications. In recent years, several low-temperature Sn-TMOs such as Zn_2SnO_4,[43,274–278] $ZrSnO_4$,[279] $SrSnO_3$,[232] $Sn_xIn_{1-x}O$ (TIO)[280,281] and their utilities in PSCs as LT-ETLs have been reported. Sn-based TMOs have been examined in PSCs owing to their better electronic

properties along with the transparency and potential chemical stability compared with that of SnO_2. These TMOs possess improved electron mobility, high chemical site densities, and tunable band structures.[282] Aside from PSCs, Sn-TMOs have largely been employed in other solar cell types including dye-sensitized solar cells.[283] The performance and PV characteristics of PSCs based on Sn-TMOs as LT-ETLs are outlined in **Table 6**.

In SnO_2 ETL-based PSCs, Baek et al.[280,281] using sputtering of BaO and In_2O_3, applied a thin layer of amorphous Sn–In–O alloy, i.e., $Sn_xIn_{1-x}O$ (TIO; Sn fraction: >50 atomic percent). By varying the Sn ratio fraction, they observed that with the increase of Sn fraction, the conduction band minimum (CBM) energy level ascended, and thus the distance between the Fermi level and the conduction band increased (**Figure 34**c). As such, the layer resistance is increased because of the electron concentration decline. The bandgap, as well as the transparency of the films, was elevated when Sn increased (Figure 34c). This group initially investigated the different Sn ratios and realized that the most optimal Sn ratio fraction was 92% (Figure 34a). Thereafter, they further improved the performance of the ETL via the addition of $TiCl_4$ treatment in which the optimized Sn ratio was obtained to be 77% at that point and could acquire a PCE of 14.88% (Figure 34b).[280] In another study, the same group monitored the effect of oxygen partial pressure (PO_2) throughout the sputtering of ETL along with $TiCl_4$ treatment and reported a PCE of 15% in which an optimal oxygen atmosphere and the Sn ratio fraction of 83% was acquired (Figure 34d,e).[281]

Noh et al.[279] synthesized the ternary semiconductor composition of Sn-TMO-based ETLs including crystalline $ZrSnO_4$ nanoparticles as the ETL in the structure of PSCs. Due to the propitious optoelectronic properties of $ZrSnO_4$ nanoparticles extending from high transparency, desired energy level, and electron configuration, ETLs based on which have been proposed as promising candidates for optimal electron transfer and diminishing of charge recombination at the perovskite/ETL interface. In this group, an investigation on the structure and optoelectronic properties of $ZrSnO_4$ nanoparticles prepared at three temperatures of 75, 55 °C, and room temperature was conducted. Their results implied that the resultant devices using $ZrSnO_4$ nanoparticles synthesized at room temperature achieved the highest PCE of 16.76%. Guo et al.[232] employed the $SrSnO_3$ ternary composition with the orthorhombic ABO_3 perovskite structure as the ETL in the PSC architecture and could realize a PCE of 16.9%. Furthermore, they could manage to enhance the conductivity and mobility of this structure by yttrium (Y) doping and boosted the efficiency to 19%.

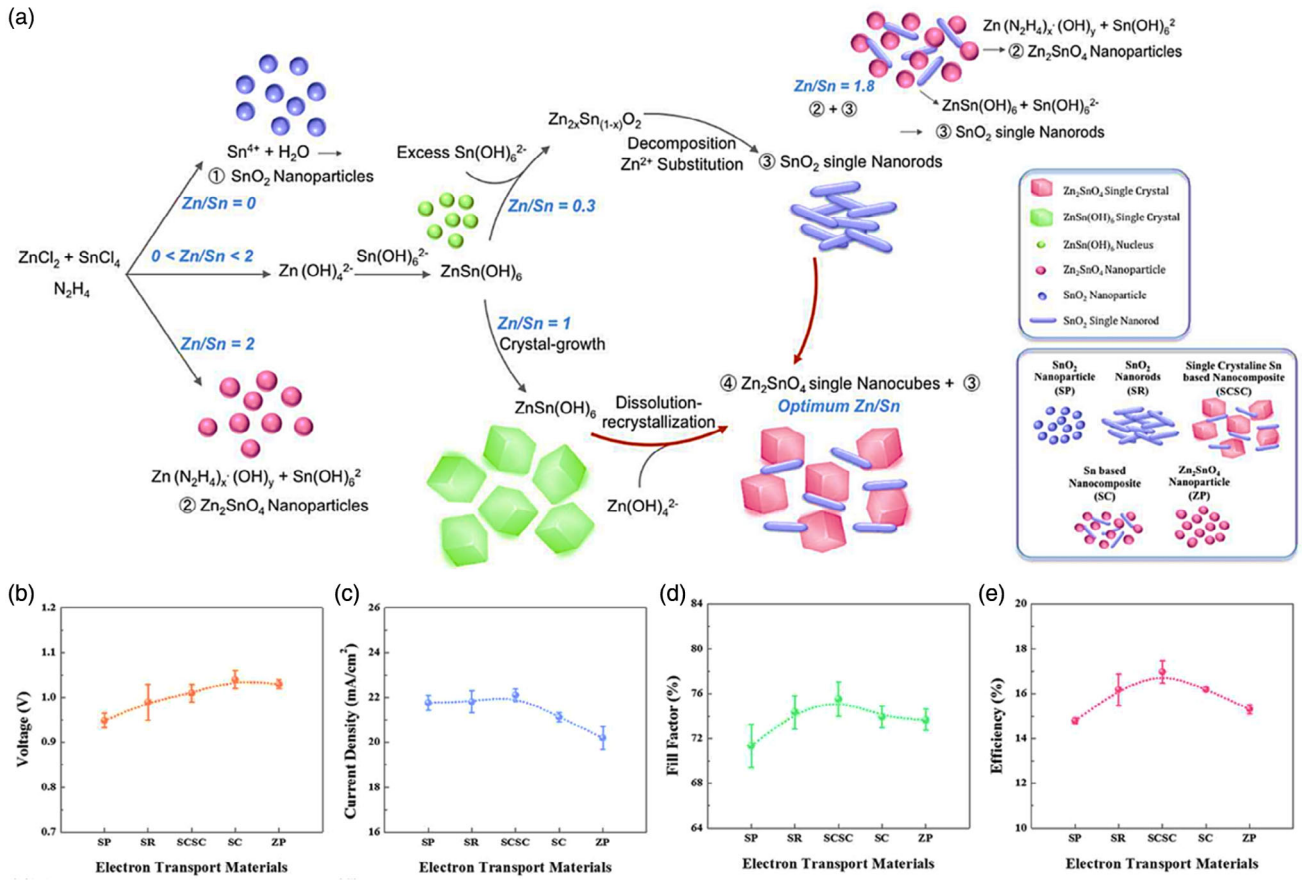

Figure 36. a) Schematic illustration for the formation of the Sn-based oxides as a function of the Zn/Sn ratio. (SP: SnO_2 nanoparticles, SR: SnO_2 nanorods, SCSC: nanocomposite oxides composed of SnO_2 nanorod and Zn_2SnO_4 nanocube, SC: nanocomposite consisting of spherical Zn_2SnO_4 NPs and SnO_2 nanorod, ZP: Zn_2SnO_4 nanoparticles), Average photovoltaic characteristics of five types of ETLs (SP, SR, SCSC, SC, and ZP) on which PSCs are based b) V_{OC}, c) J_{SC}, d) fill factor (*FF*), and e) power conversion efficiency. Reproduced with permission.[274] Copyright 2016, Royal Society of Chemistry.

Among the Sn-TMOs, the Zn_2SnO_4 compound has received the most attention as ETL. This is largely due to the fact that the Zn_2SnO_4 is an n-type ternary semiconductor metal oxide exhibiting analogous similar properties, as the large bandgap ($E_g = 3.8$ eV), with that of the anatase TiO_2 ($E_g = 3.2$ eV). Besides, the electron mobility of this material is 10–30 $cm^2 V^{-1} s^{-1}$. What is more, its charge injection and electron diffusivity are much faster than that of TiO_2-based photoanodes. Notwithstanding, its large bandgap promotes a reduction in photo-bleaching as well as a reduction in the recombination rate of electron-triiodide. Moreover, it exhibits excellent chemical stability against organic solvents and alkaline/acidic solutions.[43,275,284] Nevertheless, the synthesis of Zn_2SnO_4 nanoparticles is quite challenging and requires a relatively high temperature (i.e., over 200 °C) to crystallize since, in comparison with those of binary oxides including SnO_2 and ZnO, both Sn and Zn ions need to be regulated during the reaction.[43] In general, the synthesis temperature of Zn_2SnO_4 is significantly dependent upon the type of Zn precursor complex. Typically, Zn_2SnO_4 nanoparticles are prepared using a strong base such as NaOH through the intermediate phase of $Zn(OH)_6$; however, the conversion of $Zn(OH)_6$ to crystalline Zn_2SnO_4 requires a high reaction temperature (>200 °C). Therefore, several research groups attempted to decrease the reaction temperature by manipulating the Zn complex precursor using amino and/or carbonate-based inorganic materials. Notwithstanding these efforts, high temperature (>150 °C) applied to form the Zn_2SnO_4 nanoparticles of a uniform morphology results in the accumulation, irregular formation, and diverse-sized particles. Nevertheless, Shin and coworkers[43] could manage to obtain Zn_2SnO_4 nanoparticles possessing the uniform morphology at low temperatures (i.e., 90 °C) using the Zn-hydrazine complex precursor (**Figure 35**c). They also investigated various Zn to hydrazine (Zn/N_2H_4) ratios at different temperature ranges. As shown in Figure 35a,b, at low concentrations of hydrazine, the increase of acidity of the reaction medium leads to the formation of SnO_2 nanoparticles. Whereas in high concentrations of hydrazine, the basicity raising of the reaction medium leads to the formation of Zn_2SnO_4 nanoparticles albeit the secondary phase of $ZnSn(OH)_6$ is formed as well. Nonetheless, then again in the optimized ratio of Zn/N_2H_4 and through a mild alkaline medium, the pure phase of Zn_2SnO_4 was obtained. Therein, Shin et al.[43] could achieve a PCE of 15.3% (Figure 35d) via the spin-coating of Zn_2SnO_4 nanoparticles dispersed in 2-methoxy ethanol as ETL on a flexible PEN/ITO substrate. Moreover, in yet another similar study, could realize a PCE of 17.1% employing the multilayer ETL fabricated through the Zn_2SnO_4 nanoparticle deposition on the Zn_2SnO_4 quantum dot layer. Thereafter, by the substitution of the absorbent layer, i.e., $MAPbI_3$ with that of MAPb $(I_{0.9}Br_{0.10})_3$, they could further raise the efficiency to 17.6%.[278]

Liu et al.[276] made use of Zn_2SnO_4 composition with PCBM as a bilayer Zn_2SnO_4/PCBM structure to be utilized as low-temperature ETL in inverted and conventional planar PSCs and achieved the PCEs of 17.76% and 15.01%, respectively. Likewise, Zhang et al.[277] utilized the afore-mentioned compound as a compact ETL in PSC architecture and attained the PCE of 14.02%. Besides, Yeom et al.[274] had employed the same compound as ETL in PSCs with different configurations (i.e., mesoporous and planar) (**Figure 36**a). Initially, they could

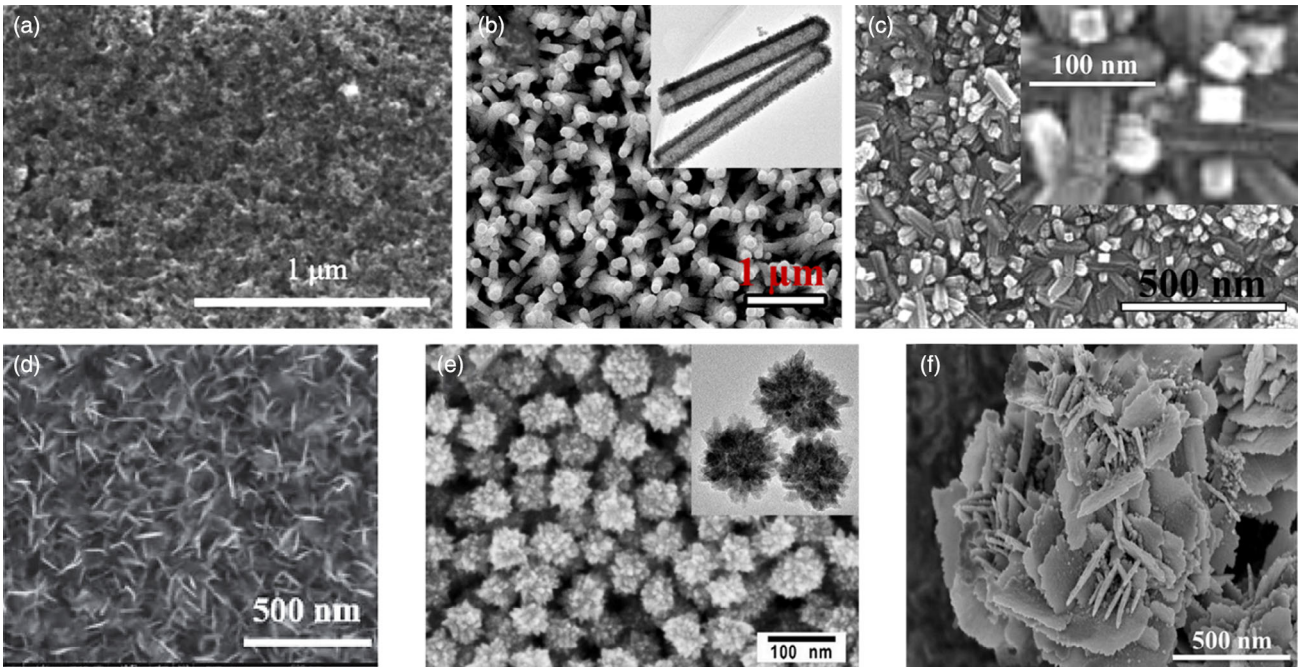

Figure 37. SEM images of different morphologies including a) nanoparticles (Adapted with permission.[267] Copyright 2020, John Wiley and Sons.), b) nanotubes (along with TEM image; Adapted with permission.[287] Copyright 2017, Elsevier.), c) nanorods (with two different magnifications; Adapted with permission.[288] Copyright 2018, Elsevier.), d) nanosheets (Adapted with permission.[66] Copyright 2016, Wiley-VCH.), e) microspheres (along with TEM image; Adapted with permission.[289] Copyright 2020, Elsevier.), and f) nanoflowers Adapted with permission.[169] Copyright 2018, Elsevier.) of mesoporous LT-SnO_2 utilized in PSC architecture.

achieve 14.80% efficiency using SnO_2 nanoparticles (SP) as ETL in planar PSC and then enhanced the PCE to 15.32% through the replacement with alternative Zn_2SnO_4 nanoparticles (ZP). What is more, they could manage to further acquire the PCEs of 16.18% and 16.2% utilizing SnO_2 nanorods (SR) and nanocomposite consisting of spherical Zn_2SnO_4 NPs and SnO_2 nanorods (SC) as mesoporous ETL, respectively. Finally, using nanocomposite oxides composed of SnO_2 nanorod and Zn_2SnO_4 nanocube (SCSC) as mesoporous ETL, they boosted the efficiency of mesoporous PSC up to 17.54% (Figure 36b–e). In a similar way, Sadegh et al.[275] employed Zn_2SnO_4 compact layer as ETL in the architecture of planar PSCs and could realize 19.3% efficiency and further added a mesoporous layer of the same composition to which via CBD method and reported the mesoporous PSCs of certified 21.3% PCE.

4. Various Morphologies of LT-SnO_2 Electron Transporting Layer

In recent years, numerous surveys have been conducted on the morphological monitoring of the layers employed in the fabrication of PSCs, including ETL. In all three planar, mesoporous, and inverted structures, a compact layer of nanoparticles is utilized as ETL. In order to realize high-efficiency PSCs, a thin (i.e., <100 nm) uniform compact layer of n-type semiconductors rendering negligible pinhole and defect is of premier requirement. Variant procedures have been applied to prepare the LT-SnO_2 compact layer mentioned in the previous sections. In essence, compact ETL functions as a part of the window layer in the planar and mesoporous structures which its morphology poses a significant impact upon the optical properties of this layer. Moreover, since the deposition of the perovskite layer is normally carried out in the planar structure, the morphology of the compact ETL affects the formation and quality of the perovskite layer. Heretofore, the highest certified PCEs for planar and inverted PSCs based on LT-SnO_2 compact layer as ETL have been reported to be 25.5%[246] and 18.8%,[51] respectively.

In mesoporous PSCs, an n-type semiconductor mesoporous layer is also deposited on the compact layer serving as a scaffold for perovskite infiltration and promoting the perovskite nucleation and crystallization. The presence of the mesoporous layer provides an enhancement in the interfacial contact area between the perovskite and ETL, which facilitates the extraction, transport, and collection of carriers. In general, mesoporous PSCs demonstrate superior photovoltaic performance over their planar counterparts. However, mesoporous ETLs, especially those prepared with metal oxide nanocrystals (e.g., SnO_2), often require a high-temperature annealing process (> 200 °C) for a more perfect crystallization. Recently, mesoporous LT-SnO_2-based PSCs (<200 °C) of different morphologies including nanoparticles,[267] nanotubes,[285] nanorods,[98,286] nanosheets,[66,219] microspheres,[287] and nanoflowers[169] have been reported (**Figure 37**a–f). Wang and coworkers[267] utilized PEG as a pore-forming agent to prepare the mesoporous LT-SnO_2 ETL nanoporous, and therein they could achieve PSCs having a PCE of 20.82%.

In mesoporous PSCs, electron transport from perovskite to ETL is of paramount importance for cell performance. Electron transfer from perovskite to ETLs based on mesoporous nanoparticles is not desirable due to some deficiencies including numerous grain boundaries, surface defects, and trap states within the random nanoparticulate network in these ETLs. One-dimensional (1D) nanostructures, including nanowires and nanotubes, owing to their high aspect ratio, could enable the provision of highly efficient transport channels for injected electrons and increase light harvesting through light scattering. Besides, 1D nanostructures possess lower grain boundaries that could diminish the number of dead ends.[86,87] Gao et al.[285] enabled the growth of ZnO nanoparticles on the FTO through a seed-assisted approach. Then, the direct growth of SnO_2 nanotubes was achieved based on the dissolution of ZnO nanoparticles during the hydrothermal synthesis process of the SnO_2 shell by means of the alkaline environment. Consequently, using SnO_2 nanotubes as ETL. The utilization of SnO_2 nanorods as ETLs in LT-PSCs was also reported by Zhang et al.[286] They fabricated SnO_2 nanorod arrays using solution-based synthesis method in the presence of hydrochloric acid and employing a thin compact SnO_2 as seed. In a modified manner, Xu et al.[98] employed SnO_2 nanorods as ETL in the PSC structure. They synthesized high aspect ratio crystalline SnO_2 nanorods via the hydrothermal method employing oleic acid (OA) ligands. Thereafter, OA-coated SnO_2 nanorods were applied at once to prepare ETL in PSCs free of a compact ETL and could ascertain the efficiency of 18.62%.

Two-dimensional (2D) nanostructures, i.e., nanosheets, possess a high surface area as well as outstanding electrical properties. Vertical SnO_2 nanosheets with exposed high energy facets have improved the light absorption and facilitated charge extraction owing to the favorable attachment of the light absorbers to the nanosheet surface due to the higher ionic charge of the exposed facets.[66,86,87,219] Liu et al.[66] employed a SnO_2 compact layer along with a mesoporous layer of SnO_2 nanosheets as ETL in PSC architecture prepared through the hydrothermal method. In a similar vein, Yang et al.[219] have synthesized SnO_2 nanosheets using the same hydrothermal method, and they could boost the efficiency further to 17.29% by doping yttrium in SnO_2 nanosheets.

The 1D and/or 2D array structures could be engineered into arrays of 3D structures. The 3D array architectures exhibit several advantages in terms of higher surface area and porosity for efficient perovskite infiltration, superior light scattering for enhanced light harvesting, as well as a 3D interconnected network for enhanced electron transport, suppressed charge recombination, and thus efficient charge collection.[87] Fan et al.[287] synthesized mono-dispersed SnO_2 microspheres through the solvothermal method and utilized them as mesoporous ETL. The formation of SnO_2 nanoflowers consisting of SnO_2 nanosheets directly on the FTO substrate was also met by Mahmoud et al.[169] through a single-step electro-spray method.

5. Scalability of LT-SnO_2 Electron Transporting Layer

Large area deposition of perovskite solar cells has become an important and widespread topic of interest in the field that simultaneously brought new challenges toward fabrication of highly

stable and efficient perovskite solar modules. As discussed in this work, utilization of low-temperature ETL could facilitate scalability of perovskite solar cell technology by offering low-temperature (below 150 °C) processability of the perovskite solar module. However, it requires to be relatively fast, reliable, and reproducible process. ETL is an ultrathin layer (usually <50 nm) and conformal deposition of such ultrathin layers is one of the main challenges that impact directly the reproducibly of the solar cells. Pinholes and cracks in the ETL layer result in direct contact of the perovskite layer with the TCO electrode, leading to charge carrier recombination that subsequently diminish the performance of the solar cell. In addition to morphology, the ETL layers should be optimized in terms of electrical properties and surface chemistry. While many enhancement strategies for LT-ETL made in the recent publications and reviewed in this paper have been developed for lab-scale PSCs, for large-scale deposition more developments would be required to fulfill the to address the abovementioned challenges. The scalable coating methods such as slot-die coating, bar coating, blade coating, spray-coating, and screen printing have been used for the modules based on SnO_2 ETL.[288,289] Fabrication of a stable and highly efficient module based on LT-SnO_2 layer requires to optimize both large area deposition of conformal homogenous ultrathin LT-SnO_2 and interfaces between ETL and the perovskite absorber layer.

6. Outlook and Conclusion

LT-SnO_2 layer has been deposited in numerous ways. While many research groups use solution processing methods such as spin-coating or CBD, other methods including ink printing and sputtering are more appropriate for a large-scale deposition. The deposited layer is required to be uniform and pinhole free, with perfect coverage and proper surface chemistry. Many of deposition methods fail to produce optimized surface chemistry. The functional groups on the surface of SnO_2 define the wetting properties and nucleation/growth quality of the perovskite layer. For this reason, surface treatment is usually required to have low defect density at SnO_2/perovskite interface. UV ozone or oxygen plasma treatments are frequently used to atomically clean the surface, while chemical treatments add particular functional groups on the surface. Other modifications on LT-SnO_2 layers include doping of SnO_2, multilayers, or composite layers. These changes in the ETL chemical nature usually modulate the electrical properties of the ETL, such as conductivity and conduction band offset. Optical properties and surface chemistry could also be controlled by these modifications.

In summary, SnO_2 exhibits the remarkable advantage of being able to achieve high-efficiency PSC (>25%) at low temperature. And the requirement of low-temperature production is parallel with the trend of large-scale commercial manufacture. LT-SnO_2 layer can be deposited in numerous ways from lab to industry. Even though many research groups can use solution processing methods such as spin-coating or CBD to achieve high efficiency with limited sizes, it is still challenging for these methods to prepare uniform, pinhole-free LT-SnO_2 films on huge substrates. Other methods including slot-die, blade-coating, ink printing, and sputtering are more appropriate for large-scale deposition, which are compatible with R2R technology, as well as some other automatic production technologies. In addition, the energy consumption, reproducibility, material cost, and material utilization rate of LT-SnO_2 are crucial for the manufacture of scalable PSC. However, none of them plays a dominant role in the development of large-area PSC modules. More efforts should be put to develop the feasible deposition methods for scaling-up and put the lab-scale PSC toward commercialization.

Furthermore, it is essential for LT-SnO_2 to undertake the modification, so as to promote the carrier transport, minimize the energy loss, and achieve high PCE. Element doping and other functional additives can change the electrical properties for the bulk SnO_2, such as conductivity and conduction band offset. The surface treatment on ETL/perovskite interface also plays a major role in enhancing the carrier extraction and transport and reducing unwanted recombination. It is obvious that the nucleation and growth of perovskite films are hardly affected the interface condition, which can simultaneously passivate the defects both in LT-SnO_2 and perovskite films, together with the improvement of interactions. The successful achievement of 25.2% and 25.5% PCE shows enormous support for the modification strategies of bulk LT-SnO_2 and ETL/perovskite interface. Thus, it can be supposed that if the combination of modification methods is applied for upscaling LT-SnO_2, it may cause multiple enhancement for the devices. It is worth noting that most of the current surface treatment are carried on the small-scale with common used spin-coating methods. When the devices are amplified, physical treatment like UVO treatment or thermal annealing seems to be applicable at this point. Serviceability of chemical treatment strategies deserves suspicion. In this aspect, additives may work more efficient since they are usually mixed together with tin source materials and will not be restricted with the operating techniques. Overall, choosing proper components as tin source, using quick and easy-operating deposition techniques, and modifying the surface properties will be the key route to obtain high-quality LT-SnO_2 for large-area PSCs.

Acknowledgements

M.H. and N.G. contributed equally to this work. M.A.-J. acknowledges the Royal Society (RGS\R1\211068), Cambridge Materials Limited, and Wolfson College, University of Cambridge for their funding and technical support. M.A.-J. acknowledges the ACT programme (Accelerating CCS Technologies, Horizon2020 Project No. 691712) and Department for Business, Energy and Industrial Strategy for the financial support of the NEXTCCUS project (project ID: 327327). M.A.-J. and H.L. acknowledge UCL Research, Innovation & Global Engagement, Cornell-UCL Global Strategic Collaboration Awards team for their financial Support. H.L. is grateful for the support from the Chinese Scholarship Council (CSC) and the Faculty of Mathematical & Physical Sciences (MAPS) at University College London (UCL). N.Gh. acknowledges the Iran's National Science Elite's federation (ISEF) for postdoctoral research grant.

Conflict of Interest

The authors declare no conflict of interest.

Keywords

electron transport layers, low temperature, perovskite solar cells, SnO_2

Received: December 3, 2022
Revised: January 25, 2023
Published online: March 9, 2023

[1] A. Kojima, K. Teshima, Y. Shirai, T. Miyasaka, *J. Am. Chem. Soc.* **2009**, *131*, 6050.
[2] National Renewable Energy Laboratory, Best Research Cell Efficiencies, https://www.nrel.gov/pv/cell-efficiency.html, (accessed: January 2023).
[3] T. Ibn-Mohammed, S. C. L. Koh, I. M. Reaney, A. Acquaye, G. Schileo, K. B. Mustapha, R. Greenough, *Renew. Sustain. Energy Rev.* **2017**, *80*, 1321.
[4] A. Polman, M. Knight, E. C. Garnett, B. Ehrler, W. C. Sinke, *Science* **2016**, *352*, aad4424.
[5] G. Yang, H. Tao, P. Qin, W. Ke, G. Fang, *J. Mater. Chem. A* **2016**, *4*, 3970.
[6] K. Mahmood, S. Sarwar, M. T. Mehran, *RSC Adv.* **2017**, *7*, 17044.
[7] D. N. Feria, C. W. Chao, K. P. O. Mahesh, C. L. Hsu, Y. C. Chao, *Synth. Met.* **2020**, *267*, 116443.
[8] W. Huang, T. Bu, F. Huang, Y. B. Cheng, *Joule* **2020**, *4*, 975.
[9] P. Vivo, J. K. Salunke, A. Priimagi, *Materials* **2017**, *10*, https://doi.org/10.3390/ma10091087.
[10] I. Hussain, H. P. Tran, J. Jaksik, J. Moore, N. Islam, M. J. Uddin, *Emergent Mater.* **2018**, *1*, 133.
[11] P. You, G. Li, G. Tang, J. Cao, F. Yan, *Energy Environ. Sci.* **2020**, *13*, 1187.
[12] B. J. Huang, C. K. Guan, S. H. Huang, W. F. Su, *Sol. Energy* **2020**, *205*, 192.
[13] Y. F. Makableh, I. Abu Awad, W. Hassan, G. Aljaiuossi, *Sol. Energy* **2020**, *202*, 204.
[14] F. De Rossi, J. A. Baker, D. Beynon, K. E. A. Hooper, S. M. P. Meroni, D. Williams, Z. Wei, A. Yasin, C. Charbonneau, E. H. Jewell, T. M. Watson, *Adv. Mater. Technol.* **2018**, *3*, https://doi.org/10.1002/admt.201800156.
[15] N. Kumar, H. B. Lee, S. Hwang, J. W. Kang, *J. Mater. Chem. A* **2020**, *8*, 3357.
[16] N. G. Park, K. Zhu, *Nat. Rev. Mater.* **2020**, *5*, 333.
[17] J. Chen, N. G. Park, *ACS Energy Lett.* **2020**, *5*, 2742.
[18] X. Dai, K. Xu, F. Wei, *Beilstein J. Nanotechnol.* **2020**, *11*, 51.
[19] M. Mujahid, C. Chen, W. Hu, Z. K. Wang, Y. Duan, *Sol. RRL* **2020**, *4*, 1.
[20] A. Pang, J. Li, X.-F. Wei, Z.-W. Ruan, M. Yang, Z.-N. Chen, *Nanoscale Adv.* **2020**, *2*, 4062.
[21] Q. Wali, F. J. Iftikhar, N. K. Elumalai, Y. Iqbal, S. Yousaf, S. Iqbal, R. Jose, *Curr. Appl. Phys.* **2020**, *20*, 720.
[22] V. Babu, R. F. Pineda, T. Ahmad, A. O. Alvarez, L. A. Castriotta, A. Di Carlo, F. Fabregat-Santiago, K. Wojciechowski, *ACS Appl. Energy Mater.* **2020**, *3*, 5126.
[23] F. Di Giacomo, A. Fakharuddin, R. Jose, T. M. Brown, *Energy Environ. Sci.* **2016**, *9*, 3007.
[24] T. Bu, S. Shi, J. Li, Y. Liu, J. Shi, L. Chen, X. Liu, J. Qiu, Z. Ku, Y. Peng, J. Zhong, Y. B. Cheng, F. Huang, *ACS Appl. Mater. Interfaces* **2018**, *10*, 14922.
[25] A. S. Subbiah, N. Mathews, S. Mhaisalkar, S. K. Sarkar, *ACS Energy Lett.* **2018**, *3*, 1482.
[26] T. Bu, J. Li, F. Zheng, W. Chen, X. Wen, Z. Ku, Y. Peng, J. Zhong, Y. B. Cheng, F. Huang, *Nat. Commun.* **2018**, *9*, https://doi.org/10.1038/s41467-018-07099-9.
[27] M. Park, J.-Y. Kim, H. J. Son, C.-H. Lee, S. S. Jang, M. J. Ko, *Nano Energy* **2016**, *26*, 208.
[28] M. Kam, Q. Zhang, D. Zhang, Z. Fan, *Sci. Rep.* **2019**, *9*, https://doi.org/10.1038/s41598-019-42962-9.
[29] G. Yang, C. Chen, F. Yao, Z. Chen, Q. Zhang, X. Zheng, J. Ma, H. Lei, P. Qin, L. Xiong, W. Ke, G. Li, Y. Yan, G. Fang, *Adv. Mater.* **2018**, *30*, https://doi.org/10.1002/adma.201706023.
[30] T. Singh, J. Singh, T. Miyasaka, *ChemSusChem* **2016**, *9*, 2559.
[31] R. Mohammadpour, A. Irajizad, A. Hagfeldt, G. Boschloo, *ChemPhysChem* **2010**, *11*, 2140.
[32] A. J. Yun, J. Kim, T. Hwang, B. Park, *ACS Appl. Energy Mater.* **2019**, *2*, 3554.
[33] R. Mohammadpour, *J. Phys. D. Appl. Phys.* **2017**, *50*, 505106.
[34] J. Du, L. Feng, X. Guo, X. Huang, Z. Lin, J. Su, Z. Hu, J. Zhang, J. Chang, Y. Hao, *J. Power Sources* **2020**, *455*, 227974.
[35] Q. Jiang, Z. Chu, P. Wang, X. Yang, H. Liu, Y. Wang, Z. Yin, J. Wu, X. Zhang, J. You, *Adv. Mater.* **2017**, *29*, https://doi.org/10.1002/adma.201703852.
[36] X. Kong, Y. Jiang, Z. Li, Y. Zhou, Z. Xu, C. Cong, X. Gao, X. Lu, G. Zhou, J. M. Liu, K. Kempa, J. Gao, *Sol. RRL* **2021**, *5*, https://doi.org/10.1002/solr.202000646.
[37] Z. Yu, Z. Yang, Z. Ni, Y. Shao, B. Chen, Y. Lin, H. Wei, Z. J. Yu, Z. Holman, J. Huang, *Nat. Energy* **2020**, *5*, 657.
[38] L. Qiu, Z. Liu, L. K. Ono, Y. Jiang, D. Y. Son, Z. Hawash, S. He, Y. Qi, *Adv. Funct. Mater.* **2019**, *29*, https://doi.org/10.1002/adfm.201806779.
[39] M. Zhu, W. Liu, W. Ke, S. Clark, E. B. Secor, T. Bin Song, M. G. Kanatzidis, X. Li, M. C. Hersam, *J. Mater. Chem. A* **2017**, *5*, 24110.
[40] H. Ye, Z. Liu, X. Liu, B. Sun, X. Tan, Y. Tu, T. Shi, Z. Tang, G. Liao, *Appl. Surf. Sci.* **2019**, *478*, 417.
[41] Z. Xu, S. H. Teo, L. Gao, Z. Guo, Y. Kamata, S. Hayase, T. Ma, *Org. Electron.* **2019**, *73*, 62.
[42] C. Wang, C. Zhang, S. Wang, G. Liu, H. Xia, S. Tong, J. He, D. Niu, C. Zhou, K. Ding, Y. Gao, J. Yang, *Sol. RRL* **2018**, *2*, 1700209.
[43] S. S. Shin, W. S. Yang, J. H. Noh, J. H. Suk, N. J. Jeon, J. H. Park, J. S. Kim, W. M. Seong, S. Il Seok, *Nat. Commun.* **2015**, *6*, https://doi.org/10.1038/ncomms8410.
[44] Z. W. Chen, J. K. L. Lai, C. H. Shek, *Phys. Lett. Sect. A Gen. At. Solid State Phys.* **2005**, *345*, 218.
[45] A. R. Maddalena, A. R. Dal Maschio, S. Dire, *J. Non. Cryst. Solids* **1990**, *121*, 365.
[46] E. Calabrò, F. Matteocci, A. L. Palma, L. Vesce, B. Taheri, L. Carlini, I. Pis, S. Nappini, J. Dagar, C. Battocchio, T. M. Brown, A. Di Carlo, *Sol. Energy Mater. Sol. Cells* **2018**, *185*, 136.
[47] G. Murugadoss, H. Kanda, S. Tanaka, H. Nishino, S. Ito, H. Imahoric, T. Umeyama, *J. Power Sources* **2016**, *307*, 891.
[48] Q. Dong, J. Li, Y. Shi, M. Chen, L. K. Ono, K. Zhou, C. Zhang, Y. Qi, Y. Zhou, N. P. Padture, L. Wang, *Adv. Energy Mater.* **2019**, *1900834*, 1900834.
[49] Q. Dong, Y. Shi, C. Zhang, Y. Wu, L. Wang, *Nano Energy* **2017**, *40*, 336.
[50] Y. Qiang, J. Cheng, Y. Qi, H. Shi, H. Liu, C. Geng, Y. Xie, *J. Alloys Compd.* **2019**, *809*, 151817.
[51] Z. Zhu, Y. Bai, X. Liu, C. C. Chueh, S. Yang, A. K. Y. Jen, *Adv. Mater.* **2016**, *28*, 6478.
[52] M. Abulikemu, M. Neophytou, J. M. Barbé, M. L. Tietze, A. El Labban, D. H. Anjum, A. Amassian, I. McCulloch, S. Del Gobbo, *J. Mater. Chem. A* **2017**, *5*, 7759.
[53] M. Singh, A. Ng, Z. Ren, H. Hu, H. C. Lin, C. W. Chu, G. Li, *Nano Energy* **2019**, *60*, 275.
[54] Q. Jiang, L. Zhang, H. Wang, X. Yang, J. Meng, H. Liu, Z. Yin, J. Wu, X. Zhang, J. You, *Nat. Energy* **2017**, *2*, https://doi.org/10.1038/nenergy.2016.177.
[55] C. Xu, Z. Liu, Q. Sun, E. C. Lee, *Sol. Energy* **2021**, *214*, 280.

[56] H. Wang, H. Liu, F. Ye, Z. Chen, J. Ma, J. Liang, X. Zheng, C. Tao, G. Fang, *J. Power Sources* **2021**, *481*, 229160.
[57] Z. Xu, Y. Jiang, Z. Li, C. Chen, X. Kong, Y. Chen, G. Zhou, J. M. Liu, K. Kempa, J. Gao, *ACS Appl. Energy Mater.* **2021**, *4*, 1887.
[58] J. Barbé, M. L. Tietze, M. Neophytou, B. Murali, E. Alarousu, A. El Labban, M. Abulikemu, W. Yue, O. F. Mohammed, I. McCulloch, A. Amassian, S. Del Gobbo, *ACS Appl. Mater. Interfaces* **2017**, *9*, 11828.
[59] E. H. Anaraki, A. Kermanpur, L. Steier, K. Domanski, T. Matsui, W. Tress, M. Saliba, A. Abate, M. Grätzel, A. Hagfeldt, J. P. Correa-Baena, *Energy Environ. Sci.* **2016**, *9*, 3128.
[60] Y. Ko, Y. Kim, C. Lee, T. Kim, S. Kim, Y. J. Yun, H. J. Gwon, N. H. Lee, Y. Jun, *ChemSusChem* **2020**, *13*, 4051.
[61] J. Y. Lam, J. Y. Chen, P. C. Tsai, Y. T. Hsieh, C. C. Chueh, S. H. Tung, W. C. Chen, *RSC Adv.* **2017**, *7*, 54361.
[62] J. Y. Chen, C. C. Chueh, Z. Zhu, W. C. Chen, A. K. Y. Jen, *Sol. Energy Mater. Sol. Cells* **2017**, *164*, 47.
[63] X. Liu, K. W. Tsai, Z. Zhu, Y. Sun, C. C. Chueh, A. K. Y. Jen, *Adv. Mater. Interfaces* **2016**, *3*, https://doi.org/10.1002/admi.201600122.
[64] Y. Wang, L. Yang, C. Dall'Agnese, G. Chen, A.-J. Li, X.-F. Wang, *Front. Chem. Sci. Eng.* **2021**, *15*, 180.
[65] B. Taheri, E. Calabrò, F. Matteocci, D. Di Girolamo, G. Cardone, A. Liscio, A. Di Carlo, F. Brunetti, *Energy Technol.* **2020**, *8*, https://doi.org/10.1002/ente.201901284.
[66] Q. Liu, M. C. Qin, W. J. Ke, X. L. Zheng, Z. Chen, P. L. Qin, L. Bin Xiong, H. W. Lei, J. W. Wan, J. Wen, G. Yang, J. J. Ma, Z. Y. Zhang, G. J. Fang, *Adv. Funct. Mater.* **2016**, *26*, 6069.
[67] C. Gong, S. Tong, K. Huang, H. Li, H. Huang, J. Zhang, J. Yang, *Sol. RRL* **2020**, *4*, https://doi.org/10.1002/solr.201900204.
[68] Y. Kuang, V. Zardetto, R. Van Gils, S. Karwal, D. Koushik, M. A. Verheijen, L. E. Black, C. Weijtens, S. Veenstra, R. Andriessen, W. M. M. Kessels, M. Creatore, *ACS Appl. Mater. Interfaces* **2018**, *10*, 30367.
[69] Y. Lee, S. Lee, G. Seo, S. Paek, K. T. Cho, A. J. Huckaba, M. Calizzi, D. Won Choi, J. S. Park, D. Lee, H. J. Lee, A. M. Asiri, M. K. Nazeeruddin, *Adv. Sci.* **2018**, *5*, https://doi.org/10.1002/advs.20180013.
[70] C. Wang, D. Zhao, C. R. Grice, W. Liao, Y. Yu, A. Cimaroli, N. Shrestha, P. J. Roland, J. Chen, Z. Yu, P. Liu, N. Cheng, R. J. Ellingson, X. Zhao, Y. Yan, *J. Mater. Chem. A* **2016**, *4*, 12080.
[71] M. N. R. Ashfold, F. Claeyssens, G. M. Fuge, S. J. Henley, *Chem. Soc. Rev.* **2004**, *33*, 23.
[72] X. Song, X. Ji, M. Li, W. Lin, X. Luo, H. Zhang, *Int. J. Photoenergy* **2014**, *2014*, https://doi.org/10.1155/2014/613173.
[73] P. Willmott, J. Huber, *Rev. Mod. Phys.* **2000**, *72*, 315.
[74] H. Krebs, M. Weisheit, S. Erik, T. Scharf, C. Fuhse, M. St, K. Sturm, M. Seibt, H. Kijewski, D. Nelke, E. Panchenko, M. Buback, *Adv. Solid State Phys.***2003**, *36*, 505.
[75] Z. Chen, G. Yang, X. Zheng, H. Lei, C. Chen, J. Ma, H. Wang, G. Fang, *J. Power Sources* **2017**, *351*, 123.
[76] Z. Song, W. Bi, X. Zhuang, Y. Wu, B. Zhang, X. Chen, C. Chen, Q. Dai, H. Song, *Sol. RRL* **2020**, *4*, https://doi.org/10.1002/solr.201900266.
[77] J. Ma, X. Zheng, H. Lei, W. Ke, C. Chen, Z. Chen, G. Yang, G. Fang, *Sol. RRL* **2017**, *1*, 1700118.
[78] G. Bai, Z. Wu, J. Li, T. Bu, W. Li, W. Li, F. Huang, Q. Zhang, Y. B. Cheng, J. Zhong, *Sol. Energy* **2019**, *183*, 306.
[79] M. F. Mohamad Noh, N. A. Arzaee, J. Safaei, N. A. Mohamed, H. P. Kim, A. R. Mohd Yusoff, J. Jang, M. A. Mat Teridi, *J. Alloys Compd.* **2019**, *773*, 997.
[80] M. F. M. Noh, M. F. Soh, C. H. Teh, E. L. Lim, C. C. Yap, M. A. Ibrahim, N. A. Ludin, M. A. M. Teridi, *Sol. Energy* **2017**, *158*, 474.
[81] S. Sonmezoglu, S. Akin, *Nano Energy* **2020**, *76*, 105127.
[82] Z. Liu, B. Sun, X. Liu, J. Han, H. Ye, Y. Tu, C. Chen, T. Shi, Z. Tang, G. Liao, *J. Mater. Chem. A* **2018**, *6*, 7409.
[83] X. Zhao, S. Liu, H. Zhang, S. Y. Chang, W. Huang, B. Zhu, Y. Shen, C. Shen, D. Wang, Y. Yang, M. Wang, *Adv. Funct. Mater.* **2019**, *29*, https://doi.org/10.1002/adfm.201805168.
[84] N. Li, J. Yan, Y. Ai, E. Jiang, L. Lin, C. Shou, B. Yan, J. Sheng, J. Ye, *Sci. China Mater.* **2019**, https://doi.org/10.1007/s40843-019-9586-x.
[85] G. Martínez-Denegri, S. Colodrero, M. Kramarenko, J. Martorell, *ACS Appl. Energy Mater.* **2018**, *1*, 5548.
[86] Y. Chen, Q. Meng, L. Zhang, C. Han, H. Gao, Y. Zhang, H. Yan, *J. Energy Chem.* **2019**, *35*, 144.
[87] W. Q. Wu, D. Chen, R. A. Caruso, Y. B. Cheng, *J. Mater. Chem. A* **2017**, *5*, 10092.
[88] Q. Jiang, X. Zhang, J. You, *Small* **2018**, *14*, https://doi.org/10.1002/smll.201801154.
[89] E. Jiang, J. Yan, Y. Ai, N. Li, B. Yan, Y. Zeng, J. Sheng, J. Ye, *Mater. Today Energy* **2019**, *12*, 389.
[90] E. Wang, P. Chen, X. Yin, Y. Wu, W. Que, *Org. Electron.* **2020**, *84*, 105751.
[91] L. Huang, X. Zhou, R. Xue, P. Xu, S. Wang, C. Xu, W. Zeng, Y. Xiong, H. Sang, D. Liang, *Nano-Micro Lett.* **2020**, *12*, https://doi.org/10.1007/s40820-020-0379-5.
[92] H. Huang, X. Liu, M. Duan, J. Ji, H. Jiang, B. Liu, S. Sajid, P. Cui, D. Wei, Y. Li, M. Li, *ACS Appl. Energy Mater.* **2020**, *3*, 5039.
[93] J. A. Smith, O. S. Game, J. E. Bishop, E. L. K. Spooner, R. C. Kilbride, C. Greenland, R. Jayaprakash, T. I. Alanazi, T. I. Alanazi, E. J. Cassella, A. Tejada, A. Tejada, G. Chistiakova, M. Wong-Stringer, T. J. Routledge, A. J. Parnell, D. B. Hammond, D. G. Lidzey, *ACS Appl. Energy Mater.* **2020**, *3*, 5552.
[94] H. Liu, Z. Chen, H. Wang, F. Ye, J. Ma, X. Zheng, P. Gui, L. Xiong, J. Wen, G. Fang, *J. Mater. Chem. A* **2019**, *7*, 10636.
[95] L. Huang, X. Sun, C. Li, J. Xu, R. Xu, Y. Du, J. Ni, H. Cai, J. Li, Z. Hu, J. Zhang, *ACS Appl. Mater. Interfaces* **2017**, *9*, 21909.
[96] F. Li, M. Xu, X. Ma, L. Shen, L. Zhu, Y. Weng, G. Yue, F. Tan, C. Chen, *Nanoscale Res. Lett.* **2018**, *13*, https://doi.org/10.1186/s11671-018-2633-z.
[97] W. Ke, G. Fang, Q. Liu, L. Xiong, P. Qin, H. Tao, J. Wang, H. Lei, B. Li, J. Wan, G. Yang, Y. Yan, *J. Am. Chem. Soc.* **2015**, *137*, 6730.
[98] X. Xu, Z. Xu, J. Tang, X. Zhang, L. Zhang, J. Wu, Z. Lan, *Chem. Eng. J.* **2018**, *351*, 391.
[99] J. Wan, L. Tao, Q. Wang, K. Zhang, J. Xie, J. Zhang, H. Wang, *Chem. Eng. J.* **2021**, *403*, 126435.
[100] S. Cao, H. Wang, H. Li, J. Chen, Z. Zang, *Chem. Eng. J.* **2020**, *394*, 124903.
[101] B. Ding, S. Y. Huang, Q. Q. Chu, Y. Li, C. X. Li, C. J. Li, G. J. Yang, *J. Mater. Chem. A* **2018**, *6*, 10233.
[102] Z. Wang, M. A. Kamarudin, N. C. Huey, F. Yang, M. Pandey, G. Kapil, T. Ma, S. Hayase, *ChemSusChem* **2018**, *11*, 3941.
[103] W. Zhang, Y. Li, X. Liu, D. Tang, X. Li, X. Yuan, *Chem. Eng. J.* **2020**, *379*, 122298.
[104] E. H. Jung, B. Chen, K. Bertens, M. Vafaie, S. Teale, A. Proppe, Y. Hou, T. Zhu, C. Zheng, E. H. Sargent, *ACS Energy Lett.* **2020**, 2796.
[105] Y. Huang, S. Li, C. Wu, S. Wang, C. Wang, R. Ma, *New J. Chem.* **2020**, *44*, 8902.
[106] L. P. S. Cells, N. Irannejad, N. Y. Nia, S. Adhami, E. Lamanna, B. Rezaei, A. di Carlo, *Energies* **2020**, *13*, https://doi.org/10.3390/en13082059.
[107] J. Dagar, S. Castro-Hermosa, G. Lucarelli, A. Zampetti, F. Cacialli, T. M. Brown, *IEEE J. Photovoltaics* **2019**, *9*, 1309.
[108] J. Dagar, S. Castro-Hermosa, G. Lucarelli, F. Cacialli, T. M. Brown, *Nano Energy* **2018**, *49*, 290.

[109] J. A. Christians, P. Schulz, J. S. Tinkham, T. H. Schloemer, S. P. Harvey, B. J. Tremolet de Villers, A. Sellinger, J. J. Berry, J. M. Luther, *Nat. Energy* **2018**, *3*, 68.
[110] A. H. Ghahremani, B. Martin, A. Gupta, J. Bahadur, K. Ankireddy, T. Druffel, *Mater. Des.* **2020**, *185*, 108237.
[111] J. Xie, K. Huang, X. Yu, Z. Yang, K. Xiao, Y. Qiang, X. Zhu, L. Xu, P. Wang, C. Cui, D. Yang, *ACS Nano* **2017**, *11*, 9176.
[112] E. Altuncu, F. Üstel, S. G. Esen, E. Karayel, *J. Achiev. Mater. Manuf. Eng.* **2016**, *77*, 18.
[113] S. Y. Kim, K. Hong, K. Kim, H. K. Yu, W. K. Kim, J. L. Lee, *J. Appl. Phys.* **2008**, *103*, 2.
[114] K. Terpilowski, D. Rymuszka, *Glas. Phys. Chem.* **2016**, *42*, 535.
[115] C. C. Wu, C. I. Wu, J. C. Sturm, A. Kahn, C. C. Wu, C. I. Wu, J. C. Sturm, A. Kahn, *Phys. Lett* **2012**, *1348*, 9.
[116] M. Yamamoto, T. Matsumae, Y. Kurashima, H. Takagi, T. Suga, T. Itoh, E. Higurashi, *Micromachines* **2019**, *10*, https://doi.org/10.3390/mi10020119.
[117] J. Seol, M. L. Monroe, T. J. Anderson, M. A. Hasnain, C. Park, *Conf. Rec. 2006 IEEE 4th World Conf. Photovolt. Energy Conversion, WCPEC-4*, Vol *1*, IEEE, Piscataway, NJ **2006**, p. 236.
[118] J. Horlyck, A. Nashira, E. Lovell, R. Daiyan, N. Bedford, Y. Wei, R. Amal, J. Scott, *Materials* **2019**, *12*, 2756.
[119] J. S. Kim, M. K. Joo, M. Xing Piao, S. E. Ahn, Y. H. Choi, H. K. Jang, G. T. Kim, *J. Appl. Phys.* **2014**, *115*, https://doi.org/10.1063/1.4868630.
[120] X. Ren, Y. Liu, D. G. Lee, W. Bin Kim, G. S. Han, H. S. Jung, S. (Frank) Liu, *InfoMat* **2020**, *2*, 401.
[121] J. Li, T. Bu, Y. Liu, J. Zhou, J. Shi, Z. Ku, Y. Peng, J. Zhong, Y. B. Cheng, F. Huang, *ChemSusChem* **2018**, *11*, 2898.
[122] V. Rohnacher, F. Ullrich, H. Eggers, F. Schackmar, S. Hell, A. Salazar, C. Huck, G. Hernandez-Sosa, U. W. Paetzold, W. Jaegermann, A. Pucci, *Adv. Mater. Technol.* **2020**, https://doi.org/10.1002/admt.202000282.
[123] Y. Luan, X. Yi, P. Mao, Y. Wei, J. Zhuang, N. Chen, T. Lin, C. Li, J. Wang, *iScience* **2019**, *16*, 433.
[124] H. Yu, H. I. Yeom, J. W. Lee, K. Lee, D. Hwang, J. Yun, J. Ryu, J. Lee, S. Bae, S. K. Kim, J. Jang, *Adv. Mater.* **2018**, *30*, https://doi.org/10.1002/adma.201704825.
[125] X. Ren, D. Yang, Z. Yang, J. Feng, X. Zhu, J. Niu, Y. Liu, W. Zhao, S. F. Liu, *ACS Appl. Mater. Interfaces* **2017**, *9*, 2421.
[126] Y. Yang, J. Wu, P. Guo, X. Liu, Q. Guo, Q. Liu, H. Luo, *J. Mater. Sci. Mater. Electron.* **2018**, *29*, 13138.
[127] M. Shekargoftar, J. Pospisil, M. Kratochvíl, J. Vida, P. Souček, T. Homola, *Energy Technol.* **2021**, *9*, https://doi.org/10.1002/ente.202001076.
[128] E. B. Secor, B. Y. Ahn, T. Z. Gao, J. A. Lewis, M. C. Hersam, *Adv. Mater.* **2015**, *27*, 6683.
[129] S. Das, B. Yang, G. Gu, P. C. Joshi, I. N. Ivanov, C. M. Rouleau, T. Aytug, D. B. Geohegan, K. Xiao, *ACS Photonics* **2015**, *2*, 680.
[130] K. Oh, K. Jung, J. Shin, S. Ko, M.-J. Lee, *J. Mater. Sci. Technol.* **2021**, *92*, 171.
[131] C. Liu, L. Zhang, X. Zhou, J. Gao, W. Chen, X. Wang, B. Xu, *Adv. Funct. Mater.* **2019**, *29*, https://doi.org/10.1002/adfm.201807604.
[132] T. Y. Wen, S. Yang, P. F. Liu, L. J. Tang, H. W. Qiao, X. Chen, X. H. Yang, Y. Hou, H. G. Yang, *Adv. Energy Mater.* **2018**, *8*, https://doi.org/10.1002/aenm.201703143.
[133] H. Zhu, F. Zhang, Y. Xiao, S. Wang, X. Li, *J. Mater. Chem. A* **2018**, *6*, 4971.
[134] C. Fei, B. Li, R. Zhang, H. Fu, J. Tian, G. Cao, *Adv. Energy Mater.* **2017**, *7*, https://doi.org/10.1002/aenm.201602017.
[135] L. Zhu, Y. Xu, P. Zhang, J. Shi, Y. Zhao, H. Zhang, J. Wu, Y. Luo, D. Li, Q. Meng, *J. Mater. Chem. A* **2017**, *5*, 20874.
[136] S. You, H. Wang, S. Bi, J. Zhou, L. Qin, X. Qiu, Z. Zhao, Y. Xu, Y. Zhang, X. Shi, H. Zhou, Z. Tang, *Adv. Mater.* **2018**, *30*, https://doi.org/10.1002/adma.201706924.
[137] Y. Ai, W. Liu, C. Shou, J. Yan, N. Li, Z. Yang, W. Song, B. Yan, J. Sheng, J. Ye, *Sol. Energy* **2019**, *194*, 541.
[138] K. A. Luck, T. A. Shastry, S. Loser, G. Ogien, T. J. Marks, M. C. Hersam, *Phys. Chem. Chem. Phys.* **2013**, *15*, 20966.
[139] R. Cisneros, M. Beley, F. Lapicque, *Phys. Chem. Chem. Phys.* **2016**, *18*, 9645.
[140] C. Goh, S. R. Scully, M. D. McGehee, *J. Appl. Phys.* **2007**, *101*, https://doi.org/10.1063/1.2737977.
[141] G. Yang, C. Wang, H. Lei, X. Zheng, P. Qin, L. Xiong, X. Zhao, Y. Yan, G. Fang, *J. Mater. Chem. A* **2017**, *5*, 1658.
[142] A. N. Cho, N. G. Park, *ChemSusChem* **2017**, *10*, 3687.
[143] Y. Shi, H. Zhang, X. Tong, X. Hou, F. Li, Y. Du, S. Wang, Q. Zhang, P. Liu, X. Zhao, *Sol. RRL* **2021**, *2100128*, https://doi.org/10.1002/solr.202100128.
[144] L. Xiong, Y. Guo, J. Wen, H. Liu, G. Yang, P. Qin, G. Fang, *Adv. Funct. Mater.* **2018**, *28*, https://doi.org/10.1002/adfm.201802757.
[145] Y. Hou, C. O. R. Quiroz, S. Scheiner, W. Chen, T. Stubhan, A. Hirsch, M. Halik, C. J. Brabec, *Adv. Energy Mater.* **2015**, *5*, https://doi.org/10.1002/aenm.201501056.
[146] A. Abrusci, S. D. Stranks, P. Docampo, H. L. Yip, A. K. Y. Jen, H. J. Snaith, *Nano Lett.* **2013**, *13*, 3124.
[147] L. Zuo, Z. Gu, T. Ye, W. Fu, G. Wu, H. Li, H. Chen, *J. Am. Chem. Soc.* **2015**, *137*, 2674.
[148] K. Choi, J. Lee, H. Il Kim, C. W. Park, G. W. Kim, H. Choi, S. Park, S. A. Park, T. Park, *Energy Environ. Sci.* **2018**, *11*, 3238.
[149] X. Zhao, J. Dong, D. Wu, J. Zhou, J. Feng, Y. Yao, C. Y. Xu, X. Yang, X. Tang, Q. Song, *ACS Appl. Energy Mater.* **2021**, *4*, 3794.
[150] J. Yan, Z. Lin, Q. Cai, X. Wen, C. Mu, *ACS Appl. Energy Mater.* **2020**, *3*, 3504.
[151] J. Zhang, H. Yu, *J. Mater. Chem. A* **2021**, *9*, 4138.
[152] F. Ye, D. Zhang, X. Xu, H. Guo, S. Liu, S. Zhang, Y. Wu, W. H. Zhu, *Sol. RRL* **2021**, *5*, https://doi.org/10.1002/solr.202000736.
[153] Z. Tang, T. Bessho, F. Awai, T. Kinoshita, M. M. Maitani, R. Jono, T. N. Murakami, H. Wang, T. Kubo, S. Uchida, H. Segawa, *Sci. Rep.* **2017**, *7*, 12183.
[154] J. K. Nam, S. U. Chai, W. Cha, Y. J. Choi, W. Kim, M. S. Jung, J. Kwon, D. Kim, J. H. Park, *Nano Lett.* **2017**, *17*, 2028.
[155] Y. Yang, L. Wu, X. Hao, Z. Tang, H. Lai, J. Zhang, W. Wang, L. Feng, *RSC Adv.* **2019**, *9*, 28561.
[156] P. Wang, J. Wang, X. Zhang, H. Wang, X. Cui, S. Yuan, H. Lu, L. Tu, Y. Zhan, L. Zheng, *J. Mater. Chem. A* **2018**, *6*, 15853.
[157] W. Liu, Z. Ma, S. Wang, J. Jiang, N. Yuan, J. Ding, *J. Solid State Electrochem.* **2018**, *22*, 3751.
[158] Y. Ogomi, A. Morita, S. Tsukamoto, T. Saitho, Q. Shen, T. Toyoda, K. Yoshino, S. S. Pandey, T. Ma, S. Hayase, *J. Phys. Chem. C* **2014**, *118*, 16651.
[159] M. A. Kozhushner, V. L. Bodneva, I. I. Oleynik, T. V. Belysheva, M. I. Ikim, L. I. Trakhtenberg, *J. Phys. Chem. C* **2017**, *121*, 6940.
[160] J. Jiménez-López, E. Palomares, *Nanoscale* **2019**, *11*, 20024.
[161] S. Gholipour, A. M. Ali, J.-P. Correa-Baena, S.-H. Turren-Cruz, F. Tajabadi, W. Tress, N. Taghavinia, M. Grätzel, A. Abate, F. De Angelis, C. A. Gaggioli, E. Mosconi, A. Hagfeldt, M. Saliba, *Adv. Mater.* **2017**, *1702005*, 1702005.
[162] M. Yu, L. Chen, G. Li, C. Xu, C. Luo, M. Wang, G. Wang, Y. Yao, L. Liao, S. Zhang, Q. Song, *RSC Adv.* **2020**, *10*, 19513.
[163] H. P. Boehm, *Discuss. Faraday Soc.* **1971**, *52*, 264.
[164] P. Sakthivel, S. Foo, M. Thambidurai, P. C. Harikesh, N. Mathews, R. Yuvakkumar, G. Ravi, C. Dang, *J. Power Sources* **2020**, *471*, 228443.

[165] W. Gong, H. Guo, H. Zhang, J. Yang, H. Chen, L. Wang, F. Hao, X. Niu, *J. Mater. Chem. C* **2020**, *8*, 11638.
[166] S. Shao, M. A. Loi, *Adv. Mater. Interfaces* **2020**, *7*, 1901469.
[167] X. Li, W. Zhang, K. Usman, J. Fang, *Adv. Energy Mater.* **2018**, *8*, https://doi.org/10.1002/aenm.201702730.
[168] Y. Sun, J. Zhang, H. Yu, J. Wang, C. Huang, J. Huang, *Chem. Eng. J.* **2021**, *420*, 129579.
[169] K. Mahmood, A. Khalid, F. Nawaz, M. T. Mehran, *J. Colloid Interface Sci.* **2018**, *532*, 387.
[170] O. Zhao, Y. Ding, D. Cheng, J. Zhang, F. Hilt, N. Rolston, G. Jiang, R. H. Dauskardt, *Thin Solid Films* **2021**, *730*, 138708.
[171] M. Zhong, Y. Liang, J. Zhang, Z. Wei, Q. Li, D. Xu, *J. Mater. Chem. A* **2019**, *7*, 6659.
[172] P. Hang, J. Xie, C. Kan, B. Li, Y. Zhang, P. Gao, D. Yang, X. Yu, *Adv. Mater.* **2021**, *33*, https://doi.org/10.1002/adma.202006910.
[173] S. K. Huang, Y. C. Wang, W. C. Ke, Y. T. Kao, N. Z. She, J. X. Li, C. W. Luo, A. Yabushita, D. Y. Wang, Y. J. Chang, K. Tsukagoshi, C. W. Chen, *J. Mater. Chem. A* **2020**, *8*, 23607.
[174] K. Liu, S. Chen, J. Wu, H. Zhang, M. Qin, X. Lu, Y. Tu, Q. Meng, X. Zhan, *Energy Environ. Sci.* **2018**, *11*, 3463.
[175] Y. Chen, J. Shi, X. Li, S. Li, X. Lv, X. Sun, X. Tao, J. Shi, Y. Z. Zheng, *J. Mater. Chem. A* **2020**, *8*, 6349.
[176] D. Rueda-Delgado, I. M. Hossain, M. Jakoby, J. A. Schwenzer, T. Abzieher, I. A. Howard, B. S. Richards, U. Lemmer, U. W. Paetzold, *Org. Electron.* **2020**, *77*, 105526.
[177] C. Tian, K. Lin, J. Lu, W. Feng, P. Song, L. Xie, Z. Wei, *Small Methods* **2020**, *4*, https://doi.org/10.1002/smtd.201900476.
[178] S. Tsarev, S. Y. Luchkin, K. J. Stevenson, P. A. Troshin, *Synth. Met.* **2020**, *268*, 116497.
[179] X. Hu, H. Wang, M. Wang, Z. Zang, *Sol. Energy* **2020**, *206*, 816.
[180] M. Sun, H. Zhang, C. Liang, C. Ji, X. Jing, F. Sun, Q. Song, F. You, Z. He, *Adv. Mater. Interfaces* **2020**, *7*, https://doi.org/10.1002/admi.202000412.
[181] H. Li, Q. Wang, H. Li, J. Zhuang, H. Guo, X. Liu, H. Wang, R. Zheng, X. Gong, *J. Phys. Chem. C* **2020**, *124*, 12948.
[182] Z. W. Gao, Y. Wang, H. Liu, J. Sun, J. Kim, Y. Li, B. Xu, W. C. H. Choy, *Adv. Funct. Mater.* **2021**, *2101438*, https://doi.org/10.1002/adfm.202101438.
[183] L. Ren, L. Liang, Z. Zhang, Z. Zhang, Q. Xiong, N. Zhao, Y. Yu, R. Scopelliti, P. Gao, *RSC Adv.* **2021**, *11*, 3792.
[184] X. Liu, X. Tan, Z. Liu, H. Ye, B. Sun, T. Shi, Z. Tang, G. Liao, *Nano Energy* **2019**, *56*, 184.
[185] Y. Deng, S. Li, X. Li, R. Wang, *Sol. Energy Mater. Sol. Cells* **2020**, *215*, 110594.
[186] Y. Deng, S. Li, X. Li, R. Wang, X. Li, *Electrochim. Acta* **2019**, *326*, https://doi.org/10.1016/j.electacta.2019.134924.
[187] H. Xie, X. Yin, J. Liu, Y. Guo, P. Chen, W. Que, G. Wang, B. Gao, *Appl. Surf. Sci.* **2019**, *464*, 700.
[188] M. Hu, L. Zhang, S. She, J. Wu, X. Zhou, X. Li, D. Wang, J. Miao, G. Mi, H. Chen, Y. Tian, B. Xu, C. Cheng, *Sol. RRL* **2020**, *4*, https://doi.org/10.1002/solr.201900331.
[189] C.-H. Chiang, C.-W. Kan, C.-G. Wu, *ACS Appl. Mater. Interfaces* **2021**, *13*, 23606.
[190] Y. Rao, Z. Li, D. Liu, C. Chen, X. Wang, G. Cui, S. Pang, *ACS Appl. Mater. Interfaces* **2021**, *13*, 20043.
[191] J. Ma, G. Yang, M. Qin, X. Zheng, H. Lei, C. Chen, Z. Chen, Y. Guo, H. Han, X. Zhao, G. Fang, *Adv. Sci.* **2017**, *4*, https://doi.org/10.1002/advs.201700031.
[192] H. Wang, H. Li, S. Cao, M. Wang, J. Chen, Z. Zang, *Sol. RRL* **2020**, *4*, https://doi.org/10.1002/solr.202000226.
[193] L. Yan, Q. Xue, M. Liu, Z. Zhu, J. Tian, Z. Li, Z. Chen, Z. Chen, H. Yan, H. L. Yip, Y. Cao, *Adv. Mater.* **2018**, *30*, https://doi.org/10.1002/adma.201802509.
[194] Y. W. Noh, I. S. Jin, K. S. Kim, S. H. Park, J. W. Jung, *J. Mater. Chem. A* **2020**, https://doi.org/10.1039/d0ta04721j.
[195] Y. Yang, T. Wang, Y. Zhang, X. Zhang, N. Li, P. Wang, Y. Qian, Q. Rong, L. Shui, G. Zhou, L. Nian, *Sol. Energy* **2020**, *196*, 22.
[196] P. Wang, R. Li, B. Chen, F. Hou, J. Zhang, Y. Zhao, X. Zhang, *Adv. Mater.* **2020**, *32*, https://doi.org/10.1002/adma.201905766.
[197] F. Wang, Y. Zhang, M. Yang, J. Du, L. Xue, L. Yang, L. Fan, Y. Sui, J. Yang, X. Zhang, *Nano Energy* **2019**, *63*, https://doi.org/10.1016/j.nanoen.2019.06.021.
[198] J. Sun, Y. Li, N. Tang, Y. Zhou, X. Zhang, X. Lu, X. Gao, J. Gao, L. Shui, S. Wu, J. M. Liu, *ACS Appl. Energy Mater.* **2020**, *3*, 3328.
[199] L. Lin, T. W. Jones, J. T. W. Wang, A. Cook, N. D. Pham, N. W. Duffy, B. Mihaylov, M. Grigore, K. F. Anderson, B. C. Duck, H. Wang, J. Pu, J. Li, B. Chi, G. J. Wilson, *Small* **2020**, *16*, https://doi.org/10.1002/smll.201901466.
[200] D. Zhang, H. Tian, S. Bu, T. Yan, J. Ge, T. Lei, W. Bi, L. Huang, Z. Ge, *J. Alloys Compd.* **2020**, *831*, 154717.
[201] Q. Sun, H. Li, X. Gong, H. Ban, Y. Shen, M. Wang, *Sol. RRL* **2020**, *4*, https://doi.org/10.1002/solr.201900229.
[202] H. B. Lee, N. Kumar, M. M. Ovhal, Y. J. Kim, Y. M. Song, J. W. Kang, *Adv. Funct. Mater.* **2020**, *30*, https://doi.org/10.1002/adfm.202001559.
[203] V. Yarangsi, K. Hongsith, S. Sucharitakul, A. Ngamjarurojana, A. Tuantranont, P. Kumnorkaew, Y. Zhao, S. Phadungdhitidhada, S. Choopun, *J. Phys. D. Appl. Phys.* **2020**, *53*, https://doi.org/10.1088/1361-6463/abb1e8.
[204] X. Guo, J. Du, Z. Lin, J. Su, L. Feng, J. Zhang, Y. Hao, J. Chang, *Chem. Eng. J.* **2021**, *407*, https://doi.org/10.1016/j.cej.2020.127997.
[205] J. Ye, Y. Li, A. A. Medjahed, S. Pouget, D. Aldakov, Y. Liu, P. Reiss, *Small* **2021**, *17*, https://doi.org/10.1002/smll.202005671.
[206] P. Song, L. Shen, L. Zheng, K. Liu, W. Tian, J. Chen, Y. Luo, C. Tian, L. Xie, Z. Wei, *Nano Sel.* **2021**, https://doi.org/10.1002/nano.202000306.
[207] X. Shi, R. Chen, T. Jiang, S. Ma, X. Liu, Y. Ding, M. Cai, J. Wu, S. Dai, *Sol. RRL* **2020**, *4*, https://doi.org/10.1002/solr.201900198.
[208] X. Chen, Z. Shi, G. Pan, J. Zhu, J. Hu, Y. Wu, Y. Tian, X. Li, W. Xu, *Mater. Today Energy* **2021**, *21*, https://doi.org/10.1016/j.mtener.2021.100724.
[209] J. Zhuang, P. Mao, Y. Luan, N. Chen, X. Cao, G. Niu, F. Jia, F. Wang, S. Cao, J. Wang, *Adv. Funct. Mater.* **2021**, *31*, https://doi.org/10.1002/adfm.202010385.
[210] N. Li, X. Niu, F. Pei, H. Liu, Y. Cao, Y. Liu, H. Xie, Y. Gao, Q. Chen, F. Mo, H. Zhou, *Sol. RRL* **2020**, *4*, https://doi.org/10.1002/solr.201900217.
[211] J. Chen, J. Zhang, C. Huang, Z. Bi, X. Xu, H. Yu, *Chem. Eng. J.* **2021**, *410*, 128436.
[212] A. S. R. Bati, M. Batmunkh, J. G. Shapter, *Adv. Energy Mater.* **2020**, *10*, https://doi.org/10.1002/aenm.201902253.
[213] L. Yang, Y. Dall'Agnese, K. Hantanasirisakul, C. E. Shuck, K. Maleski, M. Alhabeb, G. Chen, Y. Gao, Y. Sanehira, A. K. Jena, L. Shen, C. Dall'Agnese, X. F. Wang, Y. Gogotsi, T. Miyasaka, *J. Mater. Chem. A* **2019**, *7*, 5635.
[214] Y. Wang, P. Xiang, A. Ren, H. Lai, Z. Zhang, Z. Xuan, Z. Wan, J. Zhang, X. Hao, L. Wu, M. Sugiyama, U. Schwingenschlögl, C. Liu, Z. Tang, J. Wu, Z. Wang, D. Zhao, *ACS Appl. Mater. Interfaces* **2020**, *12*, 53973.
[215] N. Ren, B. Chen, R. Li, P. Wang, S. Mazumdar, B. Shi, C. Zhu, Y. Zhao, X. Zhang, *Sol. RRL* **2021**, *5*, https://doi.org/10.1002/solr.202000795.
[216] L. He, Z. Lv, H. Jiang, X. Ma, F. Wang, L. Fan, M. Wei, J. Yang, L. Yang, H. Liu, *J. Power Sources* **2020**, *453*, https://doi.org/10.1016/j.jpowsour.2020.227876.

[217] D. Aidarkhanov, Z. Ren, C. K. Lim, Z. Yelzhanova, G. Nigmetova, G. Taltanova, B. Baptayev, F. Liu, S. H. Cheung, M. Balanay, A. Baumuratov, A. B. Djurišić, S. K. So, C. Surya, P. N. Prasad, A. Ng, *Sol. Energy Mater. Sol. Cells* **2020**, *215*, https://doi.org/10.1016/j.solmat.2020.110648.
[218] Y. Qiang, Y. Xie, Y. Qi, P. Wei, H. Shi, C. Geng, H. Liu, *Sol. Energy* **2020**, *201*, 523.
[219] G. Yang, H. Lei, H. Tao, X. Zheng, J. Ma, Q. Liu, W. Ke, Z. Chen, L. Xiong, P. Qin, Z. Chen, M. Qin, X. Lu, Y. Yan, G. Fang, *Small* **2017**, *13*, https://doi.org/10.1002/smll.201601769.
[220] Q. Liu, X. Zhang, C. Li, H. Lu, Z. Weng, Y. Pan, W. Chen, X. C. Hang, Z. Sun, Y. Zhan, *Appl. Phys. Lett.* **2019**, *115*, https://doi.org/10.1063/1.5118679.
[221] J. Liu, N. Li, Q. Dong, J. Li, C. Qin, L. Wang, *Sci. China Mater.* **2019**, *62*, 173.
[222] H. Chen, D. Liu, Y. Wang, C. Wang, T. Zhang, P. Zhang, H. Sarvari, Z. Chen, S. Li, *Nanoscale Res. Lett.* **2017**, *12*, 238.
[223] Z. Ma, W. Zhou, Z. Xiao, H. Zhang, Z. Li, J. Zhuang, C. Peng, Y. Huang, *Org. Electron.* **2019**, *71*, 98.
[224] J. J. Cao, K. L. Wang, C. Dong, X. M. Li, W. F. Yang, Z. K. Wang, *Org. Electron.* **2021**, *88*, 105972.
[225] R. Wang, J. Wu, S. Wei, J. Zhu, M. Guo, Q. Zheng, M. Wei, S. Cheng, *J. Power Sources* **2022**, *544*, 231870.
[226] D. Liu, W. Zhang, Z. Ren, X. Li, *RSC Adv.* **2022**, *12*, 14631.
[227] X. Gong, Q. Sun, S. Liu, P. Liao, Y. Shen, C. Gra, S. M. Zakeeruddin, M. Gra, M. Wang, **2018**, https://doi.org/10.1021/acs.nanolett.8b01440.
[228] J. B. Wu, C. Zhen, G. Liu, *Rare Met.* **2022**, *41*, 361.
[229] Y. Bai, Y. Fang, Y. Deng, Q. Wang, J. Zhao, X. Zheng, Y. Zhang, J. Huang, *ChemSusChem* **2016**, *9*, 2686.
[230] J. Bahadur, A. H. Ghahremani, B. Martin, T. Druffel, M. K. Sunkara, K. Pal, *Org. Electron.* **2019**, *67*, 159.
[231] Y. W. Noh, J. H. Lee, I. S. Jin, S. H. Park, J. W. Jung, *Nano Energy* **2019**, *65*, 104014.
[232] H. Guo, H. Chen, H. Zhang, X. Huang, J. Yang, B. Wang, Y. Li, L. Wang, X. Niu, Z. Wang, *Nano Energy* **2019**, *59*, https://doi.org/10.1016/j.nanoen.2019.01.059.
[233] W. Ahmad, D. Liu, J. Wu, W. Ahmad, Y. Wang, P. Zhang, T. Zhang, H. Zheng, L. Chen, Z. D. Chen, S. Li, *IEEE J. Photovoltaics* **2019**, *9*, 1273.
[234] J. Jia, J. Dong, J. Wu, H. Wei, B. Cao, *J. Alloys Compd.* **2020**, *844*, 156032.
[235] Y. Chen, X. Zuo, Y. He, F. Qian, S. Zuo, Y. Zhang, L. Liang, Z. Chen, K. Zhao, Z. Liu, J. Gou, S. Liu, *Adv. Sci.* **2021**, *8*, https://doi.org/10.1002/advs.202001466.
[236] J. Liang, Z. Chen, G. Yang, H. Wang, F. Ye, C. Tao, G. Fang, *ACS Appl. Mater. Interfaces* **2019**, *11*, 23152.
[237] X. Ren, D. Yang, Z. Yang, J. Feng, X. Zhu, J. Niu, Y. Liu, W. Zhao, S. F. Liu, **2017**, https://doi.org/10.1021/acsami.6b13362.
[238] J. Tian, J. Zhang, X. Li, B. Cheng, J. Yu, W. Ho, *Sol. RRL* **2020**, *4*, https://doi.org/10.1002/solr.202000090.
[239] S. Zhang, H. Gu, S. C. Chen, Q. Zheng, *J. Mater. Chem. C* **2021**, *9*, 4240.
[240] J. Song, E. Zheng, X. F. Wang, W. Tian, T. Miyasaka, *Sol. Energy Mater. Sol. Cells* **2016**, *144*, 623.
[241] J. Chen, H. Dong, L. Zhang, J. Li, F. Jia, B. Jiao, J. Xu, X. Hou, J. Liu, Z. Wu, *J. Mater. Chem. A* **2020**, *8*, 2644.
[242] S. Wang, Y. Zhu, B. Liu, C. Wang, R. Ma, *J. Mater. Chem. A* **2019**, *7*, 5353.
[243] H. Tang, Q. Cao, Z. He, S. Wang, J. Han, T. Li, B. Gao, J. Yang, D. Deng, X. Li, *Sol. RRL* **2020**, *4*, https://doi.org/10.1002/solr.201900415.
[244] J. Chen, Z. Bi, X. Xu, H. Yu, *Electrochim. Acta* **2020**, *330*, 135197.
[245] P. Zhu, S. Gu, X. Luo, Y. Gao, S. Li, J. Zhu, H. Tan, *Adv. Energy Mater.* **2020**, *10*, https://doi.org/10.1002/aenm.201903083.
[246] W. Hui, Y. Yang, Q. Xu, H. Gu, S. Feng, Z. Su, M. Zhang, J. Wang, X. Li, J. Fang, F. Xia, Y. Xia, Y. Chen, X. Gao, W. Huang, *Adv. Mater.* **2020**, *32*, https://doi.org/10.1002/adma.201906374.
[247] M. Kouhnavard, D. M. Niedzwiedzki, P. Biswas, *Int. J. Energy Res.* **2020**, https://doi.org/10.1002/er.5754.
[248] Y. Zhou, S. Yang, X. Yin, J. Han, M. Tai, X. Zhao, H. Chen, Y. Gu, N. Wang, H. Lin, *J. Mater. Chem. A* **2019**, *7*, 1878.
[249] S. Pang, C. Zhang, H. Zhang, H. Dong, D. Chen, W. Zhu, H. Xi, J. Chang, Z. Lin, J. Zhang, Y. Hao, *Appl. Surf. Sci.* **2020**, *507*, https://doi.org/10.1016/j.apsusc.2019.145099.
[250] S. Zhang, H. Si, W. Fan, M. Shi, M. Li, C. Xu, Z. Zhang, Q. Liao, A. Sattar, Z. Kang, Y. Zhang, *Angew. Chem. Int. Ed.* **2020**, *59*, 11573.
[251] W. Cao, J. Zhang, K. Lin, L. Qiu, J. Li, Y. Dong, J. Wang, D. Xia, R. Fan, Y. Yang, *Sol. RRL* **2021**, https://doi.org/10.1002/solr.202100058.
[252] C. Huang, P. Lin, N. Fu, K. Sun, M. Ye, C. Liu, X. Zhou, L. Shu, X. Hao, B. Xu, X. Zeng, Y. Wang, S. Ke, *J. Mater. Chem. A* **2018**, *6*, 22086.
[253] H. Bi, X. Zuo, B. Liu, D. He, L. Bai, W. Wang, X. Li, Z. Xiao, K. Sun, Q. Song, Z. Zang, J. Chen, *J. Mater. Chem. A* **2021**, *9*, 3940.
[254] W. Zhang, X. Zheng, Y. Li, L. He, X. Li, *Electrochim. Acta* **2021**, *371*, 137812.
[255] X. Huang, J. Du, X. Guo, Z. Lin, J. Ma, J. Su, L. Feng, C. Zhang, J. Zhang, J. Chang, Y. Hao, *Sol. RRL* **2020**, *4*, 1.
[256] S. You, H. Zeng, Z. Ku, X. Wang, Z. Wang, Y. Rong, Y. Zhao, X. Zheng, L. Luo, L. Li, S. Zhang, M. Li, X. Gao, X. Li, *Adv. Mater.* **2020**, *32*, 1.
[257] M. Zhang, F. Wu, D. Chi, K. Shi, S. Huang, *Mater. Adv.* **2020**, *1*, 617.
[258] Z. Lv, L. He, H. Jiang, X. Ma, F. Wang, L. Fan, M. Wei, J. Yang, L. Yang, N. Yang, *ACS Appl. Mater. Interfaces* **2021**, *13*, 16326.
[259] R. Xue, X. Zhou, S. Peng, P. Xu, S. Wang, C. Xu, W. Zeng, Y. Xiong, D. Liang, *ACS Sustain. Chem. Eng.* **2020**, *8*, 10714.
[260] Y. Yang, H. Lu, S. Feng, L. Yang, H. Dong, J. Wang, C. Tian, L. Li, H. Lu, J. Jeong, S. M. Zakeeruddin, Y. Liu, M. Grätzel, A. Hagfeldt, *Energy Environ. Sci.* **2021**, https://doi.org/10.1039/d1ee00056j.
[261] R. Tao, Y. Zhang, Z. Jin, Z. Sun, L. Xu, *Electrochim. Acta* **2018**, *284*, 10.
[262] K. Jung, W. S. Chae, Y. C. Park, N. G. Park, M. J. Lee, *Chem. Eng. J.* **2021**, *409*, 128215.
[263] K. Deng, Q. Chen, L. Li, *Adv. Funct. Mater.* **2020**, *2004209*, https://doi.org/10.1002/adfm.202004209.
[264] G. Mathiazhagan, A. Seeber, T. Gengenbach, S. Mastroianni, D. Vak, A. S. R. Chesman, M. Gao, D. Angmo, A. Hinsch, *Sol. RRL* **2020**, https://doi.org/10.1002/solr.202000262.
[265] J. Wei, F. Guo, X. Wang, K. Xu, M. Lei, Y. Liang, Y. Zhao, D. Xu, *Adv. Mater.* **2018**, *30*, https://doi.org/10.1002/adma.201805153.
[266] Q. Chen, C. Peng, L. Du, T. Hou, W. Yu, D. Chen, H. Shu, D. Huang, X. Zhou, J. Zhang, W. Zhang, H. Li, J. Xie, Y. Huang, *J. Energy Chem.* **2022**, *66*, 250.
[267] Q. Wang, C. Peng, L. Du, H. Li, W. Zhang, J. Xie, H. Qi, Y. Li, L. Tian, Y. Huang, *Adv. Mater. Interfaces* **2020**, *1901866*, https://doi.org/10.1002/admi.201901866.
[268] S. N. Vijayaraghavan, J. Wall, L. Li, G. Xing, Q. Zhang, F. Yan, *Mater. Today Phys.* **2020**, *13*, https://doi.org/10.1016/j.mtphys.2020.100204.
[269] B. Gao, Q. Cao, X. Pu, J. Yang, J. Han, S. Wang, T. Li, Z. He, X. Li, *Appl. Surf. Sci.* **2021**, *546*, 148711.
[270] J. Song, G. Li, D. Wang, W. Sun, J. Wu, Z. Lan, *Sol. RRL* **2020**, *4*, https://doi.org/10.1002/solr.201900558.
[271] P. H. Lee, T. T. Wu, K. Y. Tian, C. F. Li, C. H. Hou, J. J. Shyue, C. F. Lu, Y. C. Huang, W. F. Su, *ACS Appl. Mater. Interfaces* **2020**, *12*, 45936.

[272] C. Liu, H. Su, K. Xie, H. Wang, P. Zhai, N. Chang, S. Zhang, Q. Ban, M. Guo, J. Zhang, L. Liu, *Sol. RRL* **2021**, *2100067*, https://doi.org/10.1002/solr.202100067.
[273] Z. Shi, X. Zhang, J. Guo, X. Li, Z. Weng, F. Liu, L. Wu, I. Ahmed, A. Akram, S. Javed, G. Xing, F. Li, Y. Zhan, L. Zheng, *Sol. RRL* **2020**, *2000406*, https://doi.org/10.1002/solr.202000406.
[274] E. J. Yeom, S. S. Shin, W. S. Yang, S. J. Lee, W. Yin, D. Kim, J. H. Noh, T. K. Ahn, S. Il Seok, *J. Mater. Chem. A* **2017**, *5*, 79.
[275] F. Sadegh, S. Akin, M. Moghadam, V. Mirkhani, M. A. Ruiz–Preciado, Z. Wang, M. M. Tavakoli, M. Graetzel, A. Hagfeldt, W. Tress, *Nano Energy* **2020**, *75*, 105038.
[276] X. Liu, C. C. Chueh, Z. Zhu, S. B. Jo, Y. Sun, A. K. Y. Jen, *J. Mater. Chem. A* **2016**, *4*, 15294.
[277] M. Zhang, X. Cui, Y. Wang, B. Wang, M. Ye, W. Wang, C. Ma, Z. Lin, *Nano Energy* **2020**, *71*, 104620.
[278] S. S. Shin, W. S. Yang, E. J. Yeom, S. J. Lee, N. J. Jeon, Y. C. Joo, I. J. Park, J. H. Noh, S. Il Seok, *J. Phys. Chem. Lett.* **2016**, *7*, 1845.
[279] Y. W. Noh, I. S. Jin, S. H. Park, J. W. Jung, *J. Mater. Sci. Technol.* **2020**, *42*, 38.
[280] S. Baek, J. W. Han, D. Vidyasagar, H. Cho, H. H. Ha, D. H. Kim, Y. W. Heo, S. Lee, *Materials* **2020**, *13*, 32.
[281] D. Vidyasagar, J. W. Han, S. Baek, Y. Yun, J. Yun, H. Jo, Y. Yun, Y. W. Heo, S. Lee, *Mater. Lett.* **2020**, *273*, 127960.
[282] K. Wang, S. Olthof, W. S. Subhani, X. Jiang, Y. Cao, L. Duan, H. Wang, M. Du, S. (Frank) Liu, *Nano Energy* **2020**, *68*, 104289.
[283] D. W. Kim, S. S. Shin, S. Lee, I. S. Cho, D. H. Kim, C. W. Lee, H. S. Jung, K. S. Hong, *ChemSusChem* **2013**, *6*, 449.
[284] S. S. Mali, C. S. Shim, H. Kim, C. K. Hong, *J. Mater. Chem. A* **2016**, *4*, 12158.
[285] C. Gao, S. Yuan, B. Cao, J. Yu, *Chem. Eng. J.* **2017**, *325*, 378.
[286] C. Zhang, X. Deng, J. Zheng, X. Zhou, J. Shi, X. Chen, Z. Sun, S. Huang, *Electrochim. Acta* **2018**, *283*, 1134.
[287] X. Fan, Y. Rui, X. Han, J. Yang, Y. Wang, Q. Zhang, *J. Power Sources* **2020**, *448*, 227405.
[288] C. Altinkaya, E. Aydin, E. Ugur, F. H. Isikgor, A. S. Subbiah, M. De Bastiani, J. Liu, A. Babayigit, T. G. Allen, F. Laquai, A. Yildiz, S. De Wolf, *Adv. Mater.* **2021**, *33*, 1.
[289] S. Y. Park, K. Zhu, *Adv. Mater.* **2022**, *34*, 1.
[290] M. Shekargoftar, J. Pospisil, M. Kratochvíl, J. Vida, P. Souček, T. Homola, *Energy Technol.* **2021**, *9*, https://doi.org/10.1002/ente.202001076.
[291] X. Guo, J. Du, Z. Lin, J. Su, L. Feng, J. Zhang, Y. Hao, J. Chang, *Chem. Eng. J.* **2021**, *407*, 127997.
[292] Y. Huang, S. Li, C. Wu, S. Wang, C. Wang, R. Ma, *Chem. Phys. Lett.* **2020**, *745*, 137220.
[293] J. Song, W. Zhang, D. Wang, K. Deng, J. Wu, Z. Lan, *Sol. Energy* **2019**, *185*, 508.
[294] A. Phys, Z. Sun, **2019**, *143903*, https://doi.org/10.1063/1.5118679.
[295] Z. Qian, L. Chen, J. Wang, L. Wang, Y. Xia, X. Ran, P. Li, Q. Zhong, L. Song, P. Müller-Buschbaum, Y. Chen, H. Zhang, *Adv. Mater. Interfaces* **2021**, *8*, 1.

Maryam Haghighi is a researcher at the Nano Particles and Coating Laboratory (NCL), Sharif University of Technology. Previously, she worked on supercapacitors and 2D materials during her Postdoctoral Fellow at the Amirkabir University of Technology. She received her Ph.D. at the Nanotechnology Department at Sharif University of Technology in 2018, working on 2D materials, perovskite, and thin film (CIGS, CZTS) solar cells. Her research interests are currently focused on photovoltaic solar cells, large-scale a low-temperature deposition methods, supercapacitors, catalysts, and 2D materials.

Nahid Ghazyani is the postdoc researcher at Nano particles and coating laboratory (NCL), physics department of Sharif University of Technology. She received her Ph.D. degree from Kharazmi University in 2020. During her M.Sc. and Ph.D. programs, she focused on the fabrication and characterization of nanomaterials and nanostructures for solar cells and photonic devices. She has published high value works including papers and conference proceedings. Her research interests include perovskite solar cells, sensor, upconversion materials, and nonlinear optics.

Huiming Luo is currently a Ph.D. student in functional materials and energy device research group (FMED), Institute for Materials Discovery in University College London. She received her M.Sc. from South China University of Technology in 2022 and B.Sc. degree from Nanjing Forestry University in 2019 in environmental engineering. Now, her research focus is on the development of eco-friendly optoelectronic devices such as solar cells and light-emitting diodes based on tin-halide perovskites and double perovskites.

Raheleh Mohammadpour received her B.Sc., M.Sc., and Ph.D. degrees from Sharif University of Technology with two visiting scholars from Uppsala University and National Chiao Tung University. She has published more than 100 peer-reviewed works including papers and conference proceedings. The area of her expertise includes self-powered sensor, triboelectric nanogenerator, and solar cells.

Nima Taghavinia is a full professor at Sharif University of Technology, Tehran, Iran. He received his B.Sc. and M.Sc. degrees in physics at Sharif University of Technology, Iran, in 1994 and 1996, respectively. He received a Ph.D. in Materials Science from Tohoku University, Japan, in 2002. Since then, he has been a faculty member of the Physics Department and a member of the Institute for Nanoscience and Nanotechnology at Sharif University of Technology. His research interests include optoelectronics, photovoltaic solar cells, and light-emitting diodes.

Mojtaba Abdi-Jalebi is an Assistant Professor in energy and functional materials in the Institute for Materials Discovery, University College London. He completed his Ph.D. in Physics at Cavendish Laboratory, University of Cambridge. From 2018 to 2020, he was a Junior Research Fellow at Wolfson College in Cambridge. His research focuses on the development of emerging semiconductors for low-cost optoelectronic and electrochemical devices for low-cost electronics applications and energy systems enabling carbon capture and production of solar fuels. His research aims to develop and incorporate new inexpensive materials in energy devices to alter the energy landscape by reducing the cost of energy production, consumption, and storage.